

**Transformation to zero offset
for mode-converted waves**

by
Mohammed N. Alfaraj

ProQuest Number: 10796548

All rights reserved

INFORMATION TO ALL USERS

The quality of this reproduction is dependent upon the quality of the copy submitted.

In the unlikely event that the author did not send a complete manuscript and there are missing pages, these will be noted. Also, if material had to be removed, a note will indicate the deletion.



ProQuest 10796548

Published by ProQuest LLC (2019). Copyright of the Dissertation is held by the Author.

All rights reserved.

This work is protected against unauthorized copying under Title 17, United States Code
Microform Edition © ProQuest LLC.

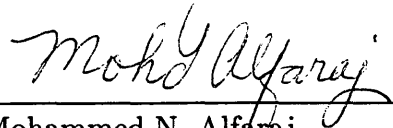
ProQuest LLC.
789 East Eisenhower Parkway
P.O. Box 1346
Ann Arbor, MI 48106 – 1346


T-4344

A thesis submitted to the Faculty and the Board of Trustees of the Colorado School of Mines in partial fulfillment of the requirements for the degree of Doctor of Philosophy (Geophysics).

Golden, Colorado


Date 4/27/93

Signed: 
Mohammed N. Alfaraj

Approved: 
Dr. Kenneth L. Larner
Professor of Geophysics
Thesis Advisor

Golden, Colorado

Date April 27, 1973


Dr. Phillip R. Romig
Professor and Head
Department of Geophysics

ABSTRACT

I present and analyze two approaches for doing transformation to zero offset (TZO) for mode-converted waves. One approach, which, in principle, is exact for constant-velocity media, is implemented in a nonphysical domain, referred to as the $k-t_1$ domain. The other approach, which is approximate, is implemented in the frequency-wavenumber ($f-k$) domain.

The exact $k-t_1$ TZO approach is an extension to mode conversion of the Gardner's TZO method, which was developed for ordinary p-waves. In this approach, the physical half-offset and the recorded time are mapped into a nonphysical half-offset k and a nonphysical time t_1 . The mapping requires knowing only the velocity ratio, not the individual velocities themselves. Analyses show that this approach has three intrinsic problems, namely, amplitude and phase, amplitude-verses-offset, and large-offset problems. Due to these unresolved problems, the $k-t_1$ TZO method is not recommended for processing seismic data, be it mode-converted or conventional (ordinary p-waves). However, this approach may be used to find stacking velocity. Velocity analysis in the $k-t_1$ domain yields velocities that are dip-independent. This is true even for mode-converted waves, in which case the reciprocal of such a stacking velocity is seen as simply the arithmetic mean of the downgoing and upgoing slownesses.

The mode-converted $f-k$ TZO method, on the other hand, is a practical way to process mode-converted data. It requires only slight modification to the existing Hale's TZO method for ordinary p-waves. To modify Hale's TZO method to mode conversion, one again needs to know only the velocity ratio. The mode-converted

TZO operator differs from the elliptical p-wave operator in two aspects. First, the operator is a pseudo-ellipse; its deviation from being an ellipse is controlled solely by the velocity ratio which squeezes one side of the operator and stretches the other, depending on the mode of conversion. Second, the operator is laterally shifted, and in a time-varying manner, so that it closely resembles the behavior of the theoretical operator for mode-converted waves. In addition, in the limit when the velocity ratio is unity, the operator reduces to the conventional, p-wave operator. As with Hale's TZO method, the mode-converted $f-k$ TZO method is also readily extendible to approximately handle velocity variations with depth; this is achieved by simply extending Hale and Artley's squeezing trick to mode-converted waves.

Application of this mode-converted $f-k$ TZO method to synthetic data reveals that the method is capable, to a great extent, of transforming mode-converted data to zero offset. Although not too sensitive to the choice of velocity ratio, the TZO process must account for mode conversion when dealing with mode-converted data. Not only can the mode-converted TZO method correct reflections from dipping reflectors, but also from horizontal ones, in which case reflections are simply shifted laterally to their appropriate, zero-offset reflection points. As for dipping reflectors, reflections are properly TZO-corrected regardless of the sign of dip.

Finally, I have tested the method on two field data sets. Consisting dominantly of p-sv reflections, both data sets were acquired in the same area, but shot in opposite directions. Because the signal-to-noise ratio was poor in both data sets, the results obtained after applying mode-converted TZO were not as dramatic as those seen in the synthetic data. Nevertheless, velocity analysis shows that the stacking velocity, obtained after mode-converted TZO has been applied, is dip-independent—a result both conventional processing (no TZO) and conventional TZO (ignoring mode con-

version) have failed to achieve. Furthermore, I show that the method may be used to qualitatively infer information about the velocity ratio from field, mode-converted, seismic data. I also derive an expression for quantitatively estimating the velocity ratio from the two mode-converted data sets; the expression makes use of the relative shift between the stacks from each set, among other things. Both the qualitative and quantitative approaches reveal that velocity ratio in the range 0.4–0.5 is a good estimate for the data here.

TABLE OF CONTENTS

ABSTRACT	iii
LIST OF FIGURES	viii
Chapter 1 INTRODUCTION	1
Chapter 2 THE KINEMATICS OF CONVERTED WAVES	9
2.1 Introduction	9
2.2 Implicit-dip relation	9
2.3 Explicit-dip relation	16
Chapter 3 TZO BY FOURIER TRANSFORM	20
3.1 Introduction	20
3.2 Hale f - k TZO	20
3.3 NMO-corrected time and NMO velocity for converted waves	22
3.4 TZO for converted waves by Fourier transform	26
3.5 The impulse response	28
3.6 Improving the TZO operator	30
3.6.1 Time-variant phase shift	31
3.6.2 Squeezing and stretching the TZO operator	34
3.7 Full-offset TZO	38
Chapter 4 APPLICATION TO SYNTHETIC DATA	43
4.1 Introduction	43
4.2 Constant velocity	43
4.3 Depth-variable velocity	51
4.3.1 TZO operator for depth-variable velocity	52
4.3.2 Depth-variable velocity: synthetic examples	54
4.4 Sensitivity to velocity ratio	61
4.4.1 Error in Poisson's ratio	66
Chapter 5 APPLICATION TO FIELD DATA	69
5.1 Introduction	69

5.2	Field geometry and preprocessing	70
5.3	Conventional processing	71
5.4	Estimation of velocity ratio	73
5.4.1	Qualitative analysis	74
5.4.2	Quantitative analysis	77
5.5	Application of TZO	79
5.6	Velocity analysis	84
Chapter 6	MODE-CONVERTED TZO IN THE $k-t_1$ DOMAIN .	91
6.1	Introduction	91
6.2	The $k-t_1$ TZO method	92
6.3	Problems with the $k-t_1$ TZO method	95
6.3.1	Amplitude and phase distortion	95
6.3.2	The AVO problem	100
6.3.3	The large-offset problem	100
6.4	Alternative solution	104
6.5	Velocity estimation	105
6.6	Summary	111
Chapter 7	CONCLUSION	115
	REFERENCES	118
Appendix A	OFFSET AND TRAVELTIME FOR CONVERTED WAVES	120
Appendix B	SERIES EXPANSION	123
Appendix C	IMPULSE RESPONSE VIA STATIONARY PHASE .	127
Appendix D	QUARTIC EQUATION FOR b	133
Appendix E	FRESNEL-ZONE WIDTH	137
Appendix F	RANGE OF b	141
Appendix G	MAXIMUM t_1 ALONG A SMILE	144

LIST OF FIGURES

1.1	Impulse responses of the TZO process. Conventional TZO yields a response (a) that is an ellipse with apex directly underneath the midpoint, whereas the response of mode-converted TZO (b) is an asymmetric curve whose apex is laterally shifted, in a time-varying manner, relative to the midpoint. Offset is 2000 m. The medium velocity in (a) is 2000 m/s; the downgoing and upgoing velocities in (b) are 2000 and 1000 m/s, respectively.	4
1.2	CRP gather obtained by applying conventional TZO (ignoring mode conversion) to mode-converted data. For these synthetic data, the downgoing and upgoing velocities are 2000 and 1000 m/s, respectively. The gather shows reflections from five reflectors with dips starting at 0 degrees (shallowest reflector) with an increment of 20 degrees; the dip of the deepest reflector is 80 degrees.	7
1.3	CRP gather obtained by applying mode-converted TZO to the same mode-converted data shown in Figure 1.2. Reflections are now correctly aligned, including those from the steepest (deepest) reflector, which dips at 80 degrees.	8
2.1	Depth section depicting a mode-converted, reflection raypath in a homogeneous medium with a dipping reflector.	10
2.2	The locus of z as a function of x looks somewhat like an ellipse, for constant γ , h , v , and t . Here $\gamma=0.5$, $h=400$ m, $v=2000$ m/s, and $t=1$ s. The midpoint is located at $x=0$	12
2.3	A circle with radius R and center at $(b, 0)$ is tangent to the pseudo-ellipse at reflection point (x, z) . The distance b from the midpoint is the same as that in Figure 2.1.	13
2.4	The curve of Figure 2.2 is constructed from circles whose radii are given by equation (2.7).	14
2.5	Shape of the impulse response $t_0(b)$ of the TZO operation for an impulse at time $t=1$ s. The parameters here are the same as those in Figure 2.2.	15

2.6	Depth section depicting a mode-converted, reflection raypath in a homogeneous medium with a dipping reflector.	17
3.1	CMP gather showing reflections from five horizontal reflectors after NMO correction. The NMO velocity in (a), which did not quite align reflections, is calculated directly from equation (3.9) for $v = 2000$ m/s and $\gamma = 0.5$. The NMO velocity in (b), which is 5% higher than that in (a), yields better alignments.	24
3.2	Theoretical (solid) and approximate (dotted) TZO impulse responses for four input impulses (1.75, 2.4, 3.2, and 4.0 s) at midpoint 0. The approximate operator has a constant (time-invariant) lateral shift, as opposed to the time-variant shift for the theoretical TZO operator. The offset is 2000 m. The downgoing and upgoing velocities are 2000 and 1000 m/s, respectively.	30
3.3	Behavior of the conversion point in a homogeneous medium, as dictated by equation (3.21). Here, for different velocity ratios, normalized depth (D/h) of the conversion point is plotted against the normalized, lateral position (b/h) for a horizontal reflector. The numbers shown on the plots are values of γ . Note that plots for γ and $1/\gamma$ are symmetric about the vertical line $b/h = 0$	32
3.4	Ten impulses in a constant-offset section (a) used to test the response of the TZO operator for mode-converted waves (b). The offset here, 5000 m, is chosen large to emphasize the time-variant lateral shifts seen in the impulse responses in (b). The midpoint spacing is 100 m. . . .	33
3.5	Shapes of approximate TZO response (dashed) to four impulses, along with those of the correct responses (solid lines). Proper, time-variant lateral shifts have been applied in (a). The result in (a) after squeezing/stretching is shown in (b); the squeeze and stretch factors are, respectively, 0.05 and 5.0. A p-sv mode conversion ($\gamma = 0.5$) is assumed here. Offset is 2000 m. Input impulses are the same as those for Figure 3.2.	35
3.6	Response of a TZO algorithm to six impulses, along with the correct responses (solid lines). (a) No squeezing/stretching, (b) Stretch and squeeze factors of 5.0 and 0.05, respectively, have been applied. The responses in (b) are closer to the correct shapes. A p-sv mode conversion ($\gamma = 0.5$) is assumed here. Offset is 2000 m. Input impulses were originally at midpoint 0.	36

3.7	Stretch factor $S1$ (a) and squeeze factor $S2$ (b) as a function of the velocity ratio γ for p–sv mode conversion. $S1$ here stretches positive zero-offset slopes, whereas $S2$ squeezes negative ones. For sv–p mode conversion, factors $S1$ and $S2$ are given by equation (3.23). Asterisks in the plots indicate experimental data.	38
3.8	Impulse-response shapes of full-offset, approximate TZO operator (dashed) to same input data as in Figure 3.5 before (a) and after (b) applying squeeze/stretch (0.04/3.0) compensation. Solid lines indicate theoretical impulse responses. Downgoing and upgoing velocities of 2000 and 1000 m/s, respectively, are assumed. Offset is 2000 m. . . .	39
3.9	CRP gathers obtained by applying scaled-offset TZO (a) and full-offset TZO (b). Reflections here are from five reflectors with dips ranging from 0 (shallowest) to 80 degrees, in increments of 20 degrees. A downgoing velocity of 2000 m/s, and a velocity ratio 0.5 are assumed.	40
3.10	CRP gathers obtained by applying scaled-offset TZO (a) and full-offset TZO (b). Reflections here are from the same five reflectors in Figure 3.9 but with dips reversed in sign.	42
4.1	Zero-offset data for the two test models used to generate synthetic p–sv data. Each figure shows zero-offset reflections from five reflectors in a homogeneous medium. The downgoing velocity is 2000 m/s, and γ is 0.5. For each model, the shallowest reflector is horizontal, the deepest reflector dips at 80 degrees, and the dip increment is 20 degrees. Since reflectors in both models have opposite dip orientations, we shall refer to models (a) and (b) as the positive- and negative-dip models, respectively.	44
4.2	Synthetic p–sv CMP gathers. (a) and (b) correspond to the middle midpoints of Figures 4.1a and 4.1b, respectively. The downgoing velocity is 2000 m/s, and the velocity ratio is 0.5.	45
4.3	NMO-corrected gathers corresponding to the CMP gathers shown in Figure 4.2. The NMO velocity used is 1485 m/s.	47
4.4	Erroneous CRP gathers obtained by processing the mode-converted data with a conventional TZO algorithm that ignores mode conversion. Only horizontal reflections (shallowest) are properly aligned.	48

4.5	Stacks of erroneous CRP gathers processed by ignoring mode conversion. For both the positive- and negative-dip models, (a) and (b), respectively, reflections from only horizontal reflectors (shallowest) stack properly.	49
4.6	CRP gathers obtained by processing the mode-converted data with the proposed TZO method that honors mode conversion. Flattening of events is superior to that seen in Figure 4.4 where mode conversion was ignored.	50
4.7	Stacks of CRP gathers processed using the mode-converted TZO method. Unlike those shown in Figure 4.5 for the TZO method that ignores mode conversion, the stacks in both (a) and (b) here are comparable to the zero-offset data in Figure 4.1.	51
4.8	CRP gathers processed with a squeezed TZO operator that approximately handles velocity variations with depth. The velocity gradients used in generating the data in (a), (b), (c), and (d) are, respectively, 0.4, 0.5, 0.6, and 0.8 s ⁻¹ . The velocity ratio and the downgoing velocity at the surface are 0.5 and 2500 m/s, respectively. The overall stretch and squeeze factors used here are $\tilde{S}1 = 1.5$ and $\tilde{S}2 = 0.01$, calculated from equation (4.1).	55
4.9	Zero-offset model used to generate synthetic p–sv data. The model shows zero-offset reflections from five reflectors in a medium where velocity varies linearly with depth. The downgoing velocity at the surface and the gradient of the downgoing velocity are 2500 m/s and 0.7 s ⁻¹ , respectively, and the sv–p velocity ratio is 0.5. The shallowest reflector is horizontal, the deepest reflector dips at 80 degrees, and the dip increment is 20 degrees.	56
4.10	Synthetic p–sv CMP gather (a), and (b) after applying NMO correction. Both gathers correspond to the middle midpoint of Figure 4.9. The downgoing velocity at the surface and the downgoing-velocity gradient are 2500 m/s and 0.7 s ⁻¹ , respectively; the velocity ratio is 0.5.	57
4.11	CRP gathers corresponding to the NMO-corrected gather of Figure 4.10b. (a) is obtained by processing the mode-converted data with a conventional TZO algorithm that ignores mode conversion. Only the horizontal reflection (shallowest) is properly aligned. (b) is the same gather obtained by applying the mode-converted TZO method.	59

4.12 Stacks of CRP gathers. The data in (a) were processed by ignoring mode conversion; those in (b) were processed using the mode-converted TZO method. Reflections from only the horizontal reflector (shallowest) stack properly when mode conversion is ignored (a). The mode-converted TZO method produces a stack that has the same structure as that of the zero-offset model depicted in Figure 4.9. 60

4.13 CRP gathers corresponding to the CRP gather depicted in Figure 4.8b, but now processed using different stretch and squeeze factors. The overall stretch and squeeze factors in (a) are $\tilde{S}1 = 3.0$ and $\tilde{S}2 = 0.025$; those in (b) are $\tilde{S}1 = 5.0$ and $\tilde{S}2 = 0.04$ 61

4.14 CRP gather of Figure 4.11b, but now processed erroneously. The velocity ratio used in (a) is 20% too high (0.6), that in (b) is 20% too low (0.4), both relative to the correct value $\gamma = 0.5$ 63

4.15 CRP gather of Figure 4.6b, but now processed erroneously. The velocity ratio used in (a) is 5% too high (0.525), that in (b) is 5% too low (0.475), both relative to the correct ratio $\gamma = 0.5$ 65

4.16 CRP gather of Figure 4.6b, but now processed erroneously. The velocity ratio used in (a) is 10% too high (0.55), that in (b) is 10% too low (0.45), both relative to the correct ratio $\gamma = 0.5$ 66

5.1 Conventional stack of Line 1 with no TZO. In the acquisition of the data here, the receivers are situated to the right of the source. 72

5.2 Conventional stack of Line 2 with no TZO. In the acquisition of the data here, the receivers are situated to the left of the source. 72

5.3 Unstacked gathers corresponding to midpoint 100 of Line 1. The CMP gather with only preprocessing applied is shown in (a). CRP gathers, after undoing the NMO correction, are shown in (b), (c), (d), and (e), with velocity ratios 1.0, 0.6, 0.5, and 0.4, respectively. 75

5.4 Unstacked gathers corresponding to midpoint 150 of Line 1. The CMP gather with only preprocessing applied is shown in (a). CRP gathers, after undoing the NMO correction, are shown in (b), (c), (d), and (e), with velocity ratios 1.0, 0.6, 0.5, and 0.4, respectively. 76

5.5 Unstacked gathers corresponding to midpoint 275 of Line 1. The CMP gather with only preprocessing applied is shown in (a). CRP gathers, after undoing the NMO correction, are shown in (b), (c), (d), and (e), with velocity ratios 1.0, 0.6, 0.5, and 0.4, respectively. 77

5.6 Stack of TZO-corrected data of Line 1, assuming $\gamma = 0.4$ 81

5.7 Stack of TZO-corrected data of Line 2, assuming $\gamma = 0.4$ 82

5.8 Stack of TZO-corrected data of Line 1 assuming $\gamma = 1$ (no mode conversion). 83

5.9 Stack of TZO-corrected data of Line 2 assuming $\gamma = 1$ (no mode conversion). 84

5.10 Contours of stacking velocities for Line 1. (a) processing with no TZO; (b) mode-converted TZO; (c) conventional TZO. 85

5.11 Contours of stacking velocities for Line 2. (a) processing with no TZO; (b) mode-converted TZO; (c) conventional TZO. 87

5.12 Stack of conventional CMP gathers (Line 1), but using NMO velocity obtained after mode-converted TZO has been applied. 88

5.13 Stack of conventional CMP gathers (Line 2), but using NMO velocity obtained after mode-converted TZO has been applied. 89

6.1 Depth section depicting mode-converted reflection. Here, $2h$ is the offset distance between source s and receiver g . The midpoint is located at the surface point $x = 0$. The downgoing and the upgoing velocities are, respectively, v and γv . The equivalent zero-offset trace, for this geometry, is located a distance b from the midpoint. 93

6.2 (a) representative synthetic CMP gather over a horizontal reflector at 400-m depth. (b) output $k-t_1$ gather, with severely distorted amplitude and phase. The input data are ordinary p-wave ($\gamma = 1$) synthetic CMP gathers, and the medium velocity is 1000 m/s. 95

6.3 Fresnel-zone width for the $k-t_1$ gather depicted in Figure 6.2b. The Fresnel zone increases with increasing k in the time window 0.8 – 1.25 s for the range of k shown in (a). In (b), the Fresnel-zone width decreases as k (large) increases for the same time window. Corners seen on the curves are explained in Appendix E. 97

6.4	Contributions from many midpoints to a single output trace in the $k-t_1$ domain. In this example, the stack of this gather forms the trace whose offset is 600 m in Figure 6.2b. The locations of contributing midpoints are relative to the location of the output $k-t_1$ gather. . . .	98
6.5	The $k-t_1$ gather of Figure 6.2b is flattened after applying a constant-velocity NMO correction to the data. The velocity used is the medium velocity, 1000 m/s.	99
6.6	Schematic diagram showing the relationship between the physical and the nonphysical half-offsets as given in equation (6.3). Here, circles represent constant, physical half-offsets. The maximum physical and nonphysical half-offsets are H and k_m , respectively.	101
6.7	The problem with large- k traces. The event in (a) is hyperbolic for all k values because the reflector is horizontal with no mode-converted waves. When the reflector is dipping, or when mode conversion is present, large- k traces become erroneous (i.e., nonhyperbolic), as depicted in (b), (c), and (d). In (b), the reflector dips at 20° downward from source to receiver. Events in (c) and (d) show the problem for mode-converted waves; the reflector in (c) is horizontal, whereas that in (d) dips at 20° downward from source to receiver.	103
6.8	Analysis in the $k-t_1$ domain for a reflector dipping at 25° , downward from source to receiver. (a) output $k-t_1$ gather; (b) same gather after filtering; (c) NMO-corrected gather ($v = 1370$ m/s); (d) stacked trace.	107
6.9	Analysis in the $h-t$ domain for a reflector dipping at 25° , downward from source to receiver. (a) CMP gather at the location where velocity is analyzed; (b) NMO-corrected gather ($v = 1200$ m/s); (c) stacked trace.	108
6.10	Analysis in the $k-t_1$ domain for a horizontal reflector. (a) output $k-t_1$ gather; (b) same gather after filtering; (c) NMO-corrected gather ($v = 1350$ m/s); (d) stacked trace.	109
6.11	Analysis in the $h-t$ domain for a horizontal reflector. (a) CMP gather at the location of the velocity analysis; (b) NMO-corrected gather ($v = 1480$ m/s); (c) stacked trace.	110
6.12	Analysis in the $k-t_1$ domain for a dipping reflector (dip= 25° , upward from source to receiver). (a) output $k-t_1$ gather; (b) same gather after filtering; (c) NMO-corrected ($v = 1360$ m/s); (d) stacked trace.	112

6.13	Analysis in the $h-t$ domain for a dipping reflector (dip= 25° , upward from source to receiver). (a) input CMP gather; (b) NMO-corrected gather ($v = 2450$ m/s); (c) stacked trace.	113
A.1	Depth section depicting a mode-converted, reflection raypath in a homogeneous medium with a dipping reflector.	121
B.1	Depth section depicting a mode-converted, reflection raypath in a homogeneous medium with a dipping reflector.	124
D.1	Depth section depicting a raypath for p-sv mode conversion. The trace has offset $2h$ between source s and receiver g . The distance from the midpoint y to the dipping reflector is D_y , and that from b (the location of an equivalent zero-offset trace) to the reflector is D . The distance from s along the raypath to the reflector is l_s , and that from the reflector to g is l_g . The incidence and reflection angles are θ_s and θ_g , respectively, and reflector dip is θ	133
E.1	Subsurface model consisting of a single dipping reflector in a constant-velocity medium. An output $k-t_1$ gather is desired at location a . Any midpoint y with source-receiver ($s-g$) offset ($2h$) encompassing point a will contribute to the output $k-t_1$ gather. The zero-offset time, which the $k-t_1$ gather inherits, is experienced along path D	137
F.1	Surface of constant traveltime (pseudo-ellipse) for a mode-converted wave. The range of b corresponding to possibly recorded seismic data is along the line connecting source s and recorder g , but shorter than offset $2h$	142

Chapter 1

INTRODUCTION

Zero-offset seismic data (source and receiver being at the same location) are rarely recorded in practice. In reflection seismology, receivers are typically placed a finite distance, i.e., offset, from the source. The need for transformation of such data to zero offset (TZO) often arises when a particular processing scheme, poststack migration for example, presumes that the input seismic data are zero-offset.

The moveout velocity of p-wave reflections is known to be dip-dependent (Levin, 1971). Normal moveout (NMO) correction based on some choice of moveout velocity will, therefore, correct reflections from reflectors with only certain dips—the dips with which the moveout velocities are associated. Consequently, mapping of seismic data to zero-offset based on NMO correction alone tends to enhance reflections with certain zero-offset slopes at the expense of other slopes (Hale, 1984). The solution to this problem is to apply a TZO method that is valid for all dips.

TZO of prestack seismic data for constant-velocity media is well understood and is readily implemented when dealing with either p-waves or s-waves. TZO is achieved by inserting a dip-moveout (DMO) process to correct data for the influence of dip, either before or after NMO correction. The TZO process transforms prestack seismic data in such a way that common midpoint (CMP) gathers are closer to being common reflection point (CRP) gathers after the transformation.

Several TZO methods are currently used in processing ordinary p-wave seismic data. One such method is implemented by applying the DMO correction in the

frequency-wavenumber ($f-k$) domain to NMO-corrected data (Hale, 1984). TZO can also be applied to NMO-corrected data in the space-time domain, in which case the TZO method is referred to as a *Kirchhoff* or *integral* method (Hale, 1991). Another approach, which achieves TZO by first applying DMO correction to prestack seismic data and, second, applying NMO correction, is implemented in a domain (Forel and Gardner, 1988) that is nonphysical in the sense that processed traces have been mapped to new “offset” and “time” domain that differs from true source-receiver offset and reflection time.

Converted (p-sv or sv-p) waves differ from ordinary (p-p or s-s) waves in that the downgoing and reflected upgoing waves travel at different velocities, even in isotropic, homogeneous media. As a result, in accordance with Snell’s law, the angle of reflection differs from the angle of incidence at a reflection. This makes the kinematics (time-distance relation, or moveout) more complicated than that encountered in the absence of mode conversion. One way of dealing with this complication is to approximate the moveout of converted waves so that it resembles that of ordinary waves (Sword, 1984). Unfortunately, such an approximation is valid only for small offsets and, consequently, cannot be used to process large-offset seismic data.

A kinematically exact TZO method for mode-converted waves, assuming a constant-velocity medium, was introduced by Harrison (1990). This TZO approach, an integral method, transforms prestack seismic data directly from recorded time to zero-offset time, given prior velocity information. Rather than done as a separate step, the process of NMO correction is embedded in Harrison’s TZO approach. Implementation of TZO for mode-converted waves by methods other than Harrison’s is the task of this thesis. Namely, we shall investigate the possibility, applicability, and efficiency of extending Hale’s $f-k$ TZO, as well as the Forel and Gardner’s approach,

to mode-converted seismic data.

Differences in the actions of mode-converted TZO and conventional (i.e., ordinary p-wave) TZO can be seen by comparing their responses for constant-offset data when the input data consist of all zeros with the exception of a single seismic trace with isolated time impulses. The impulse-response shape of conventional TZO (assuming a constant-velocity medium) is known to be an ellipse (e.g., Deregowski, 1986) in zero-offset time t_0 as a function of the location of the zero-offset output trace relative to the midpoint between source and receiver. For an input seismic trace at midpoint y and with a single impulse at time t_n (NMO-corrected time), the apex of the ellipse is located at the point (y, t_n) . Figure 1.1a shows the impulse responses of conventional TZO for three input time impulses at $y=0$, $t_n=2.0$, 2.8, and 3.6 s, assuming a constant velocity of 2000 m/s. For comparison, when the downgoing and upgoing velocities are 2000 and 1000 m/s, respectively, the trajectories for the response of mode-converted (p-sv) TZO (Harrison, 1990) to the same three time impulses are shown in Figure 1.1b. Note that the impulse-response shapes here are no longer ellipses. Furthermore, each asymmetric impulse response now has its peak shifted, in a time-varying manner, from the midpoint of the input trace.

Den Rooijen (1991) derived an integral operator for mode-converted TZO that is equivalent to Harrison's. He applied his operator to both synthetic and field mode-converted data. Typical of any Kirchhoff implementation, Den Rooijen applied amplitude weighting factors, as well as a phase-compensation filter (rho-filter) in his TZO approach. His synthetic results, though correct from the timing point of view, exhibited aliasing and amplitude variation with offset that he attributed to use of improper weighting factors (Den Rooijen, 1991). As with ordinary p-wave TZO, the aliasing and amplitude shortcoming could have been avoided if the TZO process had

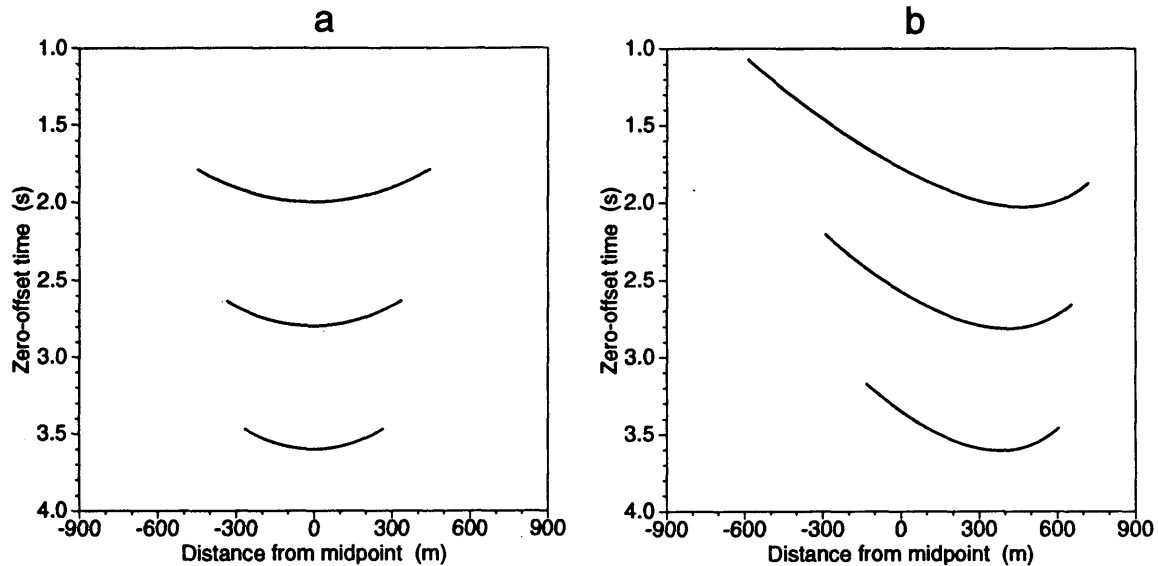


FIG. 1.1. Impulse responses of the TZO process. Conventional TZO yields a response (a) that is an ellipse with apex directly underneath the midpoint, whereas the response of mode-converted TZO (b) is an asymmetric curve whose apex is laterally shifted, in a time-varying manner, relative to the midpoint. Offset is 2000 m. The medium velocity in (a) is 2000 m/s; the downgoing and upgoing velocities in (b) are 2000 and 1000 m/s, respectively.

been implemented in the f - k domain—an alternative investigated in this thesis.

To address the problem of TZO for mode-converted waves, I first analyze the moveout for a constant-velocity medium, obtaining two different moveout relations. The first, which is exact and equivalent to that of Harrison (1990), relates zero-offset time to recorded time and output distance relative to midpoint location (see, for example, Figure 1.1b). In this moveout relation, the dependence of zero-offset time on dip is implicit. The second moveout relation, which is approximate, expresses recorded time as a function of zero-offset time and dip; dependence on dip here is explicit.

The first moveout relation (implicit dip) is used to extend an existing TZO approach, originally developed for ordinary p-waves by Forel and Gardner (1988),

to mode-converted data. While the extension of their approach to mode-converted waves is straightforward, it turns out, unfortunately, that this approach has intrinsic problems that make it unfavorable to implement. These problems are discussed in detail in Chapter 6.

The second moveout relation, though approximate, is attractive because of the explicit dependence of recorded time on dip, thus making it analogous to the well-known moveout relation for ordinary p-waves

$$t^2 = t_0^2 + \frac{x^2}{v^2} - \frac{x^2 \sin^2 \theta}{v^2},$$

as given by Levin (1971), where t is recorded time, t_0 is zero-offset time, x denotes source-receiver offset, v is velocity, and θ is the dip. Analysis of the approximate moveout relation for mode conversion reveals that TZO for mode-converted waves can be implemented in the f - k domain in much the same way as for ordinary p-waves (Hale, 1984), with little modification.

The impulse response (the operator), for the first stage of the f - k TZO method is analytically found to be a “squeezed” ellipse (relative to that of ordinary p-waves) that is laterally shifted in space. The lateral shift of this approximate operator is time-invariant and is a constant for a given offset. The exact operator seen in Figure 1.1b, however, is nonelliptical and has a time-variant lateral shift. The incorrect position and shape for the approximate operator arise because the f - k TZO method is only approximate. Therefore, I modify this approximate f - k TZO operator by, first, accounting for the lateral shift of the conversion point for horizontal reflectors as a function of time and, second, altering the shape of the resulting TZO operator to make it better resemble the behavior of that for mode conversion.

Application of this f - k TZO method to synthetic, mode-converted seismic data

reveals that this method is capable, to a great extent, of transforming mode-converted data to zero offset, even when velocity changes with depth. In contrast, conventional TZO (ignoring mode conversion) fails to correct mode-converted data and, in some cases, yields poorer results than when the data are simply NMO corrected. The method is not too sensitive to the choice of velocity ratio, but mode conversion must be taken into account. Not only does the method TZO-correct reflections from dipping reflectors regardless of the sign of dip, but also reflections from horizontal reflectors, too, in which case the reflections are laterally shifted to their appropriate zero-offset locations.

I also tested the method on two field data sets, acquired in the same region but shot in opposite directions, with dominantly p-sv reflections. The signal-to-noise ratio was poor in both sets and reflection dips did not exceed about 25 degrees, so that improvement with mode-converted TZO was not as dramatic as that for the synthetic data tests. Nevertheless, the method has significantly removed the influence of dip from stacking velocity, and yielded better stacks than either the conventional CMP stack or the stack for conventional TZO. Neither conventional processing (no TZO) nor conventional TZO (ignoring mode conversion) was able to dip-correct velocity as well as did mode-converted TZO.

As an example from the synthetic tests, Figure 1.2 shows a CRP gather after applying conventional $f-k$ TZO to mode-converted seismic data. The choice of NMO velocity used here was such that it would match that typically made in practice, i.e., a velocity obtained from velocity analysis based on only horizontal reflections. Consequently, only reflections from the horizontal reflector (shallowest) are properly corrected (i.e., horizontally aligned). Reflections from dipping reflectors are severely overcorrected and, consequently, will not produce an acceptable stack. Note, also,

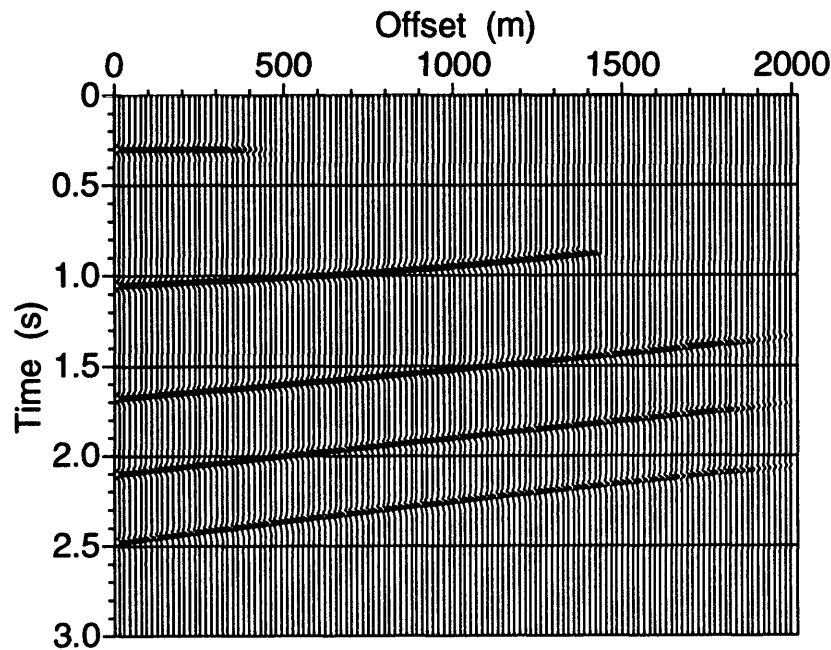


FIG. 1.2. CRP gather obtained by applying conventional TZO (ignoring mode conversion) to mode-converted data. For these synthetic data, the downgoing and upgoing velocities are 2000 and 1000 m/s, respectively. The gather shows reflections from five reflectors with dips starting at 0 degrees (shallowest reflector) with an increment of 20 degrees; the dip of the deepest reflector is 80 degrees.

that their residual moveouts do not even show the curvature familiar in overcorrected p-wave data. The same CRP gather is shown in Figure 1.3, but processed now by applying the $f-k$ TZO method proposed here, thus honoring mode conversion. Reflections from all reflectors, including the deepest one, which dips at 80 degrees, are now correctly aligned. Clearly, this CRP gather will produce a better stack than will that of Figure 1.2.

The previous two examples illustrate the necessity of incorporating a mode-converted TZO, such as the one proposed here, for the processing of mode-converted seismic data. Although Den Rooijen (1991) qualitatively showed that his integral TZO method was quite sensitive to the choice of the velocity ratio, he did not, nor

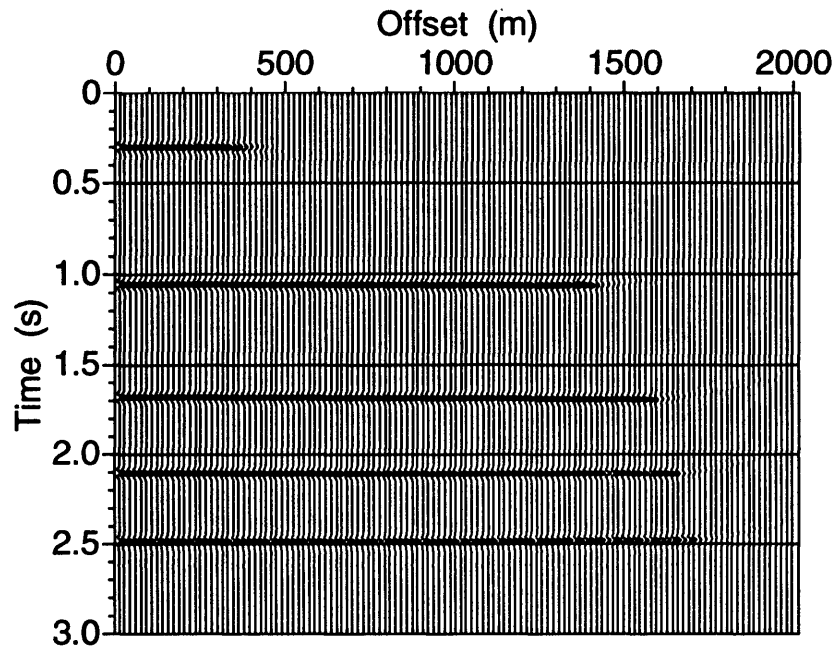


FIG. 1.3. CRP gather obtained by applying mode-converted TZO to the same mode-converted data shown in Figure 1.2. Reflections are now correctly aligned, including those from the steepest (deepest) reflector, which dips at 80 degrees.

did Harrison (1990), investigate the consequence of ignoring mode conversion when mode-converted data are considered. To bridge the gap, we shall, throughout this thesis, compare TZO results from two methods: the conventional TZO method that does not honor mode conversion, and the mode-converted TZO method proposed here. As we shall see, mode-converted data should never be processed with a TZO algorithm that ignores mode conversion.

For many rocks, the velocity of shear wave v_s is approximately half that of the compressional wave v_p (Dobrin and Savit, 1988). For this reason, I choose a velocity ratio $v_s/v_p = 0.5$ for most of the examples in this thesis.

Chapter 2

THE KINEMATICS OF CONVERTED WAVES

2.1 Introduction

Before analyzing TZO for mode-converted waves, we first address the time-distance (moveout) relation in the presence of both dip and mode conversion. Two moveout relations are derived here, both assuming a constant-velocity medium.

The first relation, which is exact, relates zero-offset time to both recorded time and the location of an output zero-offset trace. This relation, in which there is no immediate time dependence on dip, is referred to as an *implicit-dip* relation. Based on this moveout relation, derivation of TZO in the nonphysical domain introduced by Forel and Gardner (1988) is given in Chapter 6.

The second moveout relation, which is derived by approximating a power series, expresses travelttime as a function of zero-offset time and *dip*. Although not exact, this *explicit-dip* moveout relation will eventually pave the way for deriving a TZO method for mode-converted waves by Fourier transform.

2.2 Implicit-dip relation

From geometrical considerations, the equation describing the two-way travelttime for a converted wave can be written as

$$t = \frac{\sqrt{(x+h)^2 + z^2}}{v} + \frac{\sqrt{(x-h)^2 + z^2}}{\gamma v}, \quad (2.1)$$

where

- (x, z) : coordinates of the reflection point,
- h : half-offset between source and receiver along the surface $z = 0$,
- v : velocity for the path from the source to the reflector,
- γv : velocity for the path from the reflector to the receiver ($\gamma < 1$ implies p-sv conversion, and $\gamma > 1$ implies sv-p conversion).

Figure 2.1 shows the geometry pertaining to equation (2.1). In that figure, the mid-

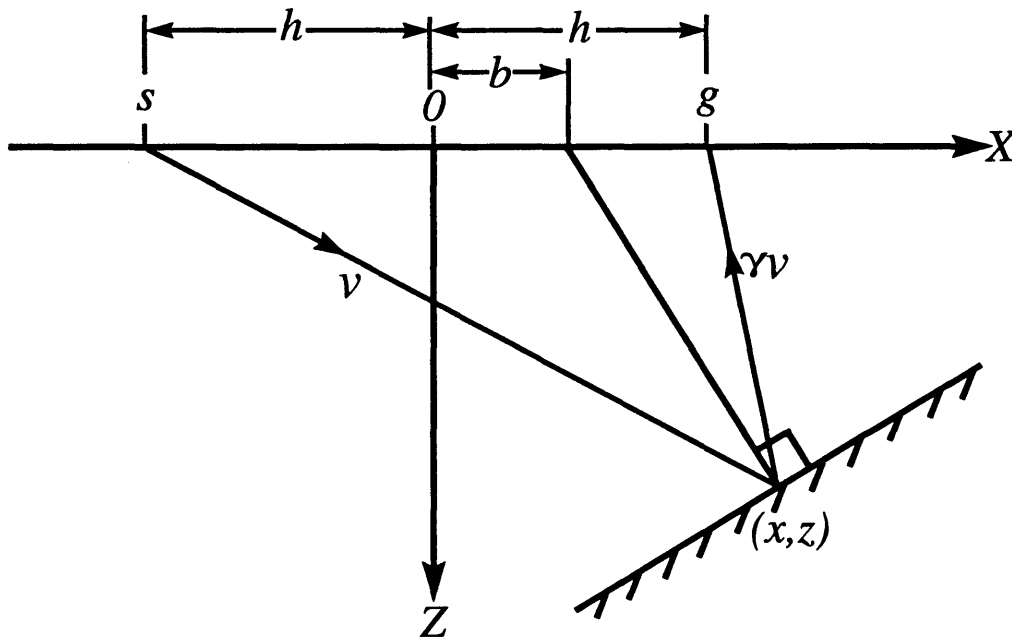


FIG. 2.1. Depth section depicting a mode-converted, reflection raypath in a homogeneous medium with a dipping reflector.

point is at the origin, s denotes the source location, and g denotes the receiver location. Unlike the situation for ordinary p-waves, for mode-converted waves the angles of incidence and reflection differ (i.e., symmetry is broken), as shown in the figure. A line

passing through reflection point (x, z) , and perpendicular to the reflector, crosses the surface at point b relative to the midpoint. To convert CMP gathers to CRP gathers, TZO must move the nonzero-offset reflection to a location that is at the distance b from the original midpoint (Hale, 1988) and has the time of that for two-way travel from $(b, 0)$ to (x, z) .

Following Sword (1984), we obtain z^2 from equation (2.1) as

$$z^2 = \frac{1}{\beta^2} \left\{ -\beta \left[(x+h)^2 - \frac{1}{\gamma^2} (x-h)^2 \right] + \alpha (vt)^2 - \frac{2vt}{\gamma} \sqrt{(vt)^2 - 4\beta xh} \right\}, \quad (2.2)$$

where

$$\begin{aligned} \alpha &\equiv 1 + \frac{1}{\gamma^2}, \\ \beta &\equiv 1 - \frac{1}{\gamma^2}. \end{aligned} \quad (2.3)$$

For constant γ , h , v , and t , the graph of z versus x looks like a distorted ellipse. An example of such a *pseudo-ellipse* is shown in Figure 2.2.

At an arbitrary subsurface reflection point (x, z) on the pseudo-ellipse (Figure 2.3), construct the circle that is tangent to the pseudo-ellipse and has its center along the line connecting the source and receiver. Let the radius of the circle be R , such that the center is at the point $(b, 0)$. The equation describing the circle is thus

$$(x - b)^2 + z^2 = R^2. \quad (2.4)$$

To satisfy the tangency requirement, the slope of the pseudo-ellipse and that of the circle must be the same at the point of tangency. Differentiating equations (2.2)

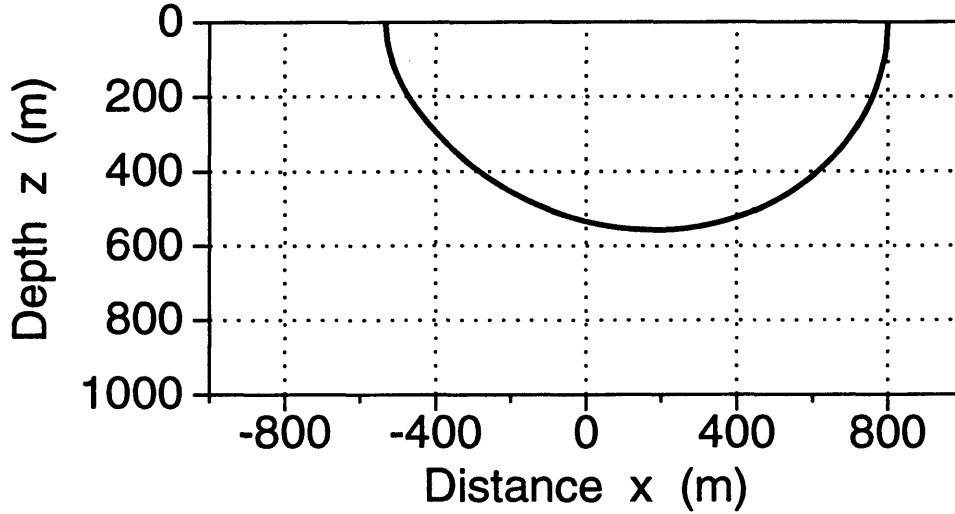


FIG. 2.2. The locus of z as a function of x looks somewhat like an ellipse, for constant γ , h , v , and t . Here $\gamma=0.5$, $h=400$ m, $v=2000$ m/s, and $t=1$ s. The midpoint is located at $x=0$.

and (2.4) with respect to x yields, respectively,

$$z \frac{dz}{dx} = \frac{1}{\beta^2} \left\{ -\beta \left[(x+h) - \frac{1}{\gamma^2}(x-h) \right] + \frac{vt}{\gamma} \frac{2\beta h}{\sqrt{(vt)^2 - 4\beta x h}} \right\}, \quad (2.5)$$

and

$$(x-b) + z \frac{dz}{dx} = 0. \quad (2.6)$$

Now, from equations (2.2), (2.4), (2.5), and (2.6), the radius R can be obtained as a function of (v, t, γ, b, h) . Specifically, using equations (2.2) and (2.4) to eliminate z^2 , using equations (2.5) and (2.6) to eliminate $z dz/dx$, and after some algebra and

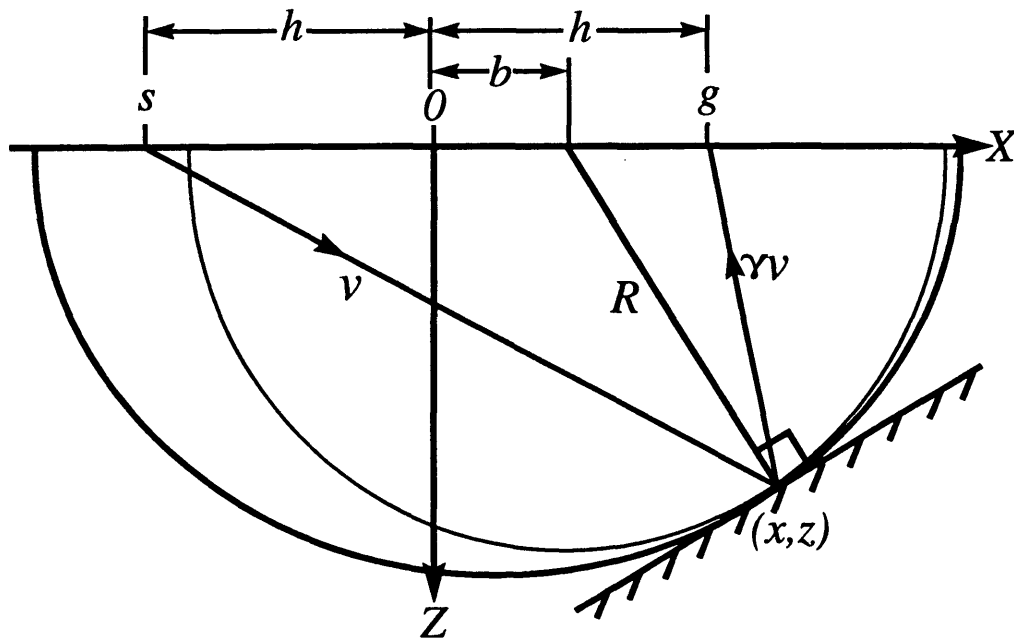


FIG. 2.3. A circle with radius R and center at $(b, 0)$ is tangent to the pseudo-ellipse at reflection point (x, z) . The distance b from the midpoint is the same as that in Figure 2.1.

simplification, we obtain

$$R^2 = (h^2 - b^2) \left[\frac{(vt)^2}{2h(\alpha h + \beta b)} - 1 \right]. \quad (2.7)$$

Harrison (1990) derived a result that is equivalent to equation (2.7), differing only in that the downgoing and upgoing velocities are used explicitly. Figure 2.4 shows how the pseudo-ellipse of Figure 2.2 is constructed as the envelope of circles whose radii are calculated from equation (2.7).

Referring to Figure 2.3, for mode-converted waves (ignoring the fact that mode conversion does not truly occur at normal incidence) the two-way normal-incidence

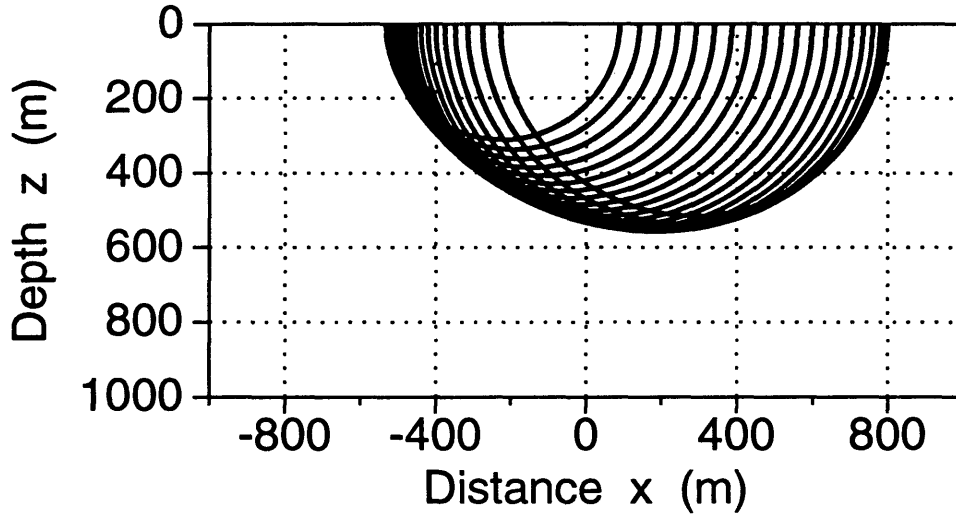


FIG. 2.4. The curve of Figure 2.2 is constructed from circles whose radii are given by equation (2.7).

time associated with reflection point (x, z) is given by

$$t_0 = \frac{R}{v} + \frac{R}{\gamma v} = \frac{R}{v} \left(1 + \frac{1}{\gamma} \right),$$

or

$$t_0 = \frac{2R}{v_a}, \quad (2.8)$$

where the *average velocity* v_a is given by

$$v_a \equiv \frac{2v}{\sigma}, \quad (2.9)$$

with

$$\sigma \equiv 1 + \frac{1}{\gamma}. \quad (2.10)$$

Substitution of equations (2.8) and (2.9) for R in equation (2.7) yields the following expression for zero-offset time

$$t_0^2 = (h^2 - b^2) \left[\frac{(\sigma t)^2}{2h(\alpha h + \beta b)} - \left(\frac{2}{v_a} \right)^2 \right]. \quad (2.11)$$

For a given offset h , relationship (2.11) between t_0 and b defines the trajectory of the response of the TZO process to an impulse at the source-receiver midpoint and at time t (i.e., the shape of the TZO operator). Figure 2.5 is a plot of this function for the same parameters used in Figure 2.2. Note that equation (2.11) reduces to an

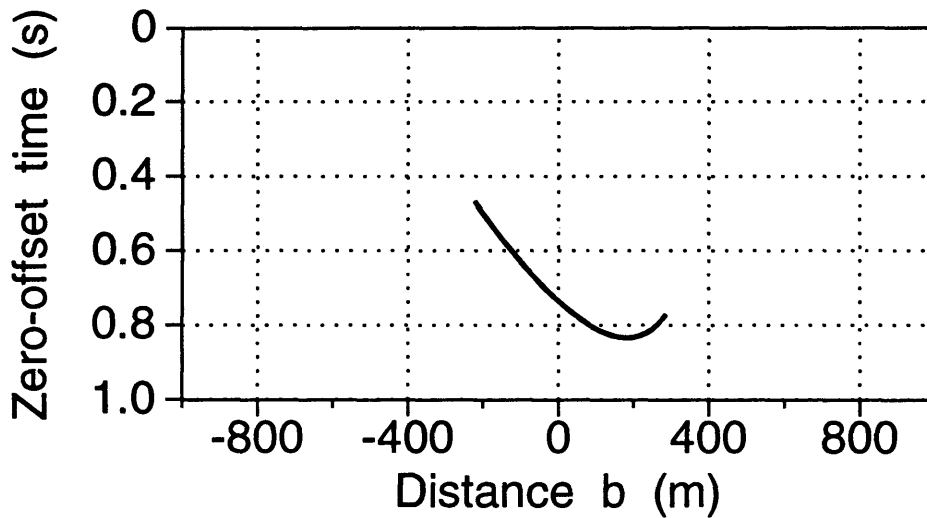


FIG. 2.5. Shape of the impulse response $t_0(b)$ of the TZO operation for an impulse at time $t=1$ s. The parameters here are the same as those in Figure 2.2.

ellipse in (t_0, b) when $\gamma = 1$ (i.e., $\beta = 0$). For $\gamma \neq 1$, however, we once again observe the broken symmetry for mode-converted data.

If the average velocity v_a is known, equation (2.11) can be used to transform prestack seismic data directly from recorded time t to zero-offset time t_0 (Harrison, 1990). Furthermore, equation (2.11) can also be used to extend to mode conversion the principles underlying the velocity-independent DMO approach introduced by Forel and Gardner (1988) for ordinary p-waves; the DMO correction in this case depends only on the velocity *ratio*, and not on the individual p- and sv-wave velocities themselves. Detailed explanation is given in Chapter 6.

Since the operator given by relation (2.11) is exact, it will be used as a standard against which to compare an approximate TZO operator derived in the next chapter.

2.3 Explicit-dip relation

For ordinary p-waves, and in a constant-velocity medium, traveltimes can be expressed as an explicit function of offset, zero-offset time, velocity, and reflector dip (Levin, 1971). This relation, the well-known hyperbolic moveout equation, is used as the basis in deriving TZO by Fourier transform for ordinary p-waves (Hale, 1984). For mode-converted waves, to formulate a TZO operator in the frequency-wavenumber domain we need a similar moveout relationship in which time explicitly depends on dip. An exact moveout relation was introduced in the previous section, equation (2.11). Unfortunately, unlike the situation for ordinary p-waves, the derived traveltimes expression for mode-converted waves is not an explicit function of dip. To make progress, I next derive an approximate dip-dependent moveout relationship.

The derivation is based on the model of a single dipping reflector in a constant-velocity medium, as shown in Figure 2.6. In that figure, the offset between source s and geophone g is x . The quantity D designates the distance from the midpoint y (between s and g) to the reflector, whose dip angle is θ . The angles between the

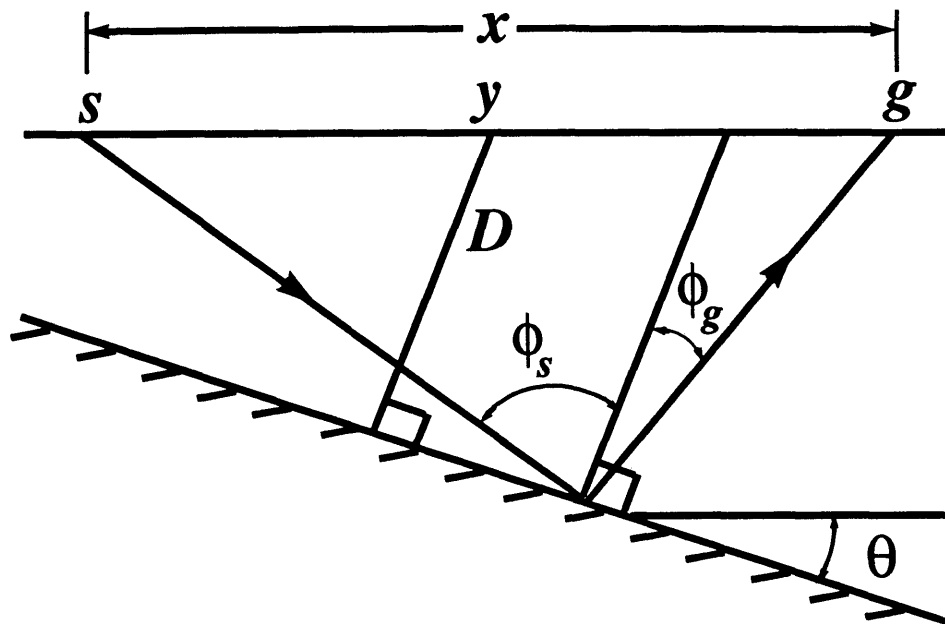


FIG. 2.6. Depth section depicting a mode-converted, reflection raypath in a homogeneous medium with a dipping reflector.

normal to the reflector and the incident and reflected (mode-converted) rays are, respectively, ϕ_s and ϕ_g . From the geometry of the figure, offset x can be expressed (Appendix A) as

$$x = \frac{2D(\tan \phi_s + \tan \phi_g)}{2 \cos \theta + \sin \theta (\tan \phi_s - \tan \phi_g)}. \quad (2.12)$$

With the downgoing and reflected waves traveling at speeds v and γv , respectively, the traveltimes for the reflection is then given (Appendix A) by

$$t = \frac{1}{v} \left[D \left(\frac{1}{\cos \phi_s} + \frac{1}{\gamma \cos \phi_g} \right) + \frac{x \sin \theta}{2} \left(\frac{1}{\gamma \cos \phi_g} - \frac{1}{\cos \phi_s} \right) \right]. \quad (2.13)$$

The angles ϕ_s and ϕ_g can be expressed in terms of a slowness parameter ν along the

dipping interface, using Snell's law:

$$\nu = \frac{\sin \phi_s}{v} = \frac{\sin \phi_g}{\gamma v}. \quad (2.14)$$

In the presence of dip, and unlike that for ordinary p-waves, traveltimes for mode-converted waves is no longer an even function of offset within a CMP gather. That is, considering p–sv conversion for example, interchanging s and g in Figure 2.6 yields a different raypath and, with it, a different traveltimes. The dependence of time t on offset x can thus be expressed in the following series form

$$t^2 = c_0 + c_1 x + c_2 x^2 + c_3 x^3 + \dots, \quad (2.15)$$

which includes both odd and even powers of x . In the absence of mode conversion, this power series expression would contain only even powers of x .

Equations (2.12) and (2.13) can be expressed in terms of the slowness parameter ν by substituting for ϕ_s and ϕ_g their values from equation (2.14). Consequently, t^2 , x , x^2 , x^3 , ..., are expressed as power series (Taylor expansion) in the same slowness parameter ν (Appendix B). After substitution of those expressions into equation (2.15), the coefficients c_i can then be recursively solved for by matching like powers of ν . The first five coefficients (Appendix B) are

$$\begin{aligned} c_0 &= \left(\frac{2D}{v_a} \right)^2 \equiv t_0^2, \\ c_1 &= \frac{2(1-\gamma)t_0 \sin \theta}{(1+\gamma)v_a}, \\ c_2 &= \frac{4\gamma \cos^2 \theta + (1-\gamma)^2 \sin^2 \theta}{(1+\gamma)^2 v_a^2}, \\ c_3 &= \frac{8\gamma(1-\gamma) \cos^2 \theta \sin \theta}{(1+\gamma)^3 t_0 v_a^3}, \end{aligned}$$

$$c_4 = \frac{4\gamma(1-\gamma)\cos^2\theta[(\gamma-1)\cos^2\theta + (2-2\gamma-\gamma^2)\sin^2\theta]}{(1+\gamma)^4 t_0^2 v_a^4},$$

where v_a is the same average velocity given by equation (2.9), i.e.,

$$\frac{2}{v_a} = \frac{1}{v} + \frac{1}{\gamma v}.$$

If the series in equation (2.15) is truncated beyond the third term, the approximate moveout relationship, after some algebra and trigonometric substitution, becomes

$$t^2 = t_0^2 + \frac{2(1-\gamma)t_0 x \sin\theta}{(1+\gamma)v_a} + \frac{4\gamma x^2}{(1+\gamma)^2 v_a^2} + \frac{[(1-\gamma)^2 - 4\gamma]x^2 \sin^2\theta}{(1+\gamma)^2 v_a^2}. \quad (2.16)$$

This relation is clearly an even function of neither offset nor dip. Note that when $\gamma = 1$ (no mode conversion), equation (2.16) reduces to

$$t^2 = t_0^2 + \frac{x^2}{v^2} - \frac{x^2 \sin^2\theta}{v^2}, \quad (2.17)$$

the well-known hyperbolic moveout relation for ordinary p-waves as given by Levin (1971).

Hale (1984) exploited the moveout relation given by equation (2.17) to derive a TZO method for ordinary p-waves by Fourier transform. In much the same way as for Hale's f - k TZO method, equation (2.16) will next be used as the basis to facilitate the derivation of TZO for mode-converted waves by Fourier transform.

Chapter 3

TZO BY FOURIER TRANSFORM

3.1 Introduction

Analogous to Hale's f - k TZO method for ordinary p-waves (reviewed here), I use the approximate moveout relation given by equation (2.16) to derive a TZO algorithm for mode-converted waves in the frequency-wavenumber domain. Since this f - k TZO, as with Hale TZO, requires that the input prestack seismic data be NMO-corrected, I will discuss NMO-corrected time and NMO velocity for mode-converted waves. Then, after deriving an initial, approximate f - k TZO formulation, I shall introduce modifications necessary to obtain the desired TZO action.

3.2 Hale f - k TZO

For ordinary p-waves, the moveout relation given by equation (2.17) is exact for a constant-velocity medium. This moveout relation is the basis for Hale f - k TZO. A review of Hale f - k TZO is given here.

Following Hale (1984), NMO-corrected time t_n is related to recorded time t by

$$t_n^2 = t^2 - \frac{4h^2}{v^2}, \quad (3.1)$$

where half-offset h , given by $x/2$, is introduced here for convenience. t_n in equation (3.1) is, by definition, the conventional NMO-corrected time. For a given seismic

trace with midpoint y , it is assumed that the NMO-corrected and the recorded seismograms, p_n and p , respectively, are related by $p_n(t_n, y, h) = p(t, y, h)$. With NMO-corrected time t_n so defined, it follows from equation (2.17) that zero-offset time, t_0 , can be expressed in terms of t_n as

$$t_0^2 = t_n^2 + \frac{4h^2 \sin^2 \theta}{v^2}. \quad (3.2)$$

For a constant half-offset h , the 2-D Fourier transform of the unknown zero-offset seismograms, $p_0(t_0, y, h)$, is defined by

$$P_0(\omega, k, h) = \int dt_0 e^{i\omega t_0} \int dy e^{-iky} p_0(t_0, y, h). \quad (3.3)$$

Using the change of variables given by equation (3.2), the integration over the unknown t_0 in the above transform is replaced by integrating over the known t_n . Taking advantage of the relations for the zero-offset slope ($\Delta t_0 / \Delta y$) in the physical and Fourier domains, i.e.,

$$\frac{\Delta t_0}{\Delta y} = \frac{2 \sin \theta}{v} = \frac{k}{\omega},$$

it follows from (3.2) that

$$A \equiv \frac{dt_n}{dt_0} = \sqrt{1 + \frac{h^2 k^2}{t_n^2 \omega^2}},$$

and the transformation in (3.3) can then be written as

$$P_0(\omega, k, h) = \int dt_n A^{-1} e^{i\omega A t_n} \int dy e^{-iky} p_n(t_n, y, h). \quad (3.4)$$

Finally, the desired zero-offset data $p_0(t_0, y, h)$ are obtained by 2-D inverse transfor-

mation of equation (3.4) as follows

$$p_0(t_0, y, h) = \frac{1}{(2\pi)^2} \int d\omega e^{-i\omega t_0} \int dk e^{iky} P_0(\omega, k, h).$$

The impulse response in the t - y domain of this TZO method is obtained by finding the 2-D inverse transform of equation (3.4) when $p_n(t_n, y, h)$ is an impulse. The impulse response is known to be an ellipse (Hale, 1988) given by

$$\left(\frac{t_0}{t_n}\right)^2 + \left(\frac{y_0}{h}\right)^2 = 1, \quad (3.5)$$

where y_0 denotes the location of the output zero-offset trace relative to the original input midpoint. This elliptical relation between t_0 and y_0 is well known in reflection seismology and is frequently referred to as the DMO ellipse.

3.3 NMO-corrected time and NMO velocity for converted waves

Let us call the third term in equation (2.16), which has no dip dependence, T^2 . That is, in terms of half-offset h , we have

$$T^2 \equiv \frac{16\gamma h^2}{(1 + \gamma)^2 v_a^2}. \quad (3.6)$$

For ordinary p-waves ($\gamma = 1$), this term reduces to

$$T^2 = \frac{4h^2}{v^2}, \quad (3.7)$$

where v is the medium velocity. So, for $\gamma = 1$ (no mode conversion), the quantity $t^2 - T^2$ reduces to t_n^2 , given by equation (3.1), which is the square of the conventional NMO-corrected time for ordinary p-waves. Similarly for mode-converted waves, define

NMO-corrected time t_n by

$$t_n^2 \equiv t^2 - T^2, \quad (3.8)$$

where t is the recorded time given by relation (2.16). For a given seismic trace with midpoint y , it is also assumed here that the recorded and the NMO-corrected seismograms, p and p_n , respectively, are related by $p_n(t_n, y, h) = p(t, y, h)$.

Again, for $\gamma = 1$, the constant medium velocity v in equation (3.7) is also the NMO velocity. Similarly, the NMO velocity for mode-converted waves can be deduced from the term T^2 ($\gamma \neq 1$) by writing equation (3.6) as

$$T^2 = \frac{4h^2}{v_{nmo}^2},$$

where the NMO velocity v_{nmo} is then given by

$$v_{nmo}^2 = \frac{(1 + \gamma)^2 v_a^2}{4\gamma}.$$

Then, using equation (2.9), we get

$$v_{nmo} = \sqrt{\gamma} v. \quad (3.9)$$

Recalling that v and γv are the downgoing and upgoing velocities, respectively, the NMO velocity given by equation (3.9) is thus the geometric mean of these two velocities.

In practice, however, the “stacking” velocity required to flatten mode-converted reflections from horizontal reflectors is somewhat higher than v_{nmo} given by equation (3.9). For a velocity ratio $\gamma = 0.5$, for example, and assuming a maximum source-receiver offset of 4000 m, a 5% increase over the proposed v_{nmo} above is needed

to approximately flatten reflections from horizontal reflectors, even in media where velocity changes with depth. Figure 3.1 shows a constant-velocity example. Although

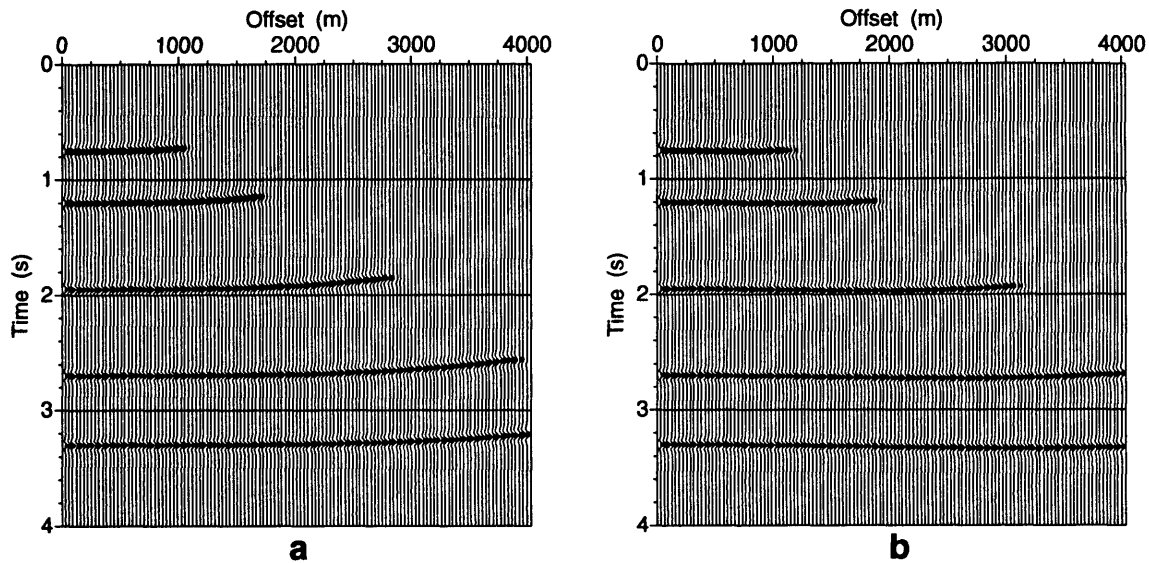


FIG. 3.1. CMP gather showing reflections from five horizontal reflectors after NMO correction. The NMO velocity in (a), which did not quite align reflections, is calculated directly from equation (3.9) for $v = 2000$ m/s and $\gamma = 0.5$. The NMO velocity in (b), which is 5% higher than that in (a), yields better alignments.

reflections are better corrected using a slightly higher NMO velocity, alignment is still imperfect and nonelliptical, as shown in Figure 3.1b. This shortcoming stems directly from the fact that mode-converted reflections are nonhyperbolic, even for horizontal reflectors in a constant-velocity medium, as in this case. This nonhyperbolic move-out, consequently, results in a stacking velocity that depends on the maximum offset under consideration.

This phenomenon is analogous to the “spreadlength bias” (stacking velocity being dependent on spread length) known for ordinary p-waves when the medium ve-

locity varies with depth (Hubral and Krey, 1980). But, for mode-converted waves, this dependence of stacking velocity on spreadlength is more severe and is observed even when the medium is homogeneous. Based on numerical tests, I have used the following time- and offset-independent empirical relation for estimating a percentage increase ($\% Inc$) above v_{nmo} to obtain stacking velocity that reasonably flattens events on CMP gathers:

$$\% Inc = 10 \frac{(1 - \gamma)^2}{\gamma}. \quad (3.10)$$

Although this relation was based on the assumption that the maximum offset is 4000 m, numerical tests show that the above $\% Inc$ should not be exceeded even when dealing with offsets larger than 4000 m; use of higher stacking velocity than that in equation (3.10) imposes excessive undercorrection on small-offset reflections, thus degrading the stack. Moreover, the above relation can be used for smaller offsets, since the smaller offsets are significantly less sensitive to the choice of NMO velocity. For example, although the velocity in Figure 3.1b is 5% higher than that in Figure 3.1a, both figures exhibit reflection times that are practically the same at offsets less than 1000 m.

The spreadlength bias for ordinary p-wave reflections in a vertically inhomogeneous medium is known to decrease with depth (or time). That is, reflections at later times in CMP gathers tend to more closely follow hyperbolic trajectories (Yilmaz, 1987). In contrast, the nonhyperbolic behavior, for the constant-velocity mode conversion here, persists even at later times (see reflections between 2.5 and 3.5 s from the deepest two reflectors in Figure 3.1). As with ordinary p-waves in media with depth-variable velocity, departure of moveouts from hyperbolas increases with offset for mode-converted waves, but now even in homogeneous media.

Before concluding this section, I should point out that relations (3.9) and (3.10)

are not intended for estimating NMO velocity for mode-converted data. In practice, one would typically obtain the NMO velocity from velocity analysis (t^2 - x^2 analysis, for example) on reflections from near-horizontal reflectors. However, relations (3.9) and (3.10) will be useful if, for example, one attempts to infer the velocity ratio from the NMO velocity so obtained, assuming the downgoing velocity v is known.

3.4 TZO for converted waves by Fourier transform

Following Hale (1984), but now dealing with mode-converted waves, I now derive an f - k TZO formulation based on the approximate moveout relation given by (2.16). Using equation (3.8) to replace t by t_n in equation (2.16), this latter equation yields a quadratic relation in zero-offset time t_0 as a function of NMO-corrected time t_n . We then obtain t_0 as

$$t_0 = \frac{2(\gamma - 1)h \sin \theta + \sqrt{t_n^2(1 + \gamma)^2 v_a^2 + 16\gamma h^2 \sin^2 \theta}}{(1 + \gamma)v_a}, \quad (3.11)$$

where it is assumed, again, that $p_0(t_0, y, h) = p_n(t_n, y, h)$. Notice the dependence of t_0 on the unknown quantity $\sin \theta/v_a$.

For a given half-offset h , the 2-D Fourier transform of the unknown $p_0(t_0, y, h)$ is, by definition,

$$P_0(\omega, k, h) = \int dt_0 e^{i\omega t_0} \int dy e^{-iky} p_0(t_0, y, h). \quad (3.12)$$

As with f - k TZO for ordinary p-waves, the integration over the unknown t_0 in the above transformation can be expressed in terms of the known NMO-corrected time, t_n , using the change of variables given by equation (3.11). Making use of the relations for the zero-offset slope ($\Delta t_0/\Delta y$) in the physical (time-distance) and Fourier (ω, k)

domains, i.e.,

$$\frac{\Delta t_0}{\Delta y} = \frac{2 \sin \theta}{v_a} = \frac{k}{\omega}, \quad (3.13)$$

it follows from (3.11) that

$$A \equiv \frac{dt_n}{dt_0} = \sqrt{1 + \frac{4\gamma h^2 k^2}{(1 + \gamma)^2 t_n^2 \omega^2}}, \quad (3.14)$$

and the transformation in (3.12) can then be written as

$$P_0(\omega, k, h) = \int dt_n A^{-1} e^{i\omega A t_n} e^{iBk} \int dy e^{-iky} p_n(t_n, y, h). \quad (3.15)$$

The quantity B , here, is a constant given by

$$B = \frac{\gamma - 1}{\gamma + 1} h. \quad (3.16)$$

The fact that B is a constant (for a constant offset $2h$) implies a linear spatial phase shift, i.e. e^{iBk} , in the Fourier domain. This linear phase shift, in turn, corresponds to a constant lateral shift in the space domain. Specifically, this constant shift is the asymptotic approximation (offset small compared with depth) for the spatial location of the conversion point for a horizontal reflector (Sword, 1984).

Finally, 2-D inverse transformation of equation (3.15) yields the desired TZO data, i.e., $p_0(t_0, y, h)$, as follows

$$p_0(t_0, y, h) = \frac{1}{(2\pi)^2} \int d\omega e^{-i\omega t_0} \int dk e^{iky} P_0(\omega, k, h).$$

3.5 The impulse response

The corresponding TZO operator in the t - y domain is obtained by finding the inverse Fourier transform of $P_0(\omega, k, h)$ when $p_n(t_n, y, h)$ is an impulse. This is accomplished by applying the method of stationary phase to equation (3.15) (see, for example, Bleistein, 1984; and Liner, 1988). The TZO operator in the t - y domain is found to be an ellipse (Appendix C), given by

$$\left(\frac{t_0}{t_n}\right)^2 + \left(\frac{Y_0}{H}\right)^2 = 1. \quad (3.17)$$

The quantity H is a scaled version of half-offset h , given by

$$H = \frac{2\sqrt{\gamma}}{1 + \gamma} h. \quad (3.18)$$

Equation (3.18) implies that the TZO impulse response for mode-converted waves is a *squeezed* version of that given by equation (3.5) for ordinary p-waves. The quantity Y_0 is the location of the output zero-offset trace; it is shifted from the output location for ordinary p-waves, y_0 , and is given by

$$Y_0 = y_0 - \frac{1 - \gamma}{1 + \gamma} h. \quad (3.19)$$

When $\gamma = 1$ (no mode conversion), equation (3.17) reduces, again, to the well-known DMO ellipse for ordinary p-waves as given by equation (3.5).

The offset scaling as implied by (3.18), and the shift in the output zero-offset trace as suggested by (3.19), are equivalent to the transformation introduced by Sword (1984). Sword suggested that each prestack seismic trace, in the time-space domain, be given a new midpoint location and a new offset, consistent with equations (3.18)

and (3.19), prior to any processing. The TZO approach introduced here, on the other hand, accounts for the location of the new midpoints, as suggested by Sword, without having to deal with trace interpolation in the time-space domain; each trace is simply shifted to the desired location by introducing a spatial phase shift in the f - k domain, as suggested by the transform in equation (3.15).

The formulation of this TZO approach was based on a truncated version of the series in equation (2.15). Considering only the first three terms of the series, as was done in the derivation above, results in a quadratic equation in t_0 , as a function of t_n , the solution of which is not difficult to find and is given in equation (3.11). If higher-order terms of the series are also considered, the resultant equation in t_0 becomes cubic or higher order. Solutions to the cubic and higher-order equations are too lengthy for our purposes and are, therefore, deemed impractical to implement. Alternatively, the errors arising from truncating the power series can be alleviated by modifying the derived f - k TZO operator.

One result of the truncation of the power series was that the phase shift obtained in (3.15) was constant and time-invariant. The actual spatial shift of the conversion point for a horizontal reflector, however, is known to vary with reflection depth, or time (Tessmer and Behle, 1988). Figure (3.2) shows the theoretical impulse response (solid), along with the derived, approximate impulse response assuming four input impulses. The lateral shifts of the apexes of the theoretical operators are clearly time-variant; the apexes correspond to horizontal reflections, i.e., zero dip. From the figure, it is also clear that the lateral, constant shift of the derived TZO operator needs to be adjusted (increased in this case), in a time-varying manner, so as to obtain a better match of the two operators near the vicinity of their apexes.

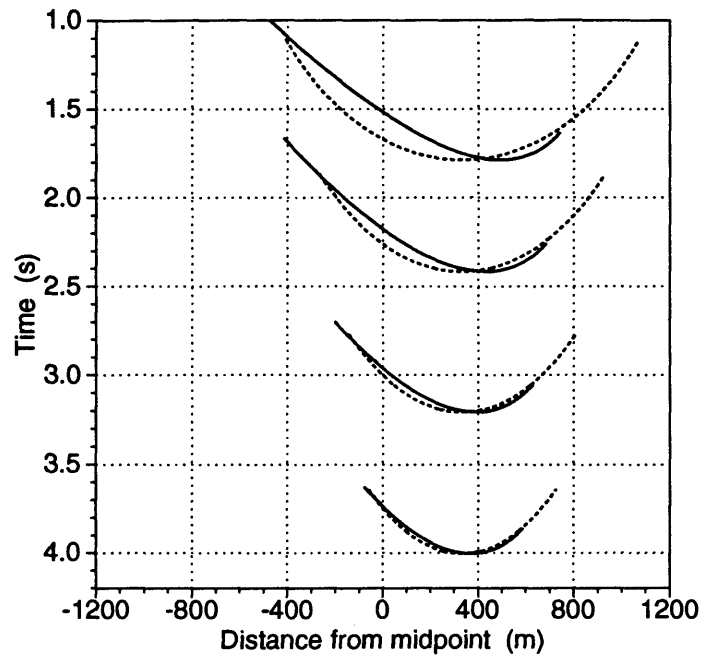


FIG. 3.2. Theoretical (solid) and approximate (dotted) TZO impulse responses for four input impulses (1.75, 2.4, 3.2, and 4.0 s) at midpoint 0. The approximate operator has a constant (time-invariant) lateral shift, as opposed to the time-variant shift for the theoretical TZO operator. The offset is 2000 m. The downgoing and upgoing velocities are 2000 and 1000 m/s, respectively.

3.6 Improving the TZO operator

In this section, we attempt to improve the derived, approximate TZO operator in two different ways. First, the constant, spatial shift of the operator will be modified to better resemble the behavior of the conversion point for a horizontal reflector. This modification is achieved by altering the phase of the TZO transform to be time variant. Second, a squeeze/stretch technique is applied to the operator to make it better match the theoretical one.

3.6.1 Time-variant phase shift

It is easy to embed time-variance of the conversion point into the phase-shift term of the transform in (3.15), and thus partially alleviate errors arising from truncating the series given in (2.15). Let us again call the lateral position of the conversion point, relative to the midpoint, b . With D denoting the depth of a horizontal reflector, the relationship between D and b (Appendix D) is given by

$$D^2 = -\frac{(h^2 - b^2)^2}{h^2 + 2\alpha hb/\beta + b^2}, \quad (3.20)$$

where we recall from equation (2.3) that α and β are constants depending only on the velocity ratio γ . In terms of normalized quantities $\tilde{D} = D/h$ and $\tilde{b} = b/h$, equation (3.20) can be written as

$$\tilde{D}^2 = -\frac{(1 - \tilde{b}^2)^2}{1 + 2\alpha\tilde{b}/\beta + \tilde{b}^2}, \quad (3.21)$$

showing that the relation between \tilde{D} and \tilde{b} is totally determined if the velocity ratio γ is known. Naturally, we would prefer to find b as a function of D using equation (3.20); this, however, requires solving a quartic equation in b . Rather, we directly calculate \tilde{D} as a function of \tilde{b} using equation (3.21), thus building a table of $[\tilde{D}, \tilde{b}(\tilde{D})]$ pairs for any given velocity ratio. Making use of a table constructed in this way aids the efficiency of the TZO process since such a table needs to be calculated only once (the only required parameter is the velocity ratio). Figure 3.3 shows an example of normalized b as a function of normalized depth for different velocity ratios. In the TZO process itself, both \tilde{D} and \tilde{b} are translated, respectively, into NMO-corrected time t_n and actual lateral shift b , using velocity and half-offset information. In other words, the pairs $[\tilde{D}, \tilde{b}(\tilde{D})]$ in the original table are trivially converted into pairs $[t_n, b(t_n)]$. Then,

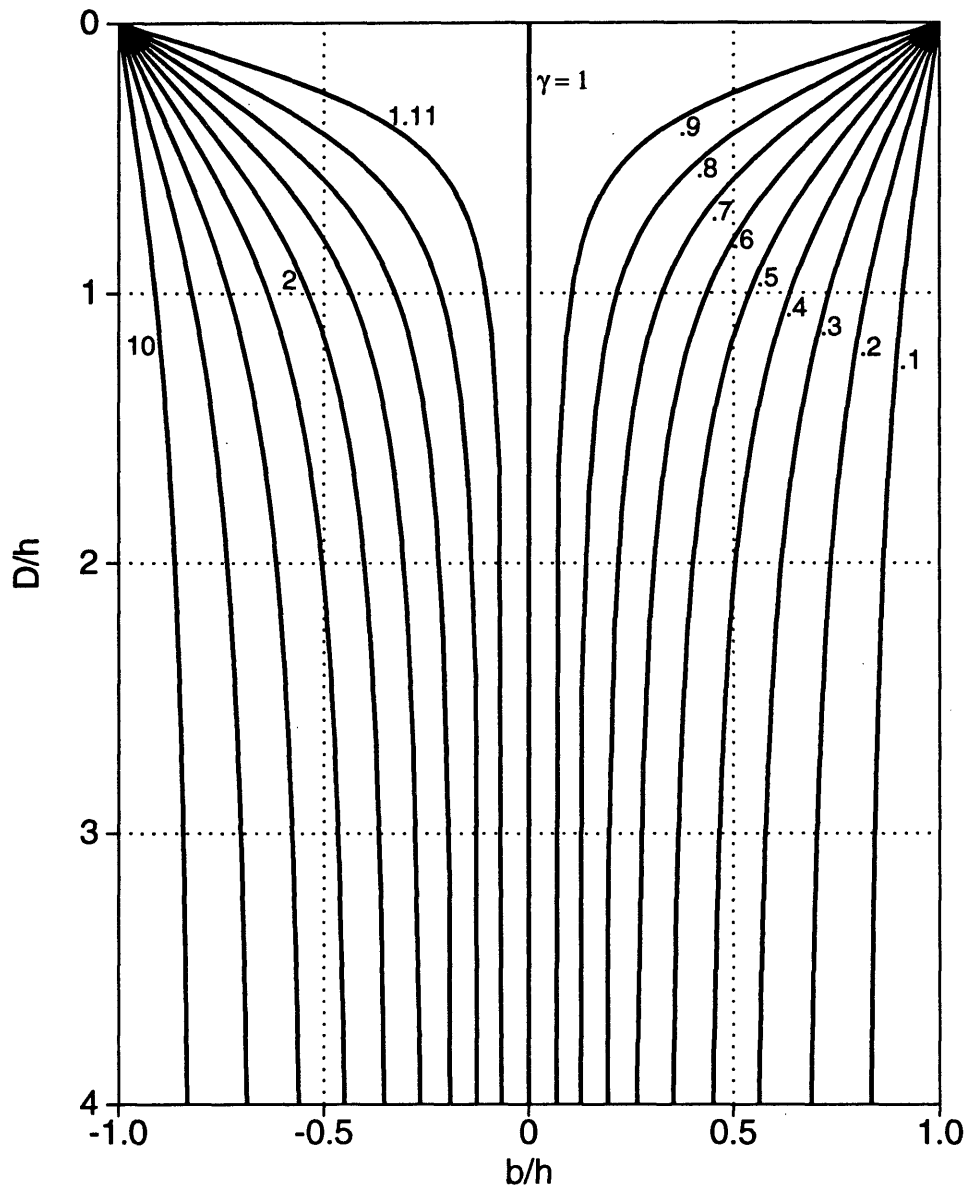


FIG. 3.3. Behavior of the conversion point in a homogeneous medium, as dictated by equation (3.21). Here, for different velocity ratios, normalized depth (D/h) of the conversion point is plotted against the normalized, lateral position (b/h) for a horizontal reflector. The numbers shown on the plots are values of γ . Note that plots for γ and $1/\gamma$ are symmetric about the vertical line $b/h = 0$.

we use this time-variant $b(t_n)$ in the phase shift of the transform given by (3.15), instead of the time-invariant B given by equation (3.16). Figure 3.4 shows impulses and TZO impulse responses for TZO constructed in this way.

Figure 3.4a shows ten impulses on a common-offset ($2h = 5000$ m) section. Assuming a p-sv mode conversion with velocity ratio $\gamma = 0.5$, the response of the

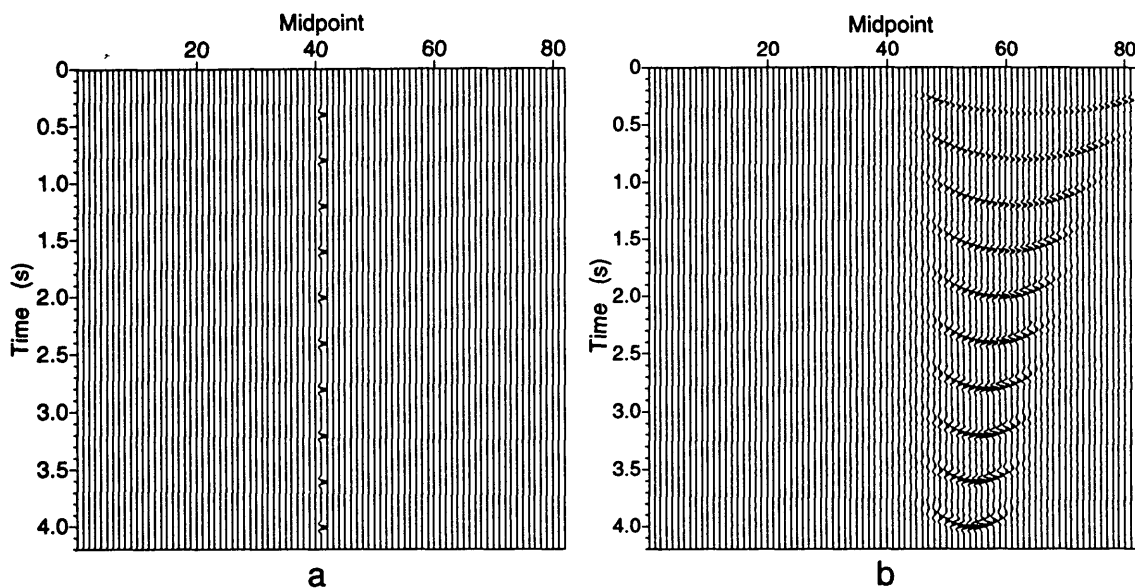


FIG. 3.4. Ten impulses in a constant-offset section (a) used to test the response of the TZO operator for mode-converted waves (b). The offset here, 5000 m, is chosen large to emphasize the time-variant lateral shifts seen in the impulse responses in (b). The midpoint spacing is 100 m.

modified TZO operator to those impulses is as shown in Figure 3.4b. Each impulse response is an ellipse that has now been squeezed, relative to that for ordinary p-waves, in the sense that its horizontal axis, when extended to the surface, spans a distance $2H$ (see equation [3.18]) that is smaller than offset $2h$. Furthermore, each squeezed ellipse has been laterally shifted, in a time-varying manner, in such a way

that the apex now corresponds to the conversion point for a horizontal reflector.

3.6.2 Squeezing and stretching the TZO operator

While proper, time-variant shift has been introduced, the elliptical shape of the TZO operator, as Figure 3.2 clearly shows, is still wrong. Squeezing (or stretching) the operator is a practical way to modifying its response to a nonelliptical shape that is closer to the correct one. Hale and Artley (1991) introduced a *squeeze factor* that would squeeze the elliptical DMO response for ordinary p-waves. Although their squeeze factor was used primarily to tune the elliptical DMO response to better handle steep reflections for depth-variable velocity, the same squeeze concept may also be used even when velocity is constant. Specifically, Hale and Artley have empirically found that a squeeze factor of 0.62 is sufficient to improve the accuracy of constant-velocity DMO if the Fourier-transform approximation introduced by Nottfors and Godfrey (1987) is used. I find that this squeeze concept is also beneficial in improving the $f-k$ TZO process for mode-converted waves. I adopt Hale and Artley's squeeze idea here to distort the shape of the approximate, mode-converted TZO operator. As we will see, TZO based on the resulting shape, which is closer to the correct one than that without distortion, yields better alignment of reflections in CRP gathers.

Figure 3.5a shows the shapes of four impulse responses of TZO (dashed), where only proper, time-variant lateral shifts have been applied. For comparison, the correct responses (solid) are also shown in the figure. Negative zero-offset slopes correspond to the right segments of each curve, whereas positive zero-offset slopes correspond to the left segments. As Figure 3.5a suggests, to achieve a response that is closer to the correct one, negative slopes need to be squeezed, and positive slopes need to

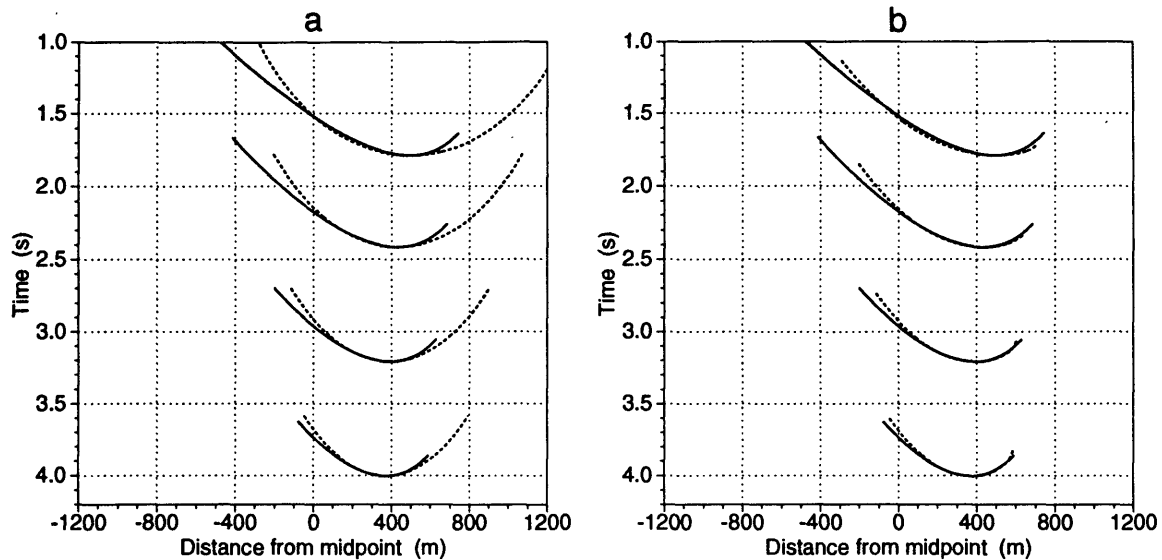


FIG. 3.5. Shapes of approximate TZO response (dashed) to four impulses, along with those of the correct responses (solid lines). Proper, time-variant lateral shifts have been applied in (a). The result in (a) after squeezing/stretching is shown in (b); the squeeze and stretch factors are, respectively, 0.05 and 5.0. A p–sv mode conversion ($\gamma = 0.5$) is assumed here. Offset is 2000 m. Input impulses are the same as those for Figure 3.2.

be stretched. In other words, for the p–sv mode conversion shown in Figure 3.5a, the *sign* of the slope, alone, determines whether stretching or squeezing should be applied. Figure 3.5b exhibits a squeezed/stretched version of the responses shown in Figure 3.5a. Figure 3.6 shows the response of an actual TZO algorithm without and with stretching/squeezing applied, for six input impulses.

The empirical process of squeezing or stretching would have little practical value if it were dependent on either dip or time. Moreover, the stretch and squeeze factors must not depend too sensitively on γ . Although the stretched/squeezed curves could be made to fit the correct ones if the stretch/squeeze factors were allowed to vary with time and dip, I choose stretch and squeeze factors here that depend only on the velocity ratio, γ , and yield Hale and Artley's squeeze factor when $\gamma = 1$. Because

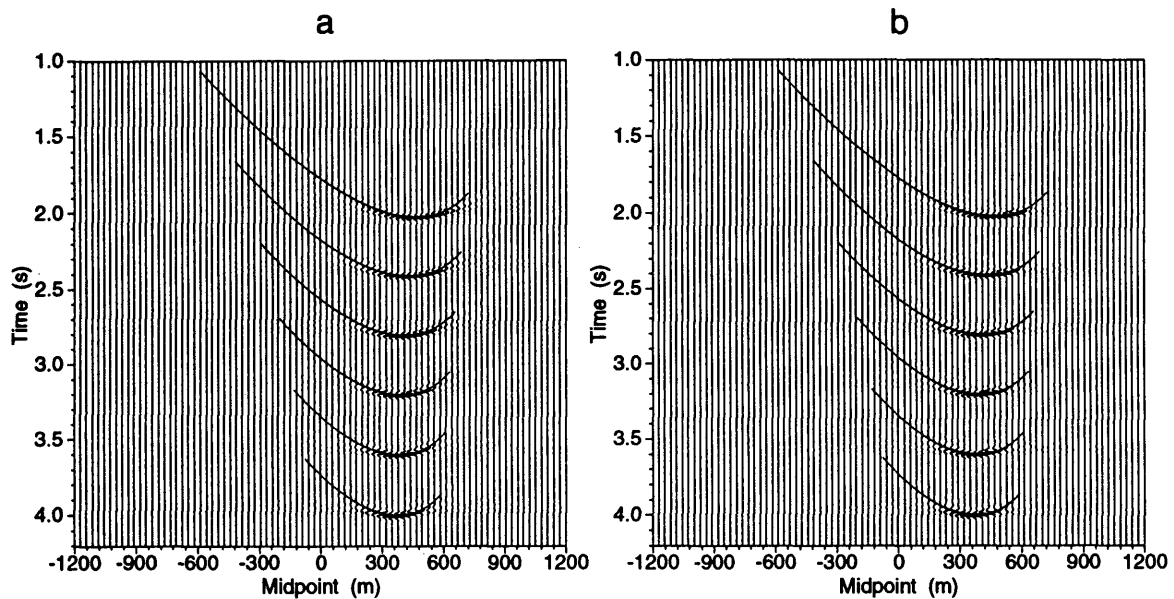


FIG. 3.6. Response of a TZO algorithm to six impulses, along with the correct responses (solid lines). (a) No squeezing/stretching, (b) Stretch and squeeze factors of 5.0 and 0.05, respectively, have been applied. The responses in (b) are closer to the correct shapes. A p–sv mode conversion ($\gamma = 0.5$) is assumed here. Offset is 2000 m. Input impulses were originally at midpoint 0.

the stretch/squeeze factors here depend on the velocity ratio only, the match between a stretched/squeezed curve and its theoretical counterpart is imperfect, but, as we shall see, yields quite acceptable moveout correction. The TZO operator is thus either squeezed or stretched, depending on the sign of the zero-offset slope as well as on the mode of conversion (p–sv or sv–p). I empirically determine this factor by comparing squeezed/stretched TZO impulse responses, using different velocity ratios, to correct impulses given by equation (2.11).

For convenience, let us define $S1$ as a parameter that achieves either squeezing or stretching and apply it to the *positive* zero-offset slopes, i.e. the left segment of the TZO operator, regardless of the mode of conversion (p–sv or sv–p). By the

same token, we define $S2$ as a parameter differing from $S1$ in that (1) $S2$ is always associated with the *negative* zero-offset slopes, and (2) $S2$ performs the opposite action of $S1$ (e.g., if the action of $S1$ is squeezing, then that of $S2$ is stretching). With this convention, and assuming p–sv mode conversion, the stretch and squeeze factors, $S1$ and $S2$, respectively, may be approximated using the following relations

$$\begin{aligned} S1 &= 0.620 + 0.633 \left[\left(\frac{1}{\gamma} \right)^3 - 1 \right], \\ S2 &= 0.620 + 0.615 \left[\left(\frac{1}{2 - \gamma} \right)^7 - 1 \right], \end{aligned} \quad (3.22)$$

which were empirically determined using a least-square fit on experimental data. Figure 3.7 shows plots of $S1$ and $S2$ calculated from the above relations, along with the experimentally determined factors, as a function of γ , assuming p–sv mode conversion. For sv–p mode conversion, the empirical squeeze and stretch factors, $S1$ and $S2$, respectively, are given by

$$\begin{aligned} S1 &= 0.620 + 0.615 \left[\left(\frac{1}{2 - 1/\gamma} \right)^7 - 1 \right], \\ S2 &= 0.620 + 0.633(\gamma^3 - 1). \end{aligned} \quad (3.23)$$

In general, any of these four expressions achieves squeezing when its value is less than 1, stretching if the value exceeds 1, and does nothing to the TZO operator when it is equal to 1.

Neither relation for $S1$ and $S2$, however, yields a value of unity when the velocity ratio is 1; they both give a value of 0.62 which implies squeezing of both positive and negative slopes. As shown by Liner (1990), the Fourier-transform approximation (Notfors and Godfrey, 1987), which we assume is used here, results in a stretched

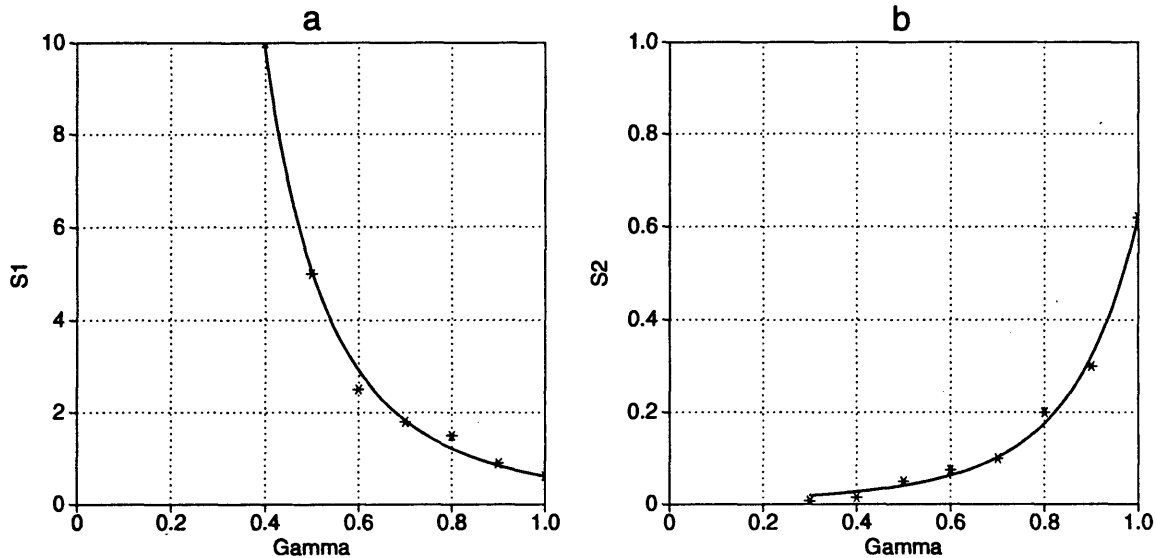


FIG. 3.7. Stretch factor S_1 (a) and squeeze factor S_2 (b) as a function of the velocity ratio γ for p-sv mode conversion. S_1 here stretches positive zero-offset slopes, whereas S_2 squeezes negative ones. For sv-p mode conversion, factors S_1 and S_2 are given by equation (3.23). Asterisks in the plots indicate experimental data.

impulse response that is wider than the theoretical constant-velocity DMO ellipse. The squeeze factor 0.62 compensates for this stretching (Hale and Artley, 1991).

3.7 Full-offset TZO

Recall, this analysis for mode-converted waves has been based on a truncated moveout relation, equation (2.16). The f - k TZO formulation, which was based on the approximate moveout relation, suggested that the half-offset h be scaled, in accordance with equation (3.18), before TZO implementation. In fact, the TZO results shown so far honored this offset-scaling result. Let us refer to TZO constructed in this way as *scaled-offset* TZO. Alternatively, we could simply have applied squeezing and stretching factors directly within Hale's f - k TZO approach, which ignores mode conversion. I will call that approach *full-offset* TZO, and shall investigate it next.

As with scaled-offset TZO, full-offset TZO, here, also honors time-variant lateral shifts of the impulse responses and makes use of approximate squeeze/stretch factors. That is, full-offset TZO differs from scaled-offset TZO only in that it ignores the offset scaling given by equation (3.18). Figure 3.8 shows the same data as in Figure 3.5 but

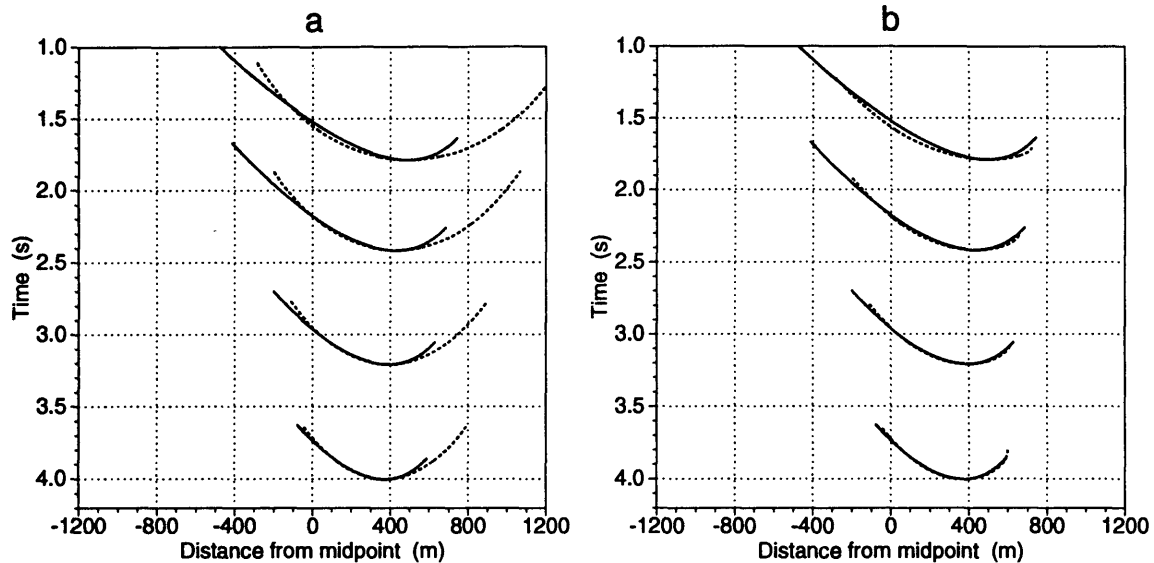


FIG. 3.8. Impulse-response shapes of full-offset, approximate TZO operator (dashed) to same input data as in Figure 3.5 before (a) and after (b) applying squeeze/stretch (0.04/3.0) compensation. Solid lines indicate theoretical impulse responses. Down-going and upgoing velocities of 2000 and 1000 m/s, respectively, are assumed. Offset is 2000 m.

now assuming full-offset (no offset scaling). Since offset (and hence the lateral extent of the elliptical impulse response) is now wider than that in the scaled-offset case, both the squeeze and stretch factors required here will be smaller. Squeeze/stretch factors of 0.04/3.0 are used for the full-offset TZO in Figure 3.8b, as opposed to 0.05/5.0 for the scaled-offset TZO in Figure 3.5b.

Comparison of Figures 3.5b and 3.8b shows that the major difference between the two methods is in their treatments of positive zero-offset slopes (left segments of

their impulse-response curves). While the full-offset case yields a shape that is closer to the correct one for large dips (far from the apex), the scaled-offset case gives a better fit for moderate dips (near the apex). Thus, full-offset TZO better handles large dips at the expense of further undercorrecting moderate dips.

This is also evident in Figure 3.9, which compares CRP gathers based on the two methods, for p-sv synthetic data assuming a downgoing velocity of 2000 m/s and

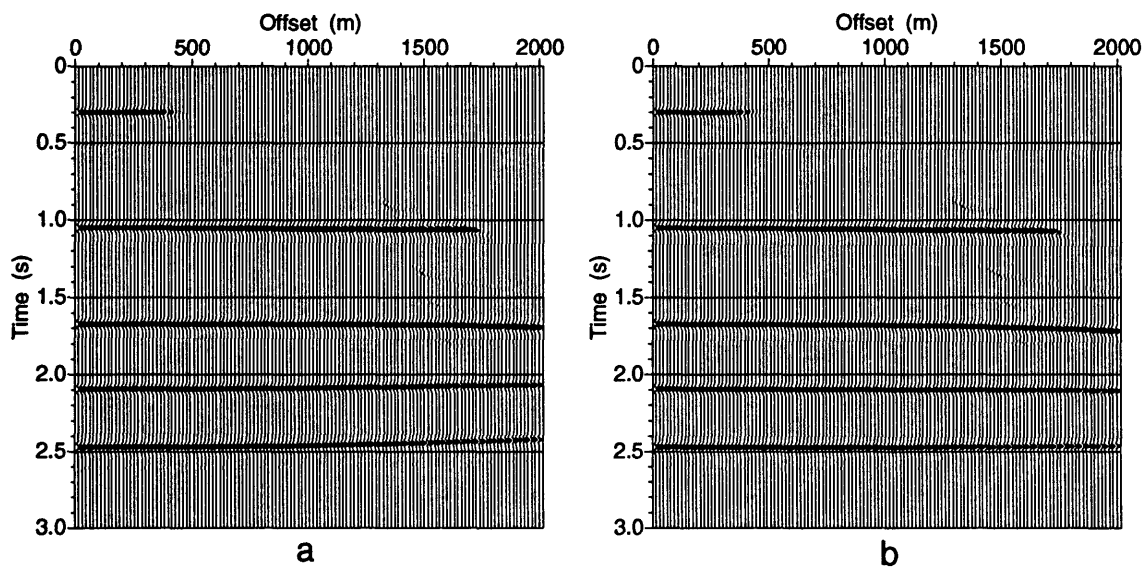


FIG. 3.9. CRP gathers obtained by applying scaled-offset TZO (a) and full-offset TZO (b). Reflections here are from five reflectors with dips ranging from 0 (shallowest) to 80 degrees, in increments of 20 degrees. A downgoing velocity of 2000 m/s, and a velocity ratio 0.5 are assumed.

a velocity ratio of 0.5. The data consist of reflections from five reflectors, with dips ranging from 0 to 80 degrees in increments of 20 degrees. The signs of the dips in this example are such that the resulting zero-offset slopes are positive. The velocity used in the NMO correction is 1485 m/s (Section 3.3). In the TZO implementation, squeeze/stretch factors of 0.05/5.0 and 0.04/3.0 have been applied to the data in Figures 3.9a and 3.9b, respectively. While full-offset TZO better corrects reflections from

steep reflectors (see the deepest reflector in Figure 3.9b, which dips at 80 degrees), reflections from the moderately dipping reflectors (near 1.0 and 1.7 s, respectively) are more undercorrected than those from scaled-offset TZO (Figure 3.9a).

One would naturally prefer to use a TZO operator that gives reasonable results for all dips; unfortunately, a compromise is required here between moderate and steep dips in the positive-slope segment of the TZO operator for mode-converted waves. In general, however, one should account for both negative and positive zero-offset slopes in seismic data to accommodate, for example, conflicting dips. Although the examples shown here are such that they all pertain to end-on seismic shooting, for split-spread shooting the TZO approach described here still holds, but care must be taken by accounting for the polarity reversal of amplitude. That is, for split-spread geometry the polarities on the two sides of the spread of recorded, mode-converted seismograms are known to be opposite to one another (see DeSanto [1986] for a thorough discussion of displacements associated with mode-converted waves). One solution to this problem is to simply reverse the amplitude polarity of one side of the spread before any processing. Another solution is to process each side of the spread separately, and then reverse the polarity of one side of the spread before stack.

Figure 3.10 shows the same data as in Figure 3.9 but now with signs of dips reversed. That is, the sv-leg of the reflection path is updip of the p-leg. Squeeze/stretch factors here are the same as in Figure 3.9. In this case, both scaled-offset TZO (Figure 3.10a) and full-offset TZO (Figure 3.10b) yield similar, and quite good, results. Based on observation of results from the previous two examples, scaled-offset TZO seems favorable over full-offset TZO when reflectors have moderate dips. Scaled-offset TZO reduces the undercorrection seen on reflections from moderately dipping reflectors. When steeply dipping reflectors are known to be present, however, full-offset

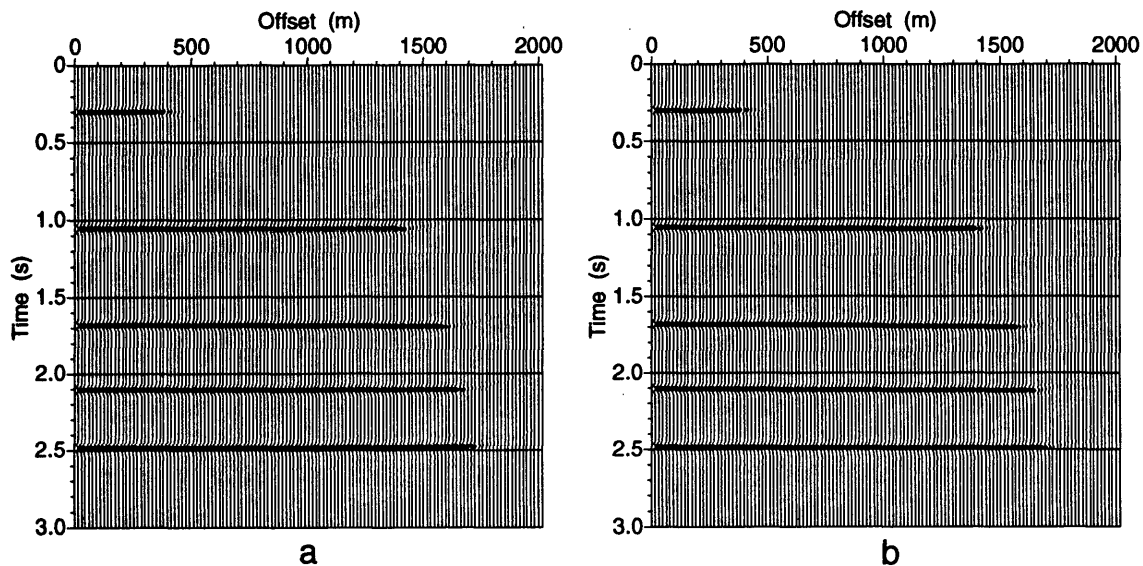


FIG. 3.10. CRP gathers obtained by applying scaled-offset TZO (a) and full-offset TZO (b). Reflections here are from the same five reflectors in Figure 3.9 but with dips reversed in sign.

TZO is favorable as it better handles large dips than does scaled-offset TZO. Since the values and orientation of dips are generally unknown, either TZO method (scaled- or full-offset) may be used since both approaches yield flattening of events that is far superior to that when mode conversion is ignored in TZO. Based on numerical tests, the stretch/squeeze factors S_1 and S_2 given by equations (3.22) and (3.23) for scaled-offset TZO must be scaled by a factor of 0.65 if full-offset TZO is used. I shall refer to both scaled- and full-offset TZO as the *mode-converted TZO method* and use them both for the remainder of this thesis; the method used, be it scaled- or full-offset, will be clearly indicated for each problem under consideration.

Chapter 4

APPLICATION TO SYNTHETIC DATA

4.1 Introduction

In this chapter, we start by applying the mode-converted TZO method to synthetic, mode-converted seismic data, assuming a homogeneous medium. We then examine the situation when velocity varies with depth, showing that the mode-converted TZO method can be tailored to deal with reflections in vertically inhomogeneous media. Again, we use synthetic data to assess the reliability of tailored TZO for depth-variable velocity.

Finally, we study the sensitivity of the mode-converted TZO method to the choice of the velocity ratio γ , for both homogeneous and inhomogeneous media. As we will see, the mode-converted TZO method introduced here is insensitive to the choice of γ for horizontal reflections (assuming a proper NMO velocity is used), quite sensitive to γ for moderately dipping reflections, and highly sensitive when dips are large.

4.2 Constant velocity

Recall, the formulation developed here for mode-converted TZO is based on the assumption that the medium is homogeneous (constant velocity). We now test the proposed TZO method on synthetic, mode-converted seismic data, assuming a constant downgoing velocity of 2000 m/s and a velocity ratio $\gamma = 0.5$, thus implying p–sv mode conversion.

As discussed in Chapter 2, the traveltime for mode-converted waves depends not only on dip, but also on the sign of dip. To see how TZO treats reflections from reflectors with arbitrary dip, we will consider two depth models that differ only in that their reflectors have opposite dip orientations. That is, the two depth models are mirror images of each other. Figure 4.1 shows the zero-offset sections associated with

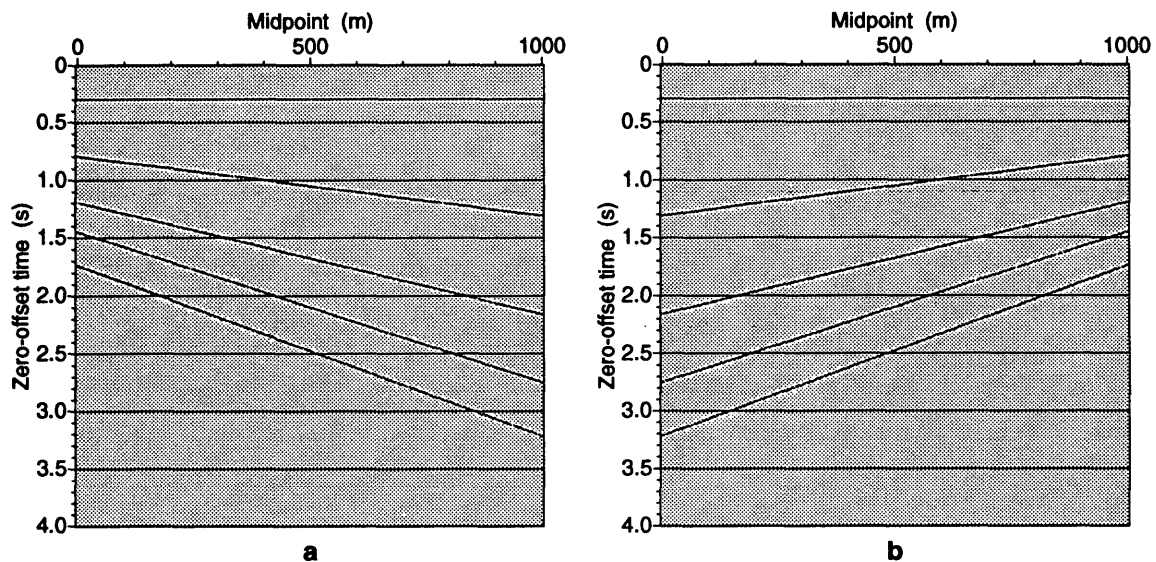


FIG. 4.1. Zero-offset data for the two test models used to generate synthetic p-sv data. Each figure shows zero-offset reflections from five reflectors in a homogeneous medium. The downgoing velocity is 2000 m/s, and γ is 0.5. For each model, the shallowest reflector is horizontal, the deepest reflector dips at 80 degrees, and the dip increment is 20 degrees. Since reflectors in both models have opposite dip orientations, we shall refer to models (a) and (b) as the positive- and negative-dip models, respectively.

each model. Each depth model consists of five reflectors in a homogeneous medium, with reflector dips ranging from horizontal (shallowest) to 80 degrees (deepest); dip increment is 20 degrees. Since the two models are symmetric, the two middle midpoints, at 500 m, in both zero-offset models have the same zero-offset time. We will use these midpoints as test points at which to compare uncorrected CMP gathers,

NMO-corrected CMP gathers, and CRP gathers.

Synthetic p-sv seismic data are generated by ray tracing, assuming the source is situated to the left of receivers (i.e., at lower midpoint locations) for both models. For convenience, I will refer to Figures 4.1a and 4.1b as positive- and negative-dip models, respectively. For each model, 126 CMP gathers are generated, each with 125 traces. The distance separating two adjacent CMP gathers is 8 m. Within each CMP gather, the trace spacing, and also the offset of the nearest trace, is 16 m; the maximum offset is 2000 m. A zero-phase (symmetric) wavelet is assumed, with a dominant frequency of 25 Hz. The time sampling interval is 4 ms.

The CMP gathers corresponding to the test points of both models are shown in Figure 4.2. The two models have the same moveout only for reflections from the

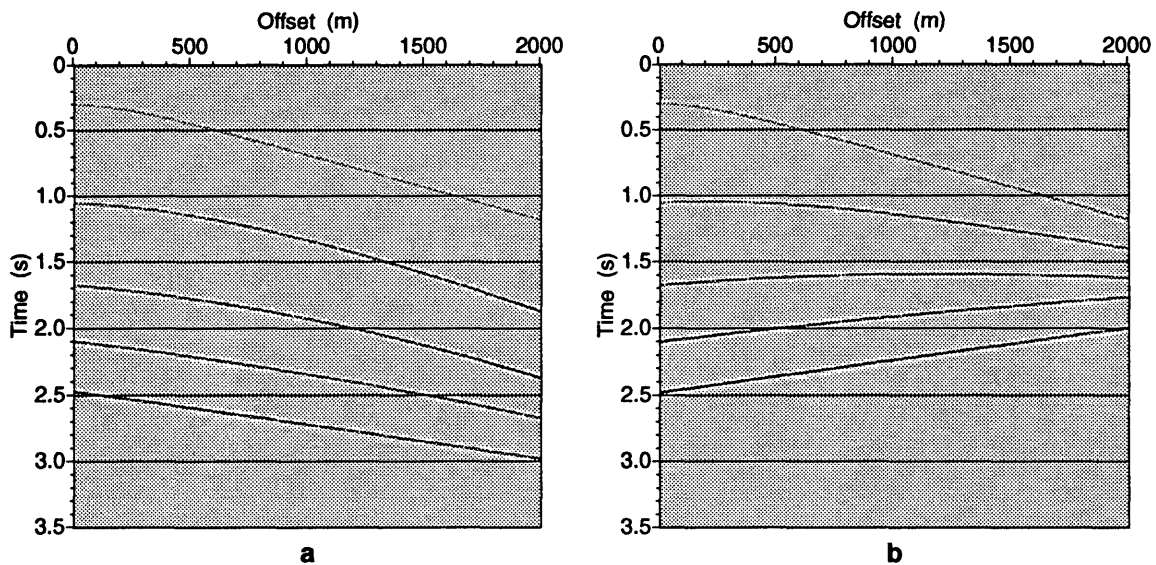


FIG. 4.2. Synthetic p-sv CMP gathers. (a) and (b) correspond to the middle midpoints of Figures 4.1a and 4.1b, respectively. The downgoing velocity is 2000 m/s, and the velocity ratio is 0.5.

horizontal (shallowest) reflectors. The nonhyperbolic moveout is obvious, especially

on reflections from steep reflectors. The two CMP gathers exhibited in Figure 4.2a and 4.2b would have had the same (hyperbolic) moveouts if the velocity ratio had been unity (no mode conversion). Moreover, reflections from the dipping reflectors in the negative-dip model, Figure 4.2b, exhibit reverse (i.e., negative) moveout. Such reverse moveout (i.e., energy arriving earlier on the far offsets than on the near) is familiar for p-waves in areas of complex overburden, but here the medium is homogeneous. Also, unlike the situation for ordinary p-wave reflections in CMP gathers, apexes of the moveout curves here are not situated at zero offset. For example, see the second moveout curve (near 1 s) in Figure 4.2b, which has its apex beneath offset ≈ 300 m; the middle reflector (near 1.7 s) has its apex at offset ≈ 1300 m.

For these two models, the NMO velocity that would reasonably flatten reflections from horizontal reflectors is 1485 m/s (see Section 3.3). Using this NMO velocity, the NMO-corrected gathers corresponding to Figure 4.2 are shown in Figure 4.3. In these gathers, truncation of reflections on far offsets and earlier times is due to stretch muting, typical in NMO-corrected gathers. For both models, reflections from the horizontal reflectors (shallowest) are properly aligned after NMO correction. For dipping reflectors, however, the positive-dip model (Figure 4.3a) shows moveouts that differ from those familiar in NMO-corrected ordinary p-wave data. Ordinarily, moveout of reflections becomes *overcorrected* after such NMO correction. Here, after NMO correction the moveout is undercorrected, and in a peculiar manner; it is concave upward or downward, depending on the magnitude of the dip. On the other hand, the moveouts in the negative-dip model exhibited in Figure 4.3b are now severely overcorrected relative to the ordinary p-wave case. Furthermore, the overcorrected moveouts here do not follow the elliptical trajectories familiar in overcorrected, p-wave data.

Before applying the mode-converted TZO method to the data, let us first in-

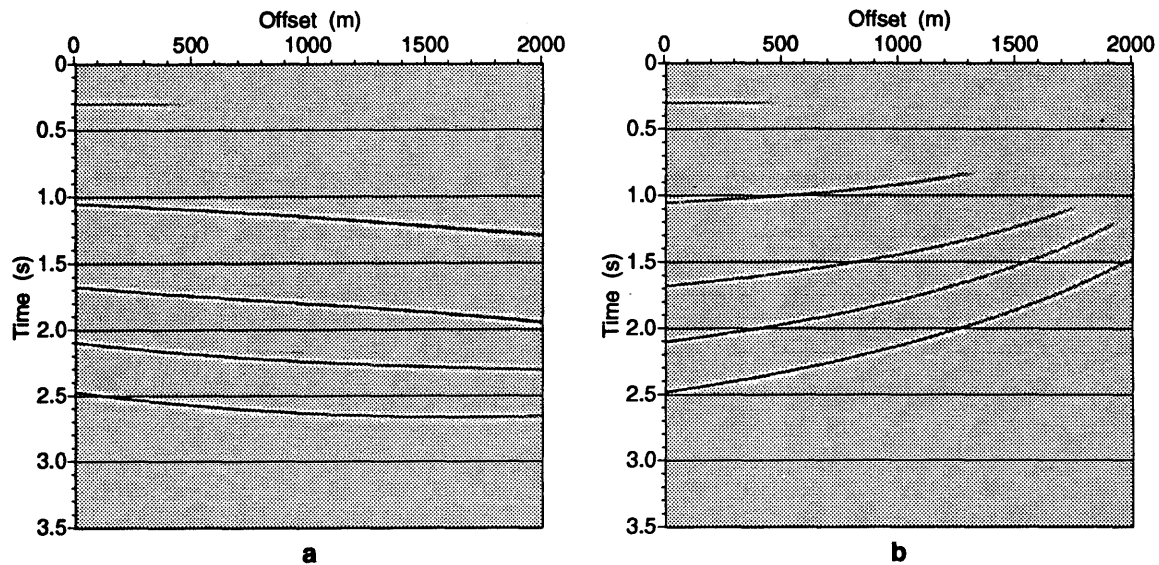


FIG. 4.3. NMO-corrected gathers corresponding to the CMP gathers shown in Figure 4.2. The NMO velocity used is 1485 m/s.

investigate the situation when the mode-converted data are TZO-processed using a conventional method that ignores mode conversion (i.e., $\gamma = 1$ is assumed in the processing). The NMO-corrected data were TZO-processed using Hale's $f-k$ TZO method, which does not honor mode conversion. Figure 4.4 shows the resulting (erroneous) CRP gathers that correspond to the CMP gathers of Figure 4.2. It is clear from both models in Figure 4.4 that only reflections from the horizontal reflector are properly corrected (horizontally aligned). Notice, also, that reflections from the dipping reflectors are either undercorrected or overcorrected, depending on the sign of dip; reflections in the positive-dip model show undercorrection, whereas those in the model of opposite dips reveal overcorrection. Moreover, the misalignment of the positive-dip data is actually *made worse* by the conventional DMO processing.

CRP gathers processed erroneously in this way produce unacceptable stacks, as the CRP stacks in Figure 4.5 clearly show. For both models, reflections from

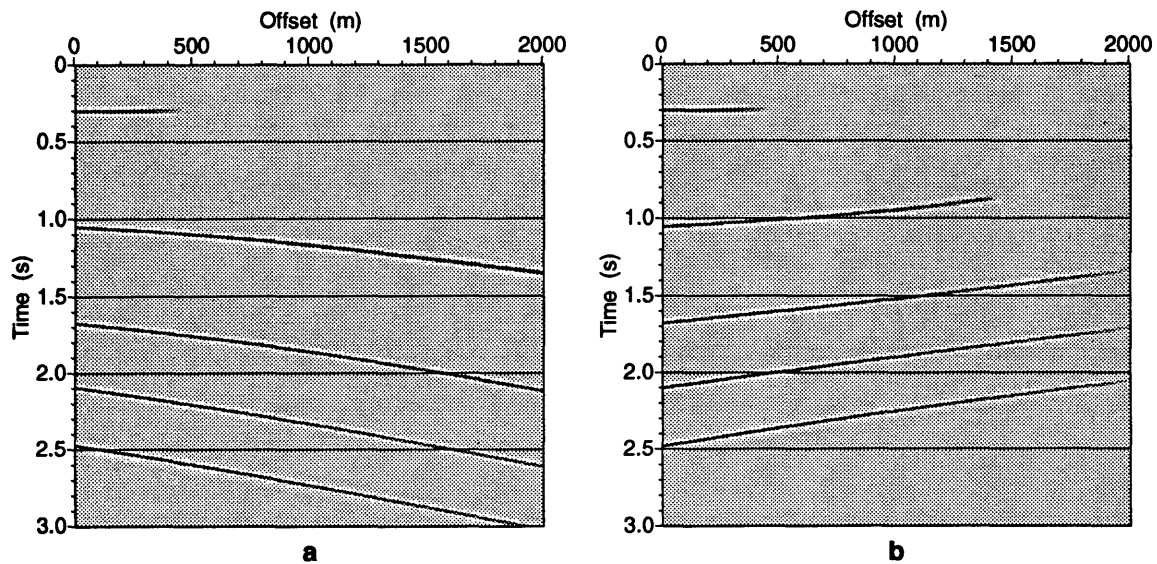


FIG. 4.4. Erroneous CRP gathers obtained by processing the mode-converted data with a conventional TZO algorithm that ignores mode conversion. Only horizontal reflections (shallowest) are properly aligned.

only the horizontal reflectors stack properly; in the stack, reflections from dipping reflectors are almost completely wiped out. These examples clearly illustrate that mode-converted seismic data *should never be processed* with a TZO algorithm that ignores mode conversion.

We now process the NMO-corrected data from both models using the mode-converted TZO method, thus honoring mode conversion. In implementing TZO here, I choose a velocity ratio γ of 0.5, the same as that used in generating the synthetic data. Sensitivity of TZO to the choice of erroneous velocity ratios will be discussed later in this chapter.

Figure 4.6 shows TZO-corrected gathers corresponding to the NMO-corrected gathers of Figure 4.3. The positive-dip model, Figure 4.6a, was processed by applying full-offset TZO; the result would have been slightly different (better or worse,

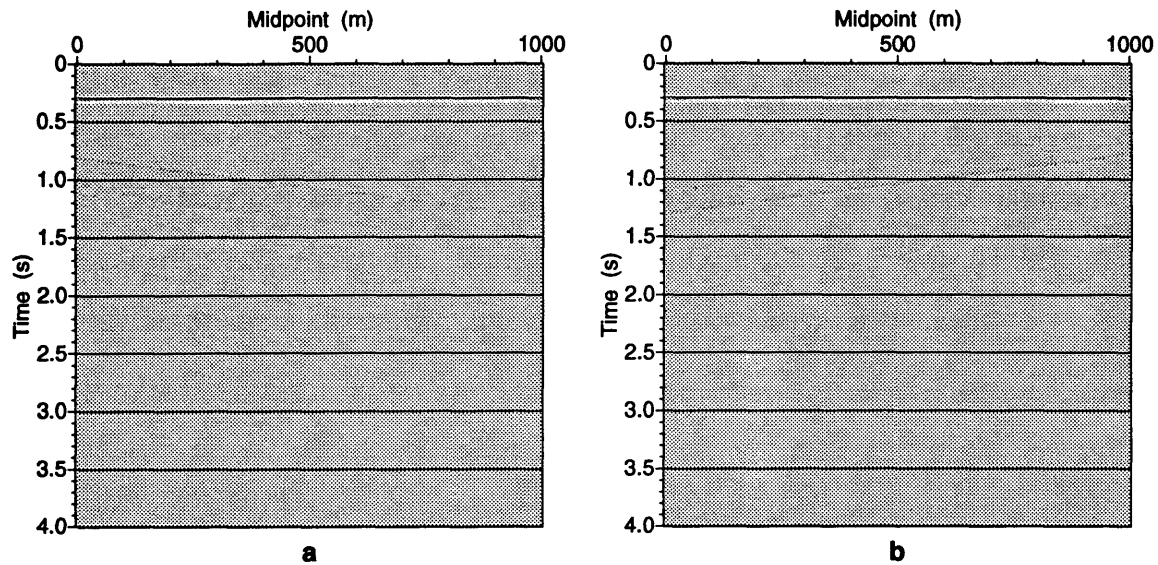


FIG. 4.5. Stacks of erroneous CRP gathers processed by ignoring mode conversion. For both the positive- and negative-dip models, (a) and (b), respectively, reflections from only horizontal reflectors (shallowest) stack properly.

depending on dip, Section 3.7) if, instead, scaled-offset TZO had been applied. The negative-dip model, Figure 4.6b, was processed assuming scaled-offset TZO (full-offset TZO would have produced similar results).

As Figure 4.6 shows, for both models the mode-converted TZO method is successful, to a great extent, in correcting (i.e., horizontally aligning) reflections, including those from the reflectors that dip at 80 degrees. Recall, the TZO method that ignored mode conversion (Figure 4.4) resulted in either undercorrection or overcorrection of reflections, depending on the sign of dip. On the other hand, the TZO method here, which honors mode conversion, corrects data regardless of the sign of dip. Hence, the TZO method proposed here is far superior to that implemented by ignoring mode conversion in TZO. But, since our TZO method is only approximate, it is not surprising to see imperfect alignments of reflections in CRP gathers. This is evident in the

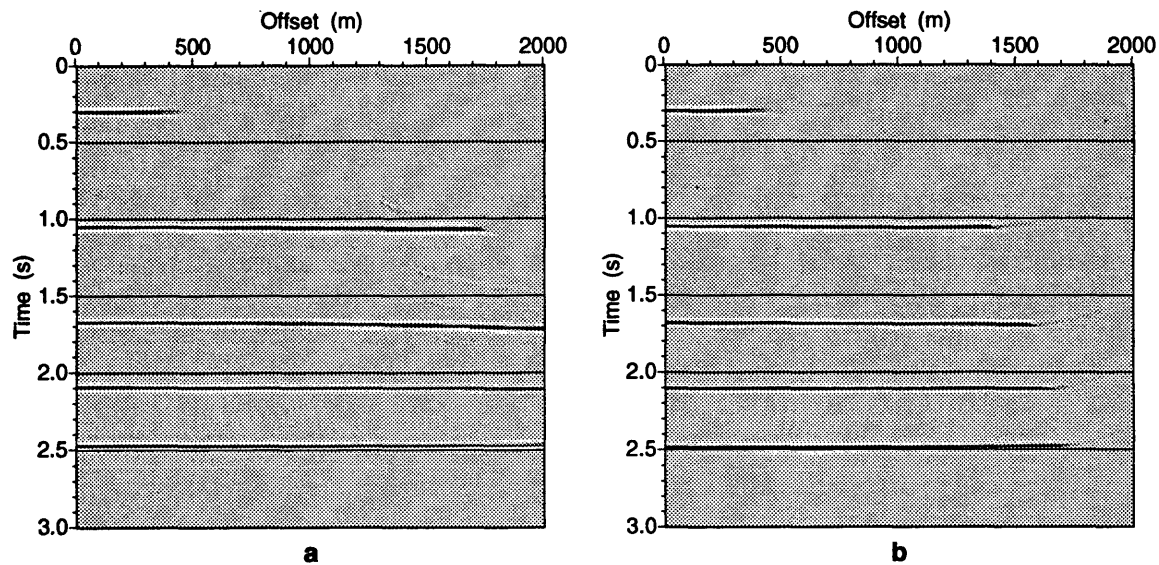


FIG. 4.6. CRP gathers obtained by processing the mode-converted data with the proposed TZO method that honors mode conversion. Flattening of events is superior to that seen in Figure 4.4 where mode conversion was ignored.

CRP gather of Figure 4.6a, where reflections near 1.7 s are slightly undercorrected on the far-offset traces. Also, both models in Figure 4.6 show slight overcorrection, on the far offsets, of reflections from the deepest reflectors, which dip at 80 degrees.

Unlike the previous situation when poor stacks were obtained by ignoring mode conversion (Figure 4.5), reflections from all reflectors can now be readily stacked without fear of severe signal degradation. Figure 4.7 shows stacks of CRP gathers processed using the mode-converted TZO method; the stacks show structures that are the same as those in the zero-offset models of Figure 4.1, although the wavelet here is mildly distorted due to less than perfect alignment of reflections within the CRP gathers. The weak amplitude seen at lower midpoint locations of the stacks (more so for the negative-dip stack) is attributable to two reasons. First, the mode-converted TZO operator, as with the conventional DMO operator, moves the energy updip.

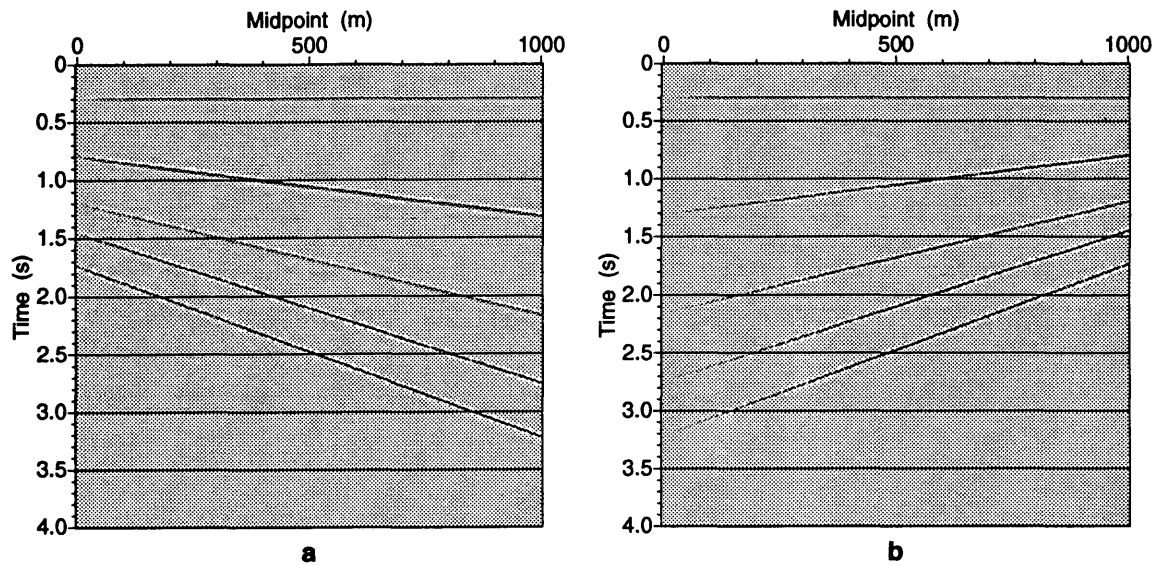


FIG. 4.7. Stacks of CRP gathers processed using the mode-converted TZO method. Unlike those shown in Figure 4.5 for the TZO method that ignores mode conversion, the stacks in both (a) and (b) here are comparable to the zero-offset data in Figure 4.1.

Second, with the receivers situated to the right of the source, the TZO operator further shifts reflection points for p–sv data to the right. This latter reason also explains the weakened amplitudes seen at lower midpoint locations for the horizontal reflectors (shallowest) in both models. The weakening of amplitudes for the negative-dip case (Figure 4.7b) is due to the combined action of these two shifts.

4.3 Depth-variable velocity

In the preceding section, we saw how the mode-converted TZO method was able, to a great extent, to correct mode-converted seismic data when the medium velocity was assumed constant. We now investigate the situation when the velocity function varies with depth. We begin by showing that the proposed, constant-velocity TZO method can be modified, in a simple and a practical way, to handle velocity variations

with depth. The modification here is simply achieved by further *squeezing* the derived (stretched/squeezed) TZO operator given in Section 3.6. We then apply the modified TZO method to synthetic, mode-converted seismic data, assuming a velocity function that varies linearly with depth.

4.3.1 TZO operator for depth-variable velocity

To approximately handle velocity variations with depth for ordinary p-waves, Hale and Artley (1991) proposed the concept of squeezed DMO, an efficient method that yields reasonably accurate results. We have already made use of their squeeze concept in Section 3.6. There, the TZO operator for mode-converted waves was squeezed/stretched to better resemble the theoretical operator in a constant-velocity medium. Here, we use Hale and Artley's squeeze concept, once more, but the aim now is to allow the constant-velocity TZO operator for mode-converted waves to better handle velocity variations with depth.

To study TZO when velocity varies with depth, I empirically analyze synthetic, mode-converted seismic data, assuming a linear velocity function with depth, given by

$$v(z) = v_0 + G z,$$

where v is the downgoing velocity as a function of depth z , v_0 is the downgoing velocity at the surface, and $G = \Delta v / \Delta z$ denotes the downgoing-velocity gradient with respect to depth. I then apply a slightly modified version of Hale and Artley's squeeze idea to the data. The modification is solely that I choose a different squeeze factor than theirs, keeping in mind that this squeezing action is in addition to the modifications (squeezing/stretching) already incorporated into the TZO operator developed in Section 3.6. The additional squeeze factor here, which I also choose as a function

of only the velocity ratio, is just to make the constant-velocity TZO operator better cope with situations when velocities vary with depth.

For ordinary p-waves, Hale and Artley found that an additional squeeze factor $A = 0.6$ is sufficient to make the constant-velocity TZO approximately handle velocity variations with depth. Applying the constant-velocity TZO to vertically inhomogeneous media, therefore, requires an overall squeeze factor given by

$$\tilde{S} = A S,$$

where we recall from Section 3.6.2 that $S = 0.62$ is a squeeze factor Hale and Artley applied even when velocity is a constant. For mode-converted waves in homogeneous media, however, we needed two factors, S_1 and S_2 in equations (3.22) and (3.23), to tailor the TZO operator to better resemble the theoretical one. Consequently, we deal with two overall factors, \tilde{S}_1 and \tilde{S}_2 , when velocity changes with depth for mode-converted waves.

Numerical results of tests with different velocity ratios and different velocity gradients show that the required overall factors for mode-converted waves can be estimated from the following relations

$$\begin{aligned}\tilde{S}_1 &= \gamma A S_1, \\ \tilde{S}_2 &= \gamma A S_2,\end{aligned}\tag{4.1}$$

where $A = 0.6$ is the additional squeeze factor given by Hale and Artley (1991) for ordinary p-waves ($\gamma = 1$) when velocity varies with depth. From equation (4.1), the additional squeeze factor needed for depth-variable velocity for mode-converted waves is thus γA , which reduces to A , Hale and Artley's additional squeeze factor for

ordinary p-waves ($\gamma = 1$).

Figure 4.8 shows four examples of CRP gathers processed using overall stretch/squeeze factors calculated from equation (4.1), assuming different velocity gradients (0.4, 0.5, 0.6, and 0.8 s^{-1}). Each CRP gather contains reflections from five reflectors, with negative reflector dips ranging from zero (shallowest) to 80 degrees (deepest), in increments of 20 degrees. In each model, p–sv mode conversion is assumed, with $\gamma = 0.5$, and the downgoing velocity at the surface is 2500 m/s.

The good alignment in the results of Figure 4.8 suggests that the squeezed TZO approach for mode-converted waves provides a natural and efficient method of TZO correction for depth-variable velocity. The empirical relation for the squeeze factor given by equation (4.1) therefore provides an extension, to mode conversion, of the concept of squeezed DMO for depth-variable velocity introduced by Hale and Artley (1991) for ordinary p-waves. Next, I show, more fully, implementation of squeezed TZO on mode-converted seismic data, using relation (4.1), for a velocity function that varies linearly with depth.

4.3.2 Depth-variable velocity: synthetic examples

Here, we consider a depth model consisting of five reflectors with negative dips. The shallowest reflector is horizontal, the deepest dips at 80 degrees, and the dip increment is 20 degrees. We assume a downgoing velocity v that increases linearly with depth z , i.e.,

$$v(z) = v_0 + Gz, \quad (4.2)$$

where the downgoing velocity at the surface $v_0 = 2500$ m/s, and the gradient of the downgoing velocity $G = 0.7$ s^{-1} . We assume p–sv mode conversion, with a velocity ratio of 0.5. The zero-offset section associated with this depth model is exhibited

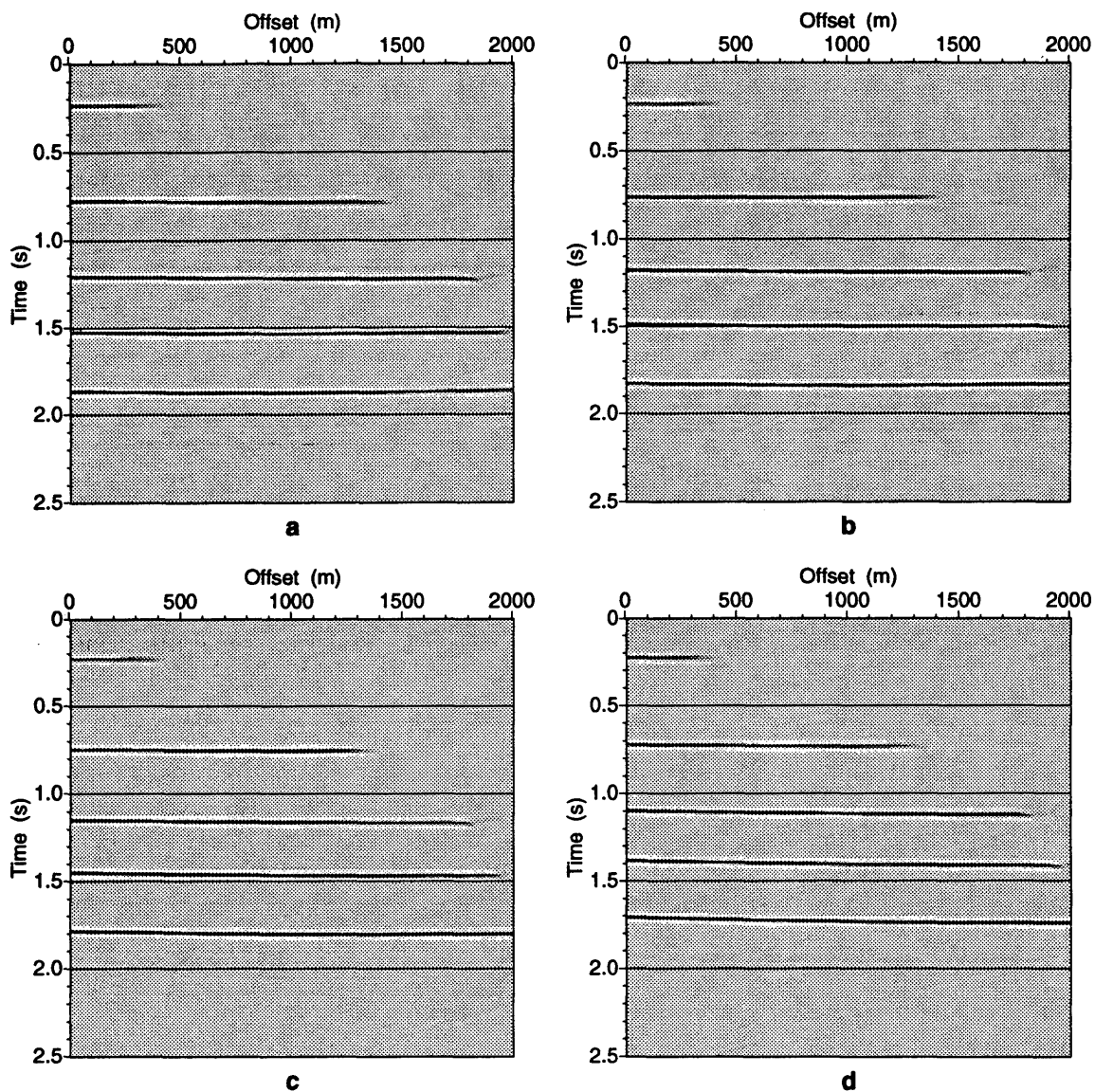


FIG. 4.8. CRP gathers processed with a squeezed TZO operator that approximately handles velocity variations with depth. The velocity gradients used in generating the data in (a), (b), (c), and (d) are, respectively, 0.4, 0.5, 0.6, and 0.8 s^{-1} . The velocity ratio and the downgoing velocity at the surface are 0.5 and 2500 m/s, respectively. The overall stretch and squeeze factors used here are $\tilde{S}_1 = 1.5$ and $\tilde{S}_2 = 0.01$, calculated from equation (4.1).

in Figure 4.9. Note that, since velocity varies with depth, the reflections from the

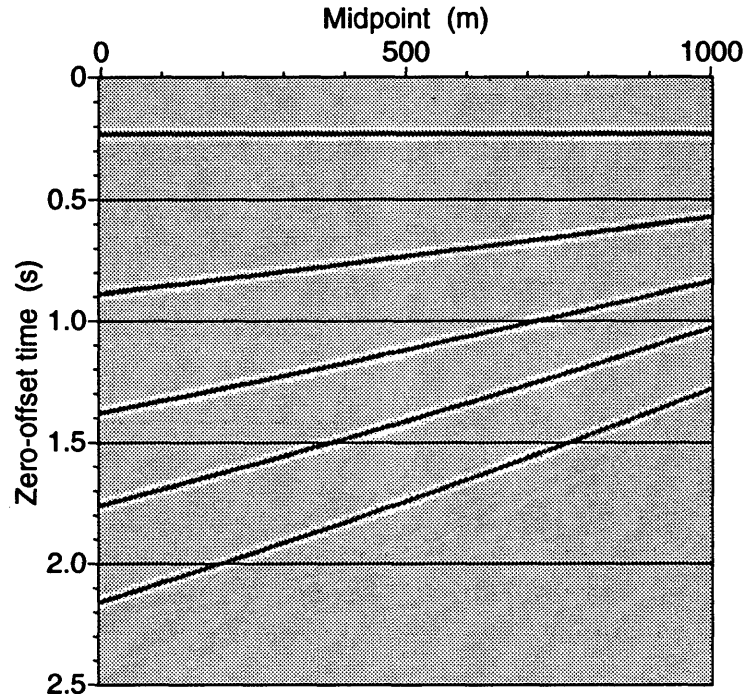


FIG. 4.9. Zero-offset model used to generate synthetic p-sv data. The model shows zero-offset reflections from five reflectors in a medium where velocity varies linearly with depth. The downgoing velocity at the surface and the gradient of the downgoing velocity are 2500 m/s and 0.7 s^{-1} , respectively, and the sv-p velocity ratio is 0.5. The shallowest reflector is horizontal, the deepest reflector dips at 80 degrees, and the dip increment is 20 degrees.

various flat, dipping reflectors are slightly curved. Again, we shall use the middle midpoint at 500 m as a test point to study various output results. The synthetic data here have the same properties (spacing, wavelet, sampling interval, etc.) as those of the constant-velocity case (Section 4.2).

The CMP gather corresponding to the test point of the model is shown in Figure 4.10a. As with the constant-velocity case, the moveout curves are nonhyperbolic,

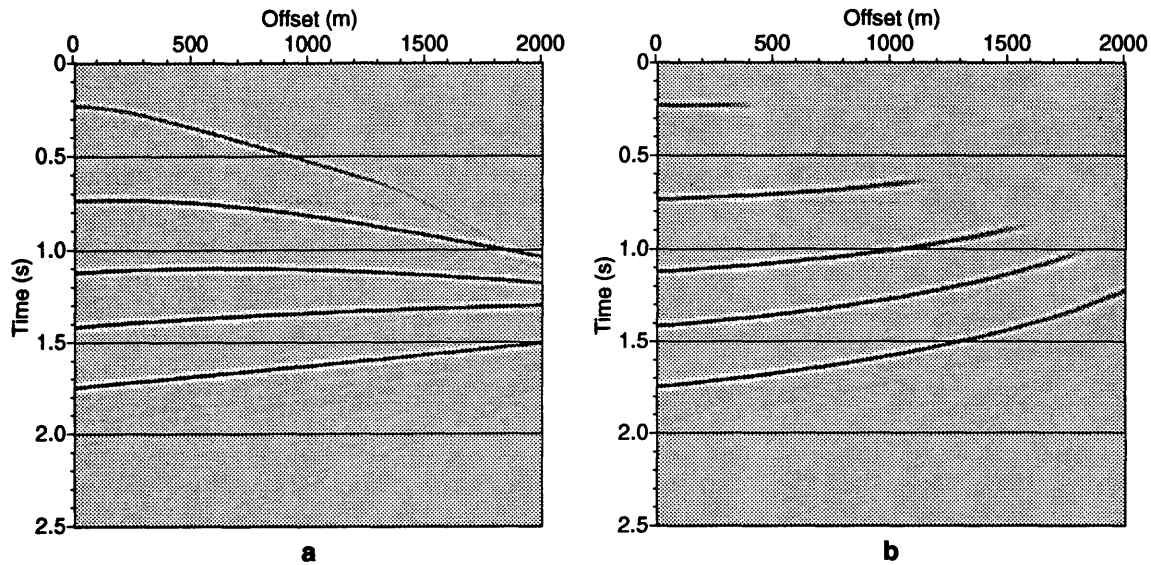


FIG. 4.10. Synthetic p-sv CMP gather (a), and (b) after applying NMO correction. Both gathers correspond to the middle midpoint of Figure 4.9. The downgoing velocity at the surface and the downgoing-velocity gradient are 2500 m/s and 0.7 s^{-1} , respectively; the velocity ratio is 0.5.

and their apices are not located at zero-offset. The CMP gather, again, exhibits reverse moveout for dipping reflections, as in the constant-velocity case (Figure 4.2b).

To perform the NMO correction for this depth-variable velocity, we use a root-mean-square (RMS) velocity, V_{nmo} , which is an extension of v_{nmo} given by equation (3.9) for the constant-velocity case. We replace the constant downgoing velocity, v in equation (3.9), by the corresponding RMS velocity, v_{rms} , since the medium velocity is no longer a constant. That is, for depth-variable velocity the NMO velocity for mode-converted waves, V_{nmo} , is given by

$$V_{nmo}^2 = \gamma v_{rms}^2, \quad (4.3)$$

where the RMS velocity v_{rms} is calculated based on the downgoing velocity function

$v(z)$ given in equation (4.2). As with the constant-velocity case, the velocity required here to approximately flatten reflections from horizontal reflectors on CMP gathers is also somewhat higher than V_{nmo} given by equation (4.3). Numerical results show that the required increase above V_{nmo} here can also be estimated from the same relation for the constant-velocity case given by equation (3.10).

The NMO-corrected gather corresponding to Figure 4.10a is shown in Figure 4.10b. In that figure, only the horizontal reflections (shallowest) are correctly aligned. In addition, and as with the constant-velocity case, dipping reflections are now severely overcorrected. Obviously, NMO correction alone is not enough to produce a good stack since reflections from dipping reflectors are present.

Just as in the constant-velocity case, let us emphasize, once more, the negative consequence of erroneously TZO-processing the mode-converted data by ignoring mode conversion. Figure 4.11a shows a CRP gather corresponding to the NMO-corrected gather of Figure 4.10b, resulting from application of Hale's $f-k$ TZO method. Again, TZO applied erroneously by ignoring mode conversion *fails* to correct the data. CRP gathers processed in this way, therefore, will produce a poor stack.

Figure 4.11b shows the same CRP gather, but processed now using the mode-converted TZO method. For this CRP gather, the overall stretch and squeeze factors, $\tilde{S}1 = 1.50$ and $\tilde{S}2 = 0.01$, were calculated using equation (4.1). Alignments of reflections are much improved.

Stacks of the processed data from both the conventional and the mode-converted TZO methods are shown in Figure 4.12. While dipping events are almost completely wiped out in the stack of the conventional-TZO data, the mode-converted TZO method was able to produce the same structure as that of the zero-offset model (Figure 4.9). As discussed in the constant-velocity case, the weak amplitude at lower

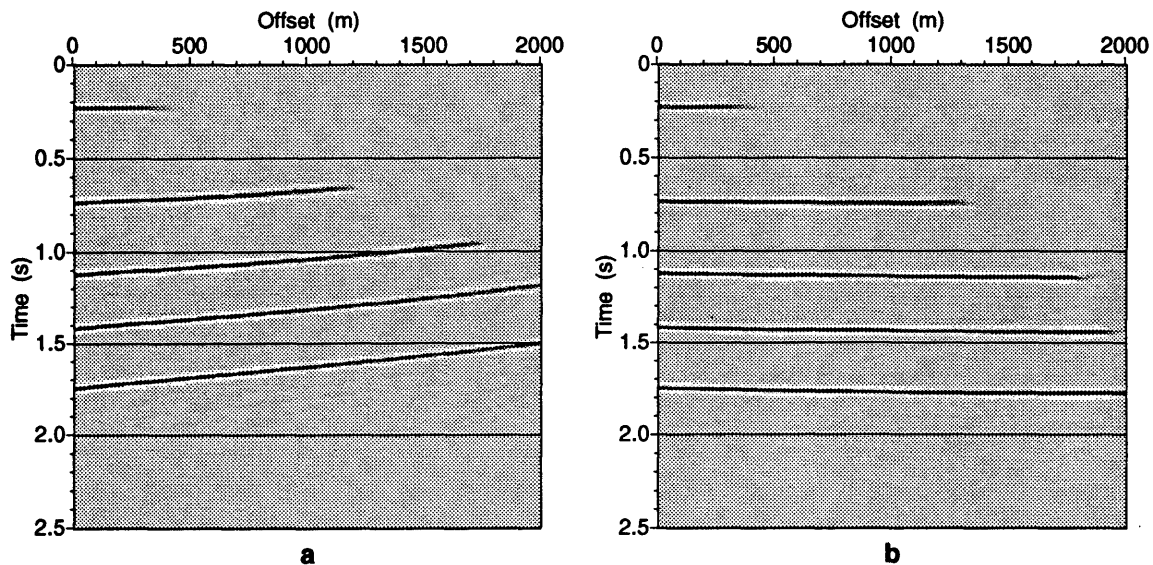


FIG. 4.11. CRP gathers corresponding to the NMO-corrected gather of Figure 4.10b. (a) is obtained by processing the mode-converted data with a conventional TZO algorithm that ignores mode conversion. Only the horizontal reflection (shallowest) is properly aligned. (b) is the same gather obtained by applying the mode-converted TZO method.

midpoints in Figure 4.12b is due to the tendency of the mode-converted TZO operator to move energy toward the right.

Finally, we study the sensitivity of the mode-converted TZO method to the choice of the overall stretch/squeeze factors when velocity varies with depth. Figure 4.13 shows two CRP gathers, which are the same as the CRP gather depicted in Figure 4.8b, but processed now using different stretch/squeeze factors. Recall, for a velocity ratio $\gamma = 0.5$, the additional squeeze factor $\gamma A = (0.5)(0.6) = 0.3$, so that equation (4.1) gives the overall stretch and squeeze factors $\tilde{S}_1 = 1.5$ and $\tilde{S}_2 = 0.01$ used in generating the CRP gather of Figure 4.8b. In Figure 4.13a, the additional squeeze factor used was just $\gamma A = 0.6$ (as if $\gamma = 1$), the same factor suggested by Hale and Artley (1991) for ordinary p-waves when velocity varies with depth. The

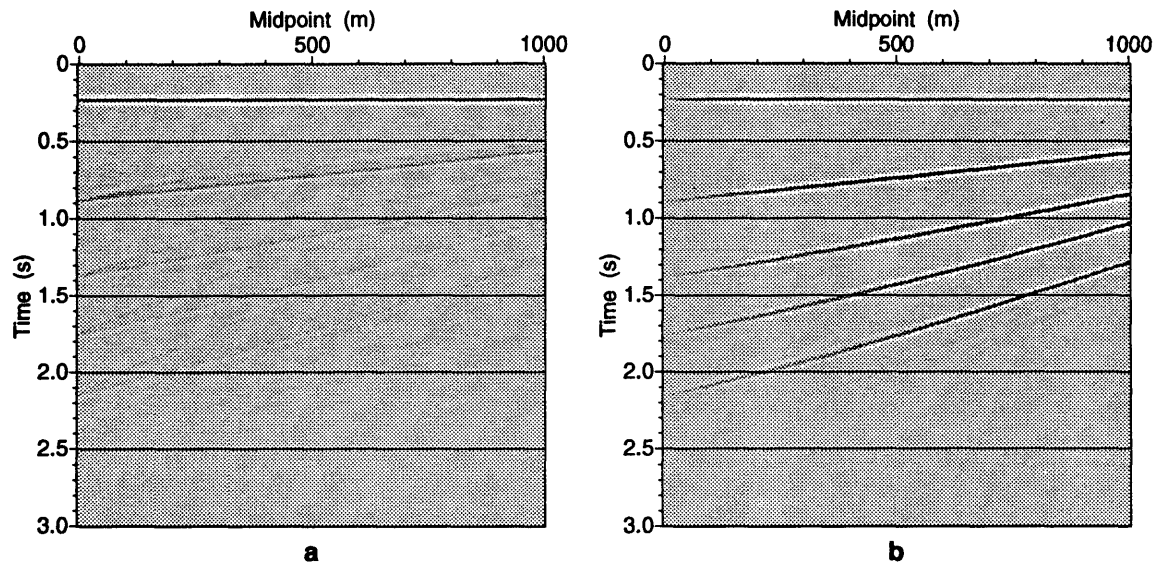


FIG. 4.12. Stacks of CRP gathers. The data in (a) were processed by ignoring mode conversion; those in (b) were processed using the mode-converted TZO method. Reflections from only the horizontal reflector (shallowest) stack properly when mode conversion is ignored (a). The mode-converted TZO method produces a stack that has the same structure as that of the zero-offset model depicted in Figure 4.9.

corresponding overall stretch and squeeze factors in this case are (equation [4.1]) $\tilde{S}1 = 3.0$ and $\tilde{S}2 = 0.025$. In Figure 4.13b, the additional squeeze factor used was $\gamma A = 1.0$, implying no additional squeezing at all. The corresponding overall stretch and squeeze factors in this case are $\tilde{S}1 = 5.0$ and $\tilde{S}2 = 0.04$.

Comparing Figures 4.13a and 4.13b with Figure 4.8b, we observe only minor differences. Namely, far-offset step reflections are slightly undercorrected in the CRP gathers of Figure 4.13. Nevertheless, use of overall stretch and squeeze factors based on equation (4.1) yields better results, as Figure 4.8b shows.

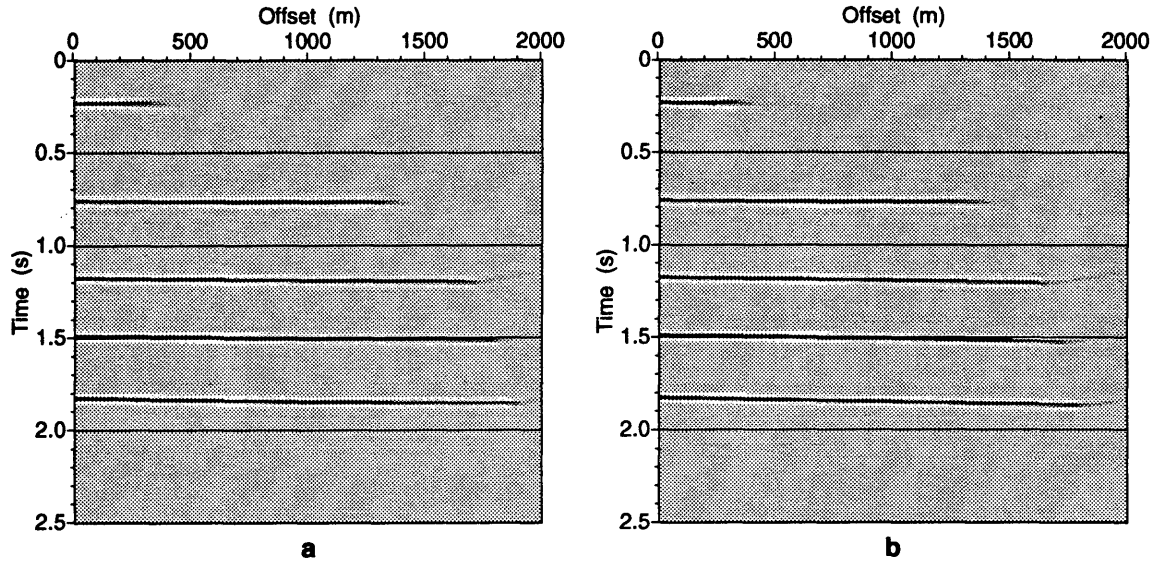


FIG. 4.13. CRP gathers corresponding to the CRP gather depicted in Figure 4.8b, but now processed using different stretch and squeeze factors. The overall stretch and squeeze factors in (a) are $\tilde{S}1 = 3.0$ and $\tilde{S}2 = 0.025$; those in (b) are $\tilde{S}1 = 5.0$ and $\tilde{S}2 = 0.04$.

4.4 Sensitivity to velocity ratio

Because of added modifications (empirical for the most part), the TZO operator now is hard to describe analytically. However, we can still use equation (3.11), which analytically describes the TZO operator in its first stage (no modifications), to get a general idea as to how the operator behaves with varying parameters. Specifically, we study equation (3.11) to get a rough idea as to the sensitivity of the TZO method to the choice of the velocity ratio γ used in the processing.

By sensitivity to the choice of the velocity ratio, we mean how the zero-offset time t_0 changes, after applying TZO, when we choose an erroneous γ . As a sensitivity measure for TZO, we use the rate of change of t_0 with respect to γ , i.e. $\partial t_0 / \partial \gamma$. Taking the partial derivative of t_0 in equation (3.11) with respect to γ , and after

simplification, we obtain

$$\frac{\partial t_0}{\partial \gamma} = \frac{4h \sin \theta}{v_a(1 + \gamma)^2} \left[1 + \frac{2h(1 - \gamma) \sin \theta}{\sqrt{v_a^2(1 + \gamma)^2 t_n^2 + 16\gamma h^2 \sin^2 \theta}} \right], \quad (4.4)$$

where we recall that θ is the dip angle, and t_n is the NMO-corrected time. Error in t_0 , i.e. Δt_0 , can be estimated from the following expression

$$\Delta t_0 = \frac{\partial t_0}{\partial \gamma} \Delta \gamma, \quad (4.5)$$

where $\Delta \gamma$ is the error in the estimation of the velocity ratio γ . The general behavior of the sensitivity measure $\partial t_0 / \partial \gamma$ in equation (4.4) is hardly obvious. Detailed sensitivity analysis is given later in this section, but for now we can draw a few trivial conclusions.

First, for reflections from horizontal reflectors, the TZO method is insensitive to the choice of γ . That is, because $\sin \theta$ is 0 for horizontal reflectors, then $\partial t_0 / \partial \gamma$ is 0, too, as equation (4.4) implies. That the TZO method is not sensitive to γ for horizontal reflections is also true for depth-variable velocity, although the sensitivity measure is derived here based on constant-velocity TZO. Figure 4.14 shows two CRP examples for a velocity function that varies linearly with depth. In both examples, reflections are the same as those depicted in Figure 4.11b, but now using erroneous velocity ratios in the TZO processing. The velocity ratio in Figure 4.14a is 20% too high, and that in Figure 4.14b is 20% too low. As expected, in both examples the horizontal reflections (shallowest) are not altered by the erroneous choice of velocity ratio.

A second observation is that, due to the dependence on the term $\sin \theta$ in equation (4.4), not only does the sensitivity depend on dip, but also on the sign of dip. Third, the sensitivity, and thus the error Δt_0 , increases with increasing offset. This is

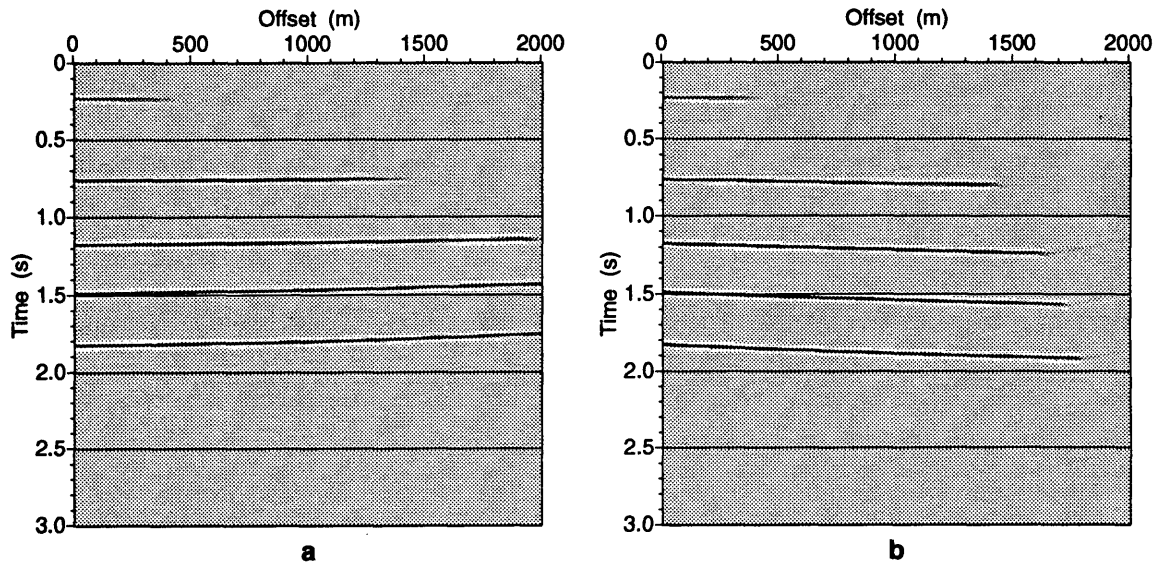


FIG. 4.14. CRP gather of Figure 4.11b, but now processed erroneously. The velocity ratio used in (a) is 20% too high (0.6), that in (b) is 20% too low (0.4), both relative to the correct value $\gamma = 0.5$.

obvious in both Figures 4.14a and 4.14b, where error in t_0 (poor horizontal alignment) increases with increasing offset for reflections from dipping reflectors.

Let us now further investigate the sensitivity measure given by equation (4.4), by incorporating two simplifying assumptions. Namely, we shall assume the presence of steep reflectors ($\sin \theta \approx 1$), and that the maximum offset is equal to the depth of the reflector under consideration. The first assumption ($\sin \theta \approx 1$) is extreme because the proposed TZO method is clearly most sensitive to γ for steep reflectors. The latter assumption implies that half-offset can be expressed as $h = t_0 v_a / 4$. Substituting this into equation (4.4), setting $\sin \theta = 1$, and simplifying, gives

$$\frac{\partial t_0}{\partial \gamma} = \frac{t_0}{(1 + \gamma)^2} \left[1 + \frac{t_0(1 - \gamma)}{2\sqrt{(1 + \gamma)^2 t_n^2 + \gamma t_0^2}} \right]. \quad (4.6)$$

We then use equations (3.8) and (2.16) to express t_n^2 in terms of t_0^2 as follows

$$t_n^2 = t_0^2 + \frac{4ht_0(1-\gamma)\sin\theta}{(1+\gamma)v_a} + \frac{4h^2[(1-\gamma)^2 - 4\gamma]\sin^2\theta}{(1+\gamma)^2v_a^2}. \quad (4.7)$$

Setting $\sin\theta = 1$ and $h = t_0v_a/4$ in equation (4.7), substituting the resulting t_n^2 into equation (4.6), and after simplification, we get

$$\frac{\partial t_0}{\partial \gamma} = \frac{t_0}{(1+\gamma)^2} \left(1 + \frac{1-\gamma}{3+\gamma} \right), \quad (4.8)$$

which implies that the sensitivity of TZO, for large dip and at large offset, depends on zero-offset time t_0 as well as on the velocity ratio γ .

To see how much error in γ we can tolerate without severely degrading the data, let us allow a maximum error in t_0 that is equal to half a cycle. That is

$$\Delta t_0 \leq \frac{1}{2f},$$

where f is the dominant frequency. Then, from equations (4.5) and (4.8), the error that we can tolerate in this case is given by the following inequality

$$\Delta \gamma \leq \frac{(1+\gamma)^2}{2t_0f \left(1 + \frac{1-\gamma}{3+\gamma} \right)}. \quad (4.9)$$

For a velocity ratio of 0.5, and a frequency of 25 Hz, as in the synthetic data considered previously, and assuming $t_0 = 2$ s, the above inequality allows for a maximum error in γ of about 4%. Such a small tolerable error indicates that the TZO method here is highly sensitive to the choice of the velocity ratio if steep reflectors are present. Figure 4.15 shows erroneous versions of the CRP gather depicted in Figure 4.6b for the constant-velocity case. The erroneous velocity ratios used here are 5% too high

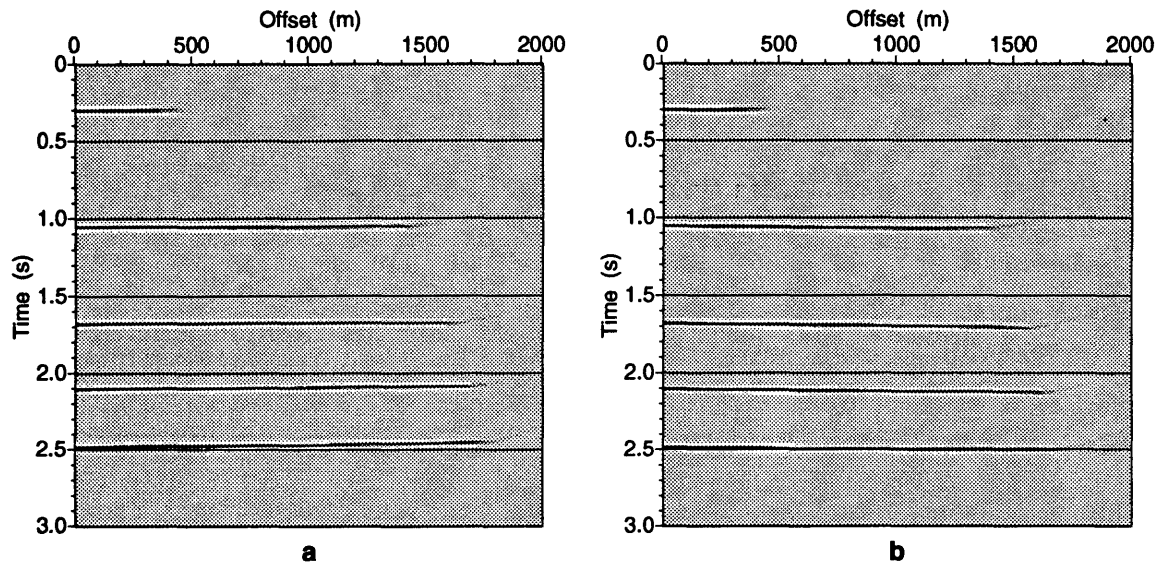


FIG. 4.15. CRP gather of Figure 4.6b, but now processed erroneously. The velocity ratio used in (a) is 5% too high (0.525), that in (b) is 5% too low (0.475), both relative to the correct ratio $\gamma = 0.5$.

in Figure 4.15a, and 5% too low in Figure 4.15b, relative to the correct ratio $\gamma = 0.5$. Horizontal reflections in both examples (shallowest) are not altered, reflections from small to moderate dips are slightly misaligned, and those associated with large dips (deepest) are most misaligned, but not too severely.

As suggested by equation (4.5), when the error in the velocity ratio γ further increases, we should expect to see more error in t_0 from reflections associated with dipping reflectors. Figure 4.16 shows the data in Figure 4.15 but now processed using erroneous velocity ratios that are 10% different from the correct value. Again, horizontal reflections here are not altered by choosing erroneous velocity ratios. However, reflections from steep reflectors are now severely erroneous and, consequently, will not produce a good stack (see reflections from the two deepest reflectors in Figures 4.16a and 4.16b).

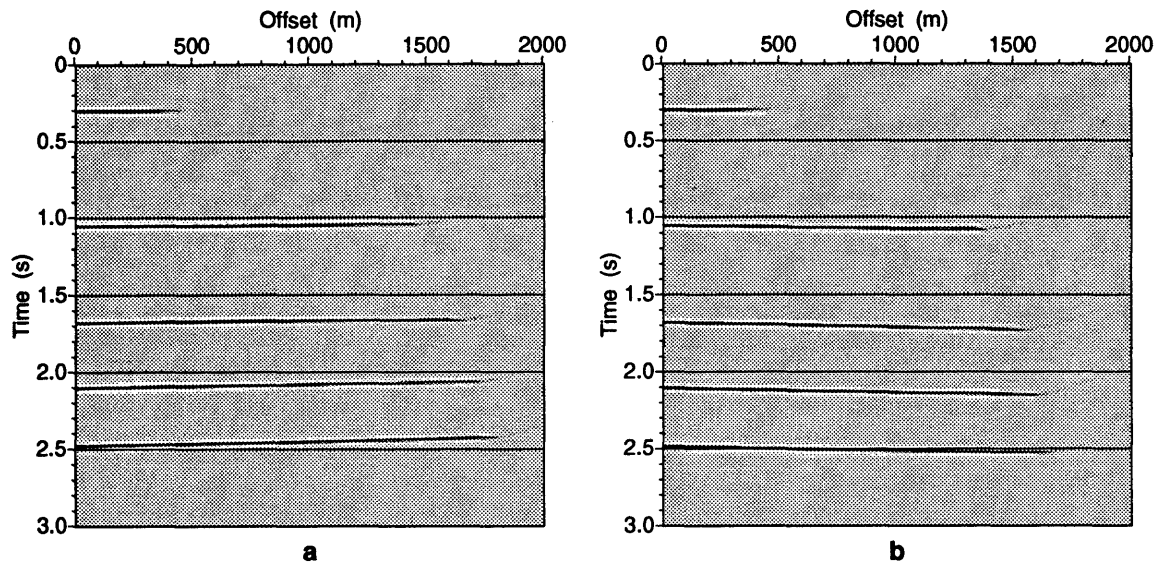


FIG. 4.16. CRP gather of Figure 4.6b, but now processed erroneously. The velocity ratio used in (a) is 10% too high (0.55), that in (b) is 10% too low (0.45), both relative to the correct ratio $\gamma = 0.5$.

Based on the analysis and numerical examples given in this section, we conclude that the proposed TZO method can tolerate error up to about 10% in γ for small dips (up to about 30 degrees). The method is highly sensitive to γ when large dips are present.

4.4.1 Error in Poisson's ratio

As an aside, let us investigate the error in Poisson's ratio (an elastic modulus) arising from assuming an erroneous velocity ratio. Assuming p-sv mode-conversion, Poisson's ratio, σ_P , is expressed in terms of the velocity ratio γ as

$$\sigma_P = \frac{2\gamma^2 - 1}{2(\gamma^2 - 1)}. \quad (4.10)$$

Differentiating equation (4.10) with respect to γ , and simplifying, we get

$$\begin{aligned}\frac{d\sigma_P}{d\gamma} &= -\frac{\gamma}{(\gamma^2 - 1)^2}, \\ \frac{d^2\sigma_P}{d\gamma^2} &= \frac{3\gamma^2 + 1}{(\gamma^2 - 1)^3}.\end{aligned}\quad (4.11)$$

Assuming a second-order Taylor-series expansion, error in σ_P , i.e. $\Delta\sigma_P$, is found from the expression

$$\Delta\sigma_P = \frac{d\sigma_P}{d\gamma} \Delta\gamma + \frac{d^2\sigma_P}{d\gamma^2} \frac{(\Delta\gamma)^2}{2}, \quad (4.12)$$

where $\Delta\gamma$ denotes error in the velocity ratio γ . Then, from equations (4.10), (4.11), and (4.12), we get

$$E_{\sigma_P} \equiv \frac{\Delta\sigma_P}{\sigma_P} = \frac{2\gamma\Delta\gamma}{(\gamma^2 - 1)(2\gamma^2 - 1)} + \frac{(\Delta\gamma)^2(3\gamma^2 + 1)}{(\gamma^2 - 1)^2(2\gamma^2 - 1)}, \quad (4.13)$$

which gives the normalized error in Poisson's ratio as a function of $\Delta\gamma$, the error in the velocity ratio. For velocity ratios $\gamma = 0.4, 0.5,$ and 0.6 , and assuming 10% error in γ , that is,

$$E_\gamma \equiv \frac{\Delta\gamma}{\gamma} = 0.1, \quad (4.14)$$

the corresponding errors in Poisson's ratio, calculated from equation (4.13), are 5%, 12%, and 34%, respectively. For 20% error in γ , the above errors in Poisson's ratio become 9%, 20%, and 54%. Thus the error in Poisson's ratio increases with increasing velocity ratio.

To study the implication of the above error, let us further analyze the error in Poisson's ratio relative to that in the velocity ratio. For simplicity here, we ignore the second term on the right-hand side of equation (4.11), implying a first-order Taylor expansion as opposed to the original second-order. Then from equations (4.14) and

the truncated version of (4.13), we have

$$R \equiv \frac{E_{\sigma_P}}{E_\gamma} = -\frac{2\gamma^2}{(\gamma^2 - 1)(2\gamma^2 - 1)}. \quad (4.15)$$

To find the value of velocity ratio at which the two errors E_{σ_P} and E_γ are equal, we set $R = 1$ in equation (4.15) and solve for γ . This gives a value of $\gamma = 0.47$. For velocity ratios less than this threshold value, errors in Poisson's ratio are less than those in the velocity ratios; for greater velocity ratio, error in Poisson's ratio is quite magnified. For example, $\gamma = 0.3$ yields $R = 0.24$, indicating that E_{σ_P} is much less than E_γ ; however, $\gamma = 0.7$ corresponds to $R = 96$, implying a remarkably large error in Poisson's ratio.

A practical way of looking at the implication of the error is to study the lower and upper limits that one is likely to encounter in exploration geophysics, for both γ and σ_P . For example, the maximum value of σ_P found in sedimentary rocks is 0.32—for limestone (Clark, 1966). This corresponds to $\gamma = 0.51$. At the other extreme, shale can attain the smallest possible values of σ_P (0.04–0.12, Clark, [1966]), corresponding to a range of velocity ratios of 0.69–0.66. Although we observe that a typical velocity ratio is most likely to lie in the range 0.5–0.7, ratios as low as 0.2 have been reported in geophysical literatures (e.g., Corbin, et al., 1988). Moreover, Dobrin and Savit (1988) noted that the velocity ratio, for many rocks encountered in exploration geophysics, is typically $\gamma = 0.5$; error in Poisson's ratio for such rocks, as we have found above, will be comparable to that in the velocity ratio.

Chapter 5

APPLICATION TO FIELD DATA

5.1 Introduction

In this chapter, we discuss results of processing two field data sets consisting of mode-converted (p-sv) reflections. The data, acquired in the southern San Joaquin Valley of California, are courtesy of Chevron Oil Field Research Company. The two data sets were recorded over the same area, but each shot in a different direction. That is, the two data sets differ in that the receiver locations were on opposite sides of the source position in the two surveys. I shall refer to the data set whose receivers are located on the right of the source as Line 1, and to the other set (receivers on the left of source) as Line 2.

For comparison, I process the data in different ways: (1) processing with no regard to TZO; that is, the data are stacked using conventional stacking velocity; (2) processing with conventional TZO that does not honor mode conversion; and (3) processing with mode-converted TZO.

To apply mode-converted TZO, I start by estimating a velocity ratio that would be suitable for processing the entire data. I achieve this by conducting both qualitative and quantitative analyses on the data. In the qualitative approach, I simply compare TZO-processed gathers, obtained from applying different velocity ratios, with one another as well as with unprocessed gathers. I then choose that ratio which, in my view, yields the best reflection continuity, as the velocity ratio to use in TZO

processing. I complement this qualitative analysis by also studying constant-velocity stacks (CVSs), obtained both conventionally and after TZO (assuming different velocity ratios) has been applied.

The quantitative approach for estimating γ , on the other hand, is based on a formula that, as we shall see, makes use of lateral shifts of stacked reflections in Line 1 relative to those in Line 2. Based on both the qualitative and quantitative approaches, I find that any velocity ratio γ in the range 0.4–0.5 (corresponding to Poisson's ratios $\sigma_P = 0.4$ –0.3) is a reasonable estimate for the data here. I choose to use $\gamma = 0.4$ in applying mode-converted TZO to the two lines.

Finally, I compare the stacking velocities obtained without and with mode-converted TZO.

5.2 Field geometry and preprocessing

Each data set consists of 188 shot gathers, each gather has 60 receivers, covering a total surface distance of about 26000 ft. Within each shot gather, the nearest receiver is located 1080-ft from the source, and the receiver spacing is 120 ft, thus yielding a maximum source-receiver offset of 8160 ft. The recorded time is 6 s.

The source is a vertical-motion vibrator; the horizontal-component geophones are oriented so as to detect radial (horizontal, in-line) particle motion. Thus, we assume that the recorded reflections are dominated by mode-converted (p–sv) waves.

Preprocessing consists of applying residual-statics correction (provided by Chevron), muting of early times, gain, and filtering. Two forms of gain were applied to the data, trace balancing and automatic gain control (AGC). In the trace balancing, amplitudes of each trace were divided by the trace root-mean-square (RMS) amplitude, thus compensating for erratic trace-to-trace amplitudes typical in land

surveys. The AGC time window was 0.5 s. The filter is trapezoidal bandpass, with corner frequencies of 5, 10, 30, and 50 Hz.

The preprocessed data were sorted into common-midpoint (CMP) gathers. A total of 444 CMP gathers are formed for each data set. With a nominal fold of 30 traces, the trace spacing within each CMP gather is now 240 ft, and the spacing between adjacent CMP gathers is 60 ft. These CMP gathers are used as inputs to the subsequent processing.

5.3 Conventional processing

In this section, I discuss data processed with no regard to TZO. I first perform velocity analysis on the preprocessed CMP gathers, and then use the velocity functions so-obtained to NMO-correct the data. The stacks of the NMO-corrected gathers for both Line 1 and 2 are shown in Figures 5.1 and 5.2, respectively.

As we recall in the acquisition of the data, the receivers are situated to the right of the source for Line 1, and to the left of the source for Line 2. With this, and since we are dealing with p–sv mode conversion, we expect to see events in Line 2 shift to the right relative to those in Line 1. A close examination of the two stacks reveals that the events are indeed shifted in accordance with the above assertion. Take, for example, the portion of the anticline at 4 s in Line 1, just to the left of the broad horizontal region (about midpoint 245). Now, the same feature in Line 2 intersects 4 s at about midpoint 215, resulting in a total relative shift to the right of $245 - 215 = 30$ midpoints. Allowing ± 5 midpoints for error tolerance, and recalling that the midpoint spacing is 60 ft, the total relative shift is thus $(30 \pm 5) \cdot 60 = 1800 \pm 300$ ft, a quantity I will later use to estimate the velocity ratio.

In Line 1 (Figure 5.1), note that the signal-to-noise ratio is poor on the right

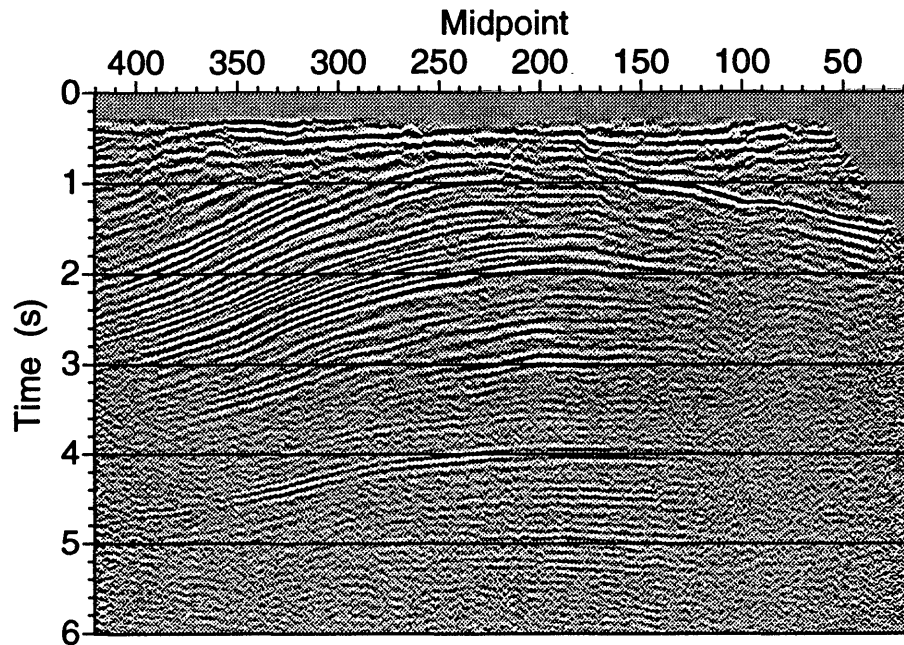


FIG. 5.1. Conventional stack of Line 1 with no TZO. In the acquisition of the data here, the receivers are situated to the right of the source.

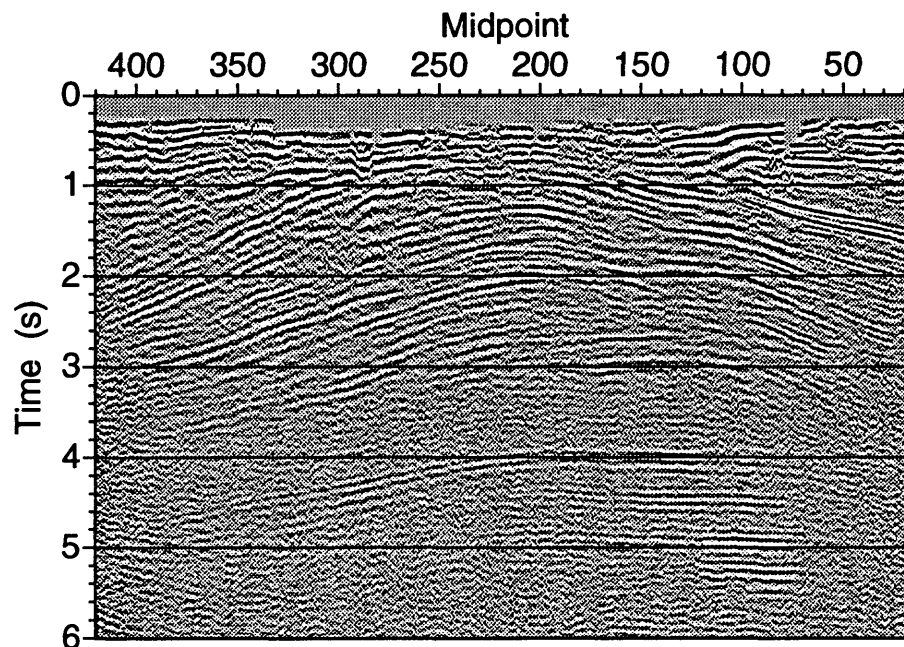


FIG. 5.2. Conventional stack of Line 2 with no TZO. In the acquisition of the data here, the receivers are situated to the left of the source.

portion of the section, particularly after 2 s; Line 2 (Figure 5.2) has a better data quality in the same region, though still poor. In other regions, the data quality of Line 1 is, in general, better than that of Line 2. Compare, for example, the sloping reflections on the left of both sections, between 1 and 3 s. Also, it is obvious from the two stacks that there are no conflicting dips present in the subsurface (e.g., fault-plane reflections). Conflicting dips would have further aided in the assessment of results after applying mode-converted TZO to the two data sets. Below, I compare these sections to their counterparts when mode-converted TZO is performed.

The maximum reflection slope in the data is about 0.2 ms/ft, seen in Figure 5.1 at about 2 s and midpoint 350. I use this slope, assuming parallel bedding, to estimate the maximum dip present in the subsurface. To determine this, I use equation (3.13), which requires knowing the average velocity v_a . Since v_a and the stacking velocity v_s are typically in the same ball park when dip influence is removed from v_s , I take $v_a = v_s$ after removing the dip influence from v_s , i.e., v_s obtained after applying TZO. As we shall see when I analyze velocity, $v_s = 4000$ ft/s is a reasonable estimate of stacking velocity near the surface. Taking $v_a = 4000$ ft/s at the surface, and substituting this along with the slope (0.2 ms/ft) into equation (3.13), yields a maximum dip angle of about 25 degrees. This is a modest dip value when attempting to assess the value of TZO; therefore we should not expect TZO to have a dramatic influence on the imaging of the data in these lines.

5.4 Estimation of velocity ratio

Before applying mode-converted TZO, we first need to estimate a reasonable velocity ratio. In this section, I estimate the velocity ratio in two ways: (1) performing a qualitative analysis of both prestack and poststack data, assuming different velocity

ratios; and (2) calculating the velocity ratio based on quantities measured from the two data sets. As we shall see, both approaches suggest that γ in the range 0.4–0.5 is a good estimate for the velocity ratio.

5.4.1 Qualitative analysis

Here, I apply TZO assuming different velocity ratios, and then compare their results with one another. The tests include eight choices of velocity ratio, from 0.3 to 1.0, in increments of 0.1. Applying TZO assuming both depth-variable velocity and constant velocity, I have found the results to be comparable, as might be expected given that dips do not exceed about 25 degrees. For constant-velocity TZO, the velocity used was 4500 ft/s; this velocity controls two features of the TZO operator, its aperture (lateral extent) and its lateral shift. In addition, since TZO is not too sensitive to the choice of NMO velocity (Hale, 1984), the velocity used for NMO prior to the constant-velocity TZO was also 4500 ft/s. For TZO with depth-variable velocity, the velocities used for both NMO and TZO were those obtained from conventional velocity analysis of prestack data. Below, I show results from only constant-velocity TZO. For each test, the data were first NMO-corrected, then sorted into common-offset gathers prior to TZO.

Let us compare TZO-corrected data resulting from use of different velocity ratios. We first look at unstacked gathers from Line 1, at midpoints 100, 150, and 275. To compare CRP (TZO-corrected) gathers with CMP gathers, I have removed the NMO correction from the CRP gathers. The gathers shown in Figure 5.3 pertain to midpoint 100 of Line 1. Figure 5.3a shows the CMP gather with only preprocessing applied. Figure 5.3b is a CRP gather after applying conventional TZO ($\gamma = 1$). Figures 5.3c, 5.3d, and 5.3e show CRP gathers after applying mode-converted TZO

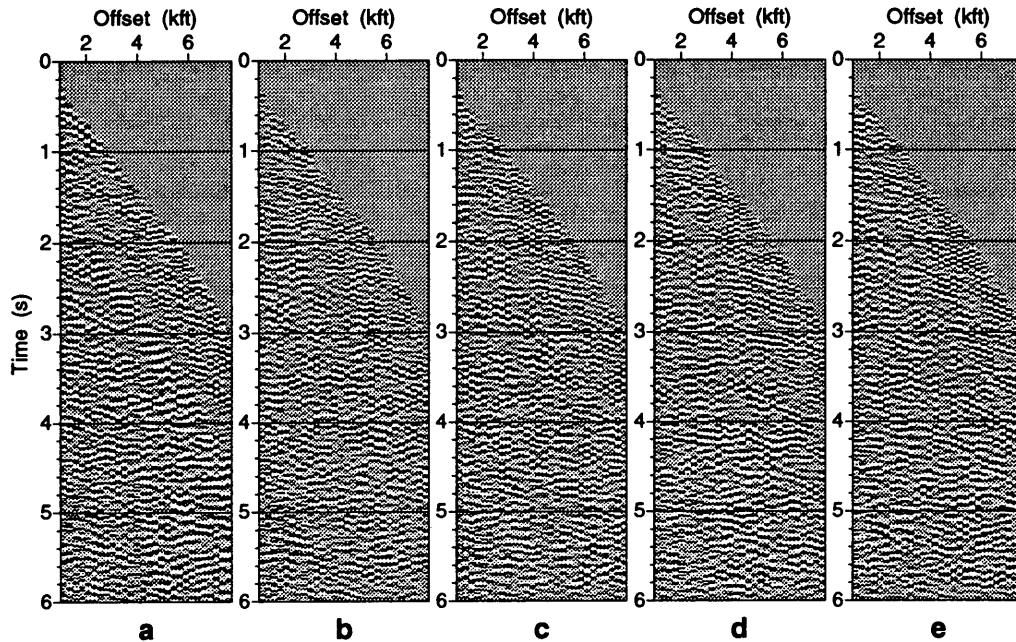


FIG. 5.3. Unstacked gathers corresponding to midpoint 100 of Line 1. The CMP gather with only preprocessing applied is shown in (a). CRP gathers, after undoing the NMO correction, are shown in (b), (c), (d), and (e), with velocity ratios 1.0, 0.6, 0.5, and 0.4, respectively.

assuming velocity ratios of 0.6, 0.5, and 0.4, respectively. In the unstacked gathers of the two mode-converted data sets, the signal-to-noise ratio is poor compared to that of conventional p-wave data from the same area (not shown).

In terms of reflection continuity, I judge CRP gather 5.3e, with $\gamma = 0.4$, to be the best among the CRP gathers shown, including 5.3b which assumes conventional TZO. Compare, for example, the shallow event at 1.2 s, and the events just below 2 s in all gathers. Midpoint 100 is, of course, in the poor-signal portion of the section. The unstacked gathers for midpoints 150 and 275, over better-signal parts of the line, are shown in Figures 5.4 and 5.5, respectively. Again in terms of reflection continuity, the CRP gathers with $\gamma = 0.4$ or 0.5 appear to be best among other

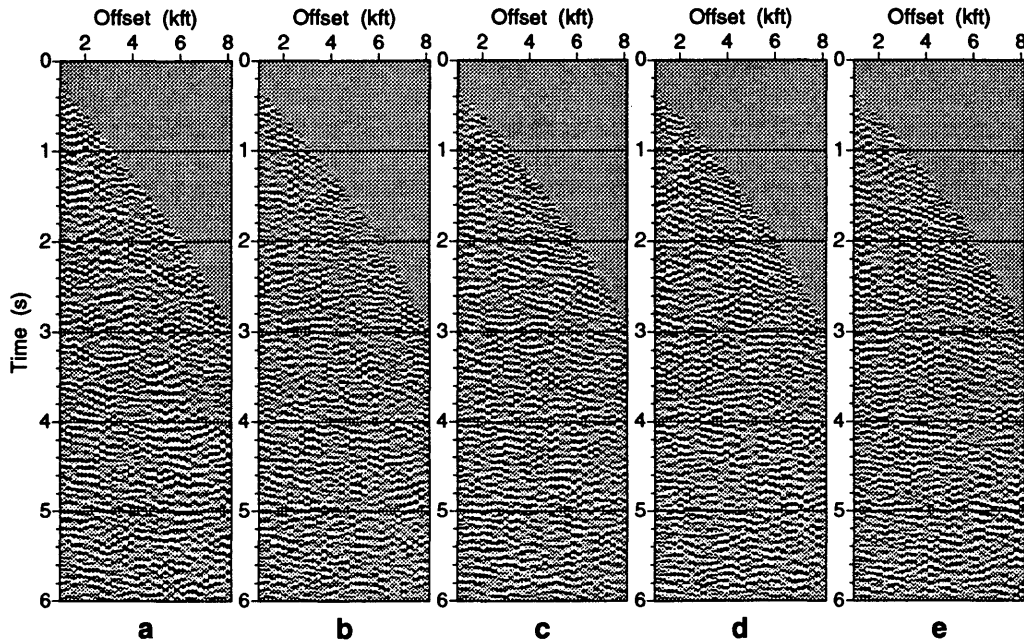


FIG. 5.4. Unstacked gathers corresponding to midpoint 150 of Line 1. The CMP gather with only preprocessing applied is shown in (a). CRP gathers, after undoing the NMO correction, are shown in (b), (c), (d), and (e), with velocity ratios 1.0, 0.6, 0.5, and 0.4, respectively.

gathers, although the reflections quality is far from ideal in any of the panels. Any of the choices, $\gamma = 0.4-0.6$, gives better reflection continuity than that in either the original data or the TZO-corrected data with $\gamma = 1$. However, as we recall from the study of the conversion point (Figure 3.3), the choice of velocity ratio also controls the time-varying lateral shift of reflections imposed by the TZO operator. Since the magnitude of shift depends on the choice of velocity ratio, only those choices of ratio that are close to the actual one in the subsurface will eventually place reflections in their correct positions. Hence, we can expect that reflector continuity might improve with those choices of velocity ratio that are close to the actual one. The conclusion here, that $\gamma = 0.4-0.5$ for the data, was also supported by results from analyzing

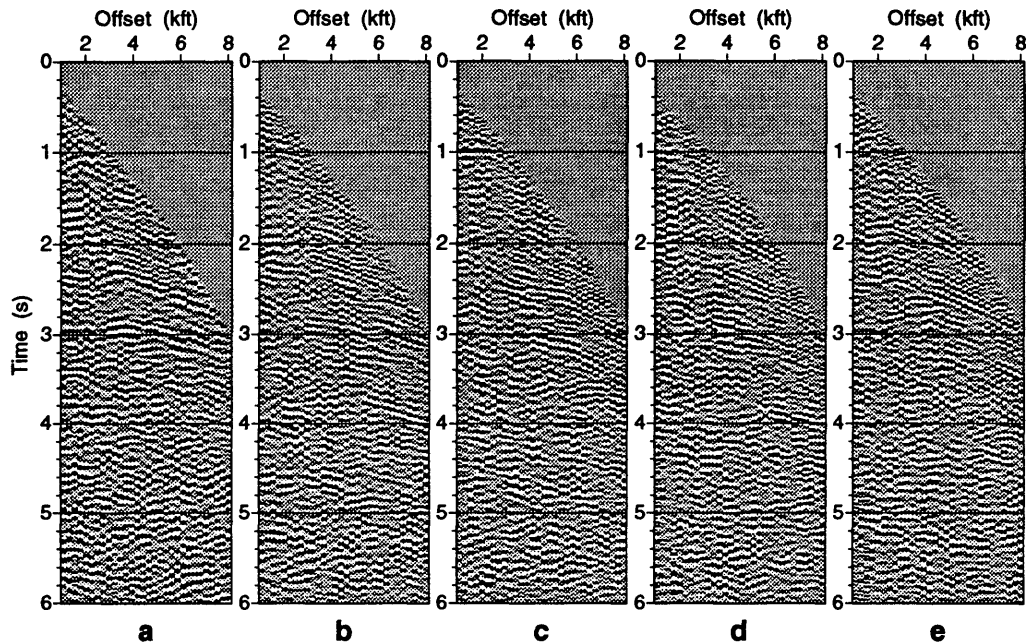


FIG. 5.5. Unstacked gathers corresponding to midpoint 275 of Line 1. The CMP gather with only preprocessing applied is shown in (a). CRP gathers, after undoing the NMO correction, are shown in (b), (c), (d), and (e), with velocity ratios 1.0, 0.6, 0.5, and 0.4, respectively.

constant-velocity stacks (results not shown).

Pleasing as it is to see the best continuity in the gathers produced by mode-converted TZO, one could ask whether that result is to be expected. From the synthetic data in Section 4.2, we saw that mode-converted TZO altered moveouts, but it did not actually change reflection continuity.

5.4.2 Quantitative analysis

To further support the qualitative assertion made above, that a velocity ratio $\gamma = 0.4\text{--}0.5$ is a reasonable choice, here I estimate the ratio based on measurements from the data.

Recall in Chapter 2, equation (2.11) gives an expression for zero-offset time. We start by splitting this relation into two parts, namely

$$\frac{\sigma^2}{\alpha h + \beta b} = a, \quad (5.1)$$

and

$$a = \frac{2h}{t^2} \left[\frac{t_0^2}{h^2 - b^2} + \left(\frac{2}{v_a} \right)^2 \right]. \quad (5.2)$$

Recall that σ , α , and β are quantities that depend on only the velocity ratio. The reason for the above splitting, as equation (5.2) implies, is to express a in terms of quantities that can be measured from seismic data (including the lateral shift b). With quantities b and a known, we can then solve for γ from equation (5.1). Solving for γ from that equation, and simplifying, we get

$$\gamma = \frac{a(h - b) - 1}{1 - \sqrt{2ah - a^2(h^2 - b^2)}}. \quad (5.3)$$

For simplicity here, we shall take v_a as the stacking velocity v_s , and t can be simply found from the expression

$$t^2 = t_0^2 + \frac{4h^2}{v_s^2}.$$

Also for simplicity, we shall assume near-horizontal reflectors, implying $b = 0$ for conventional p-waves. One check on the validity of relation (5.3) is to check it for the case of ordinary p-waves ($b = 0$). In such a case, a in equation (5.2) reduces to just $2/h$. Substituting $a = 2/h$ in equation (5.3) yields $\gamma = 1$, as expected for ordinary p-waves reflected from horizontal reflectors.

The quantity b can be estimated from two stacked sections shot in two different

directions, e.g., Lines 1 and 2 discussed earlier. We recall that the relative shift between the two sections at 4 s was 1800 ± 300 ft, corresponding to $b = 900 \pm 150$ ft (half the relative shift between the two sections). Since we are dealing with stacked data, the question now is: what value of half-offset h shall we use in the above relations? I choose to pick half the maximum h present in the data; i.e., $h = 2040$ ft—an average value that, I believe, is fairly representative of all half-offsets. As for velocity at 4 s between midpoints 248 and 215 (the vicinity of the shift under investigation), I choose a value of 4500 ft/s, a reasonable value as we shall see when I analyze velocities.

With the above assumptions, relation (5.2) yields the range $a = 0.00113$ – 0.00132 ft⁻¹. Equation (5.3) then gives the corresponding range of velocity ratio $\gamma = 0.41$ – 0.52 . A similar calculation at 2 s (peak of anticline at midpoint 180 in Line 1 shifts to midpoint 140 in Line 2) gives $a = 0.00126$ – 0.00159 ft⁻¹, and $\gamma = 0.40$ – 0.53 . Both ranges of velocity ratio are consistent with that ($\gamma = 0.4$ – 0.5) from the qualitative analysis.

From the above analysis, and since TZO is not too sensitive to the choice of velocity ratio, I choose $\gamma = 0.4$ in the TZO processing of the two data sets.

5.5 Application of TZO

I now apply TZO to both data sets assuming $\gamma = 0.4$. For comparison, I also show the same data processed with conventional TZO. The processing sequence for the stacked sections to come is as follows

1. NMO-correct preprocessed CMP gathers;
2. sort into common-offset gathers;

3. apply TZO;
4. sort into CMP gathers;
5. remove NMO correction (applied in Step 1) from data in Step 4;
6. perform velocity analysis;
7. use velocity function from Step 6 to NMO-correct and stack the data in Step 5.

Next, I show results of velocity analysis (Step 6), and compare them to their counterparts when TZO is not performed.

Figures 5.6 and 5.7 show stacks of TZO-corrected data for Lines 1 and 2, respectively, assuming $\gamma = 0.4$. Ideally, the two sections should display the same subsurface image, with no lateral shift of reflections. Let us compare these two sections to one another, and then compare each one to its counterpart when conventional processing (no TZO) is performed.

At first glance, it seems as though there is a prominent lateral shift of reflections between the two stacks on the left of the sections (midpoint 400) between 2 and 3 s (Figures 5.6 and 5.7). However, a closer look shows that this is not the case; instead the major difference here is that amplitudes of events on the left end of Line 1 are weaker than those in Line 2. This can be attributed to the fact that the two lines were shot in opposite directions, resulting in each line having a different (shifted) subsurface *coverage* at the left and right ends of the section. This also explains the weakened amplitudes seen on the right end of Line 2.

I have asked several colleagues to compare the two stacks on a workstation. Not knowing my personal bias, and not knowing how the data were processed, most of them confirmed that the major difference between the two sections was in their amplitudes, and not in their shifts. Elsewhere in the two sections, locations of events

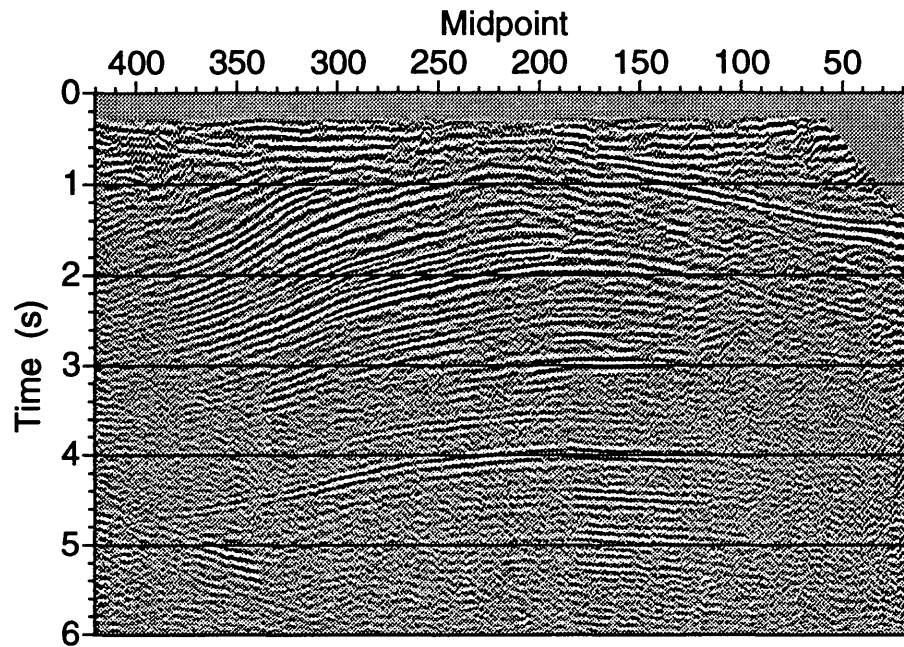


FIG. 5.6. Stack of TZO-corrected data of Line 1, assuming $\gamma = 0.4$.

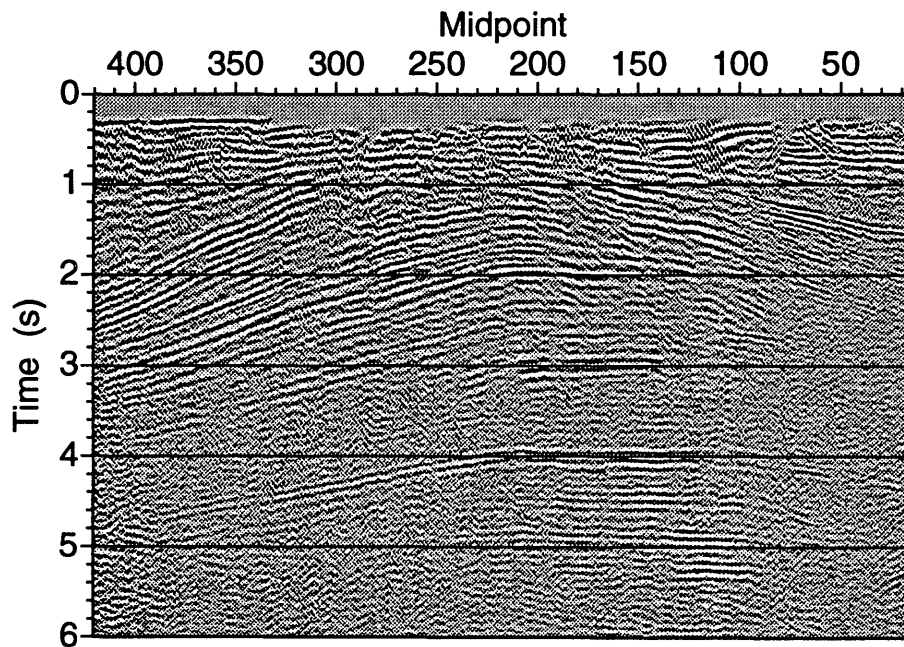


FIG. 5.7. Stack of TZO-corrected data of Line 2, assuming $\gamma = 0.4$.

generally match each other, although differences between the two sections are present (due to data quality and independently chosen stacking velocities). Take, for example, the anticline that intersects 4 s; in both sections, the intersection takes place at about midpoint 230. Another example is the anticline intersecting 2 s at midpoint 235 in both stacks.

We now compare the TZO-corrected stacks with conventional stacks for both lines. For Line 1, we note an improvement (flattening) of the dipping shallow reflector (Figure 5.6, midpoint 100, 1.2 s), as compared with its counterpart when conventional stack was used (Figure 5.1). Also, among other differences between the two stacks of Line 1, notice how the reflector at midpoint 175 and 3 s is smoother in the TZO-corrected section. In addition, dipping reflections below 5 s at midpoint 350 are present only in the TZO-corrected section. Note, also, that the reflections here have been shifted to the right; this is most prominent up shallow (compare, for example, the dipping reflections around 2 s between midpoints 350 and 400).

As expected for Line 2, the relative shift of events between the conventional stack (Figure 5.2) and the TZO-corrected stack (Figure 5.7) is opposite to that seen in the stacks of Line 1. That is, events in the TZO-corrected section are now shifted to the left, relative to those in the conventional stack. This opinion is shared, again, by colleagues with no knowledge as to how the data were processed. As for data quality, reflector continuity has improved on the left of the TZO-corrected section (between midpoints 350–400, 1.5–3 s). Meanwhile, data in the shallow part of the conventional stack have better quality than those in the TZO-corrected section.

For comparison, I show the same lines but now processed with conventional TZO ($\gamma = 1$). Figure 5.8 shows the stack of Line 1, and Figure 5.9 shows that of Line 2. The stack with conventional TZO for Line 1 (Figure 5.8) shows poorer reflectors

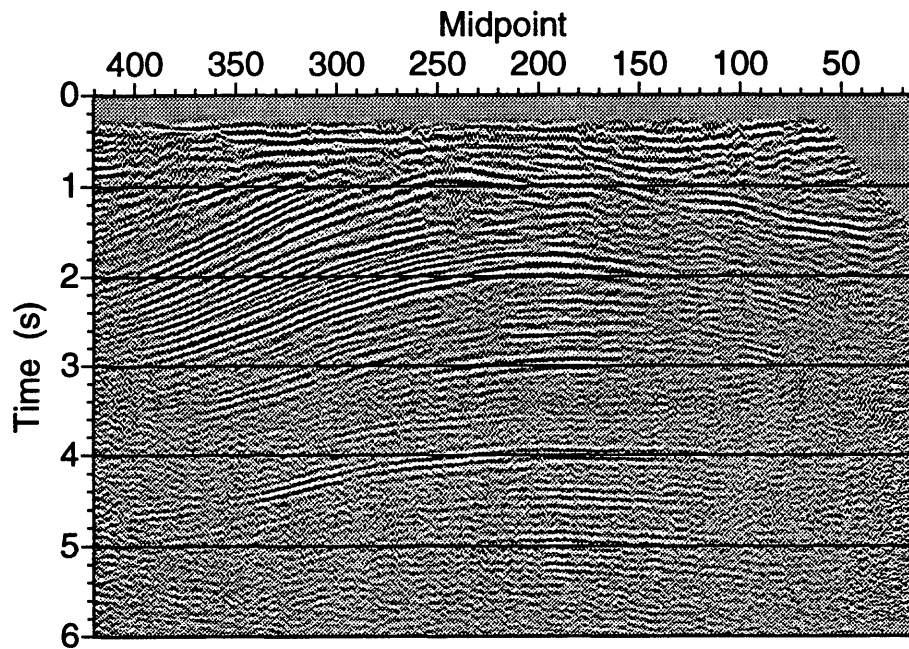


FIG. 5.8. Stack of TZO-corrected data of Line 1 assuming $\gamma = 1$ (no mode conversion).

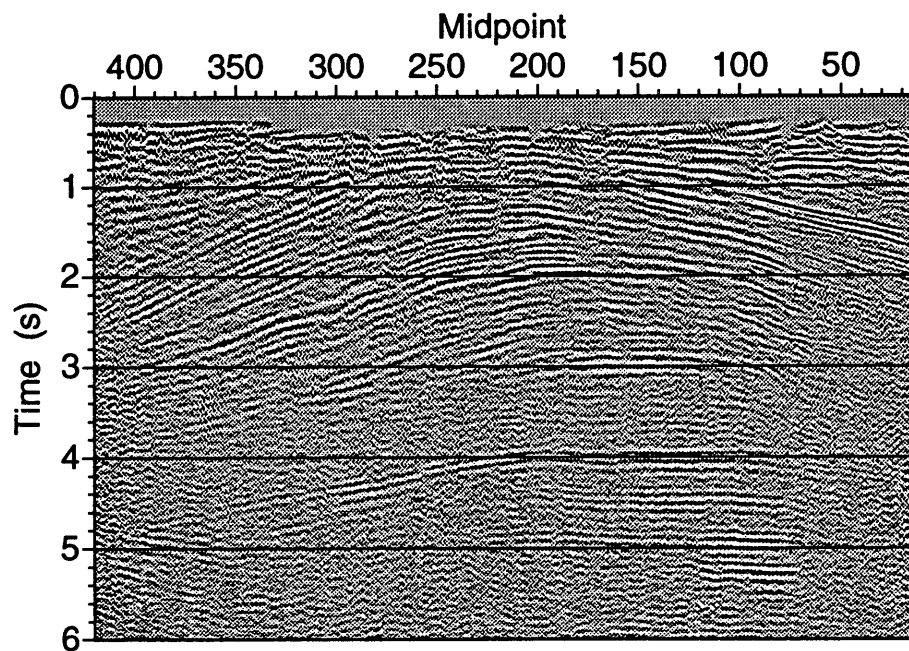


FIG. 5.9. Stack of TZO-corrected data of Line 2 assuming $\gamma = 1$ (no mode conversion).

continuity than when $\gamma = 0.4$ (Figure 5.6). For instance, compare the continuity of the reflector at midpoint 350 and 4.6 s in Figures 5.6 and 5.8. As for Line 2, the continuity of reflectors on the right of the section seems better in the stack with conventional TZO (Figure 5.9) than that with mode-converted TZO (Figure 5.7). However, data quality on the left of Line 2 is far superior with mode-converted TZO.

Unfortunately, but unsurprisingly, the data comparisons here are much less dramatic demonstrations of the effectiveness of mode-converted TZO than were the synthetic data examples. Given the sensitivity of any stack section to the choice of velocities for NMO correction, a look at the velocities used and the influence of velocity on these stacks may further help in assessment of the results.

5.6 Velocity analysis

We now look at stacking velocities for both lines, obtained before and after TZO has been applied. For data after TZO correction, I show stacking velocities for both mode-converted TZO and conventional TZO.

For Line 1, contours of stacking velocities, v_s , are shown in Figure 5.10. Note that the velocity values shown (4000–6000 ft/s) are obviously lower than those expected for ordinary p-waves; this is so because we are dealing with mode-converted waves with a relatively low velocity ratio ($\gamma = 0.4$). See Section 3.3 for more details.

The conventional stacking velocities (no TZO) are shown in Figure 5.10a. Note the general decrease in velocity from left to right. This velocity trend is consistent with observations that I discuss in Chapter 6—that not only does the stacking velocity for mode-converted waves depend on dip, but also on the sign of dip. More specifically, and as we shall see in Chapter 6, the stacking velocity *increases* when the shooting is updip from source to receivers; the increase is relative to when the reflector is

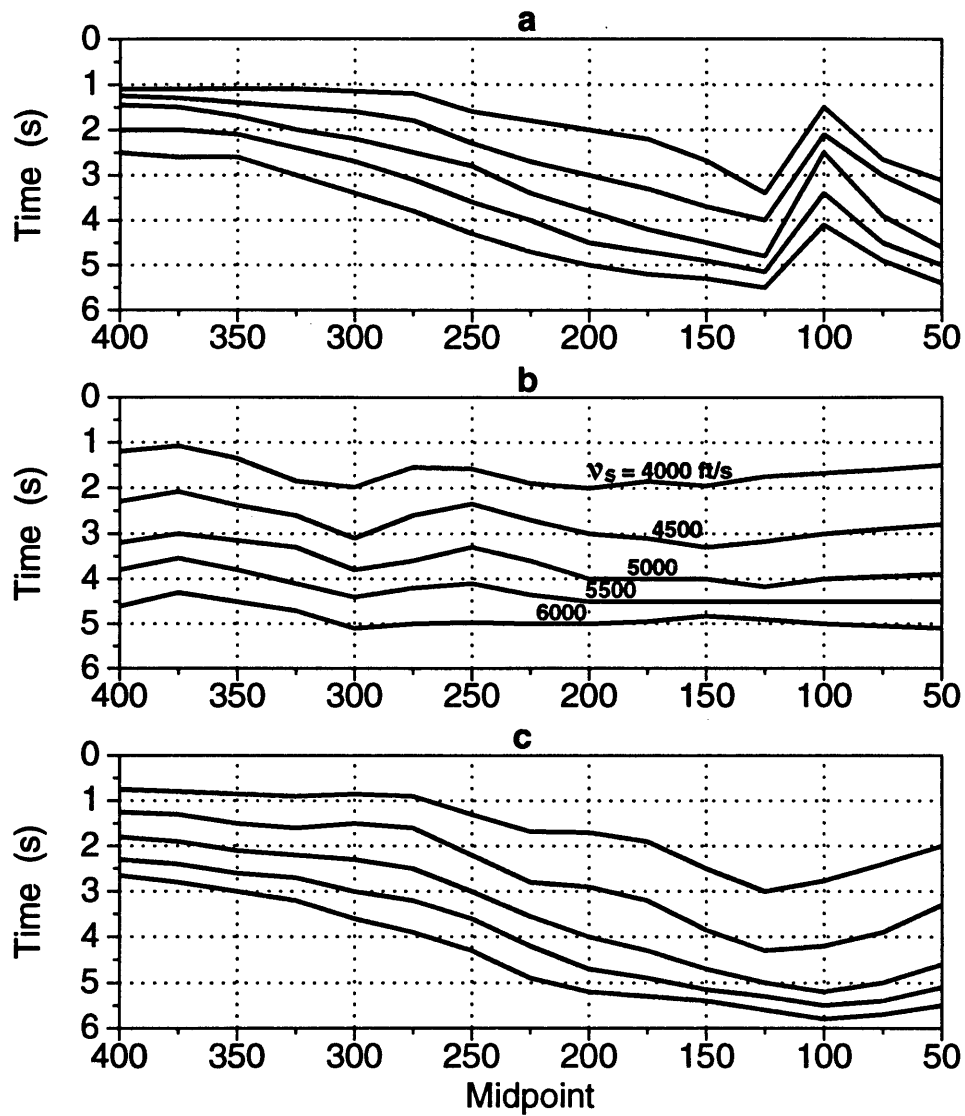


FIG. 5.10. Contours of stacking velocities for Line 1. (a) processing with no TZO; (b) mode-converted TZO; (c) conventional TZO.

horizontal. On the other hand, when the shooting is downdip, the stacking velocity *decreases*. (The stacking velocity for ordinary p-waves always increases with dip, regardless of the sign of dip.)

Recall that the shooting in Line 1 was from left to right. Given the anticlinal features present in the subsurface for this case, the shooting from left (midpoint 400) to right (midpoint 200) is then seen in the updip direction from source to receivers. Hence, the stacking velocity in this region (Figure 5.10a) is, as expected, relatively higher than that on the right portion of the section (midpoints 50–200) where shooting is now downdip.

The velocity contours for Line 1 after applying mode-converted TZO are shown in Figure 5.10b. Note that the velocities are consistent across the section, and are generally structure-independent. This indicates that mode-converted TZO has removed the influence of dip on stacking velocity, as one would hope.

For comparison, I show velocity contours for the same data but now processed with conventional TZO (Figure 5.10c). The general trend here is similar to that with no TZO (Figure 5.10a), implying that conventional TZO did not remove the dip influence from stacking velocity; this is not surprising. Since we are dealing with mode conversion, we should not expect conventional TZO (ignoring mode conversion) to correct mode-converted data as effectively as does mode-converted TZO.

As for Line 2, results of velocity contours are shown in Figure 5.11. The shooting geometry here is the reverse of that for Line 1. Hence, what was updip shooting for Line 1 is now downdip shooting here, and *visa versa*. As a result, the velocity trend in the conventional stack (Figure 5.11a) is now the reverse of that from Line 1 (Figure 5.10a). The velocities after mode-converted TZO has been applied are shown in Figure 5.11b. Clearly by comparing Figures 5.11a and 5.11b, mode-converted

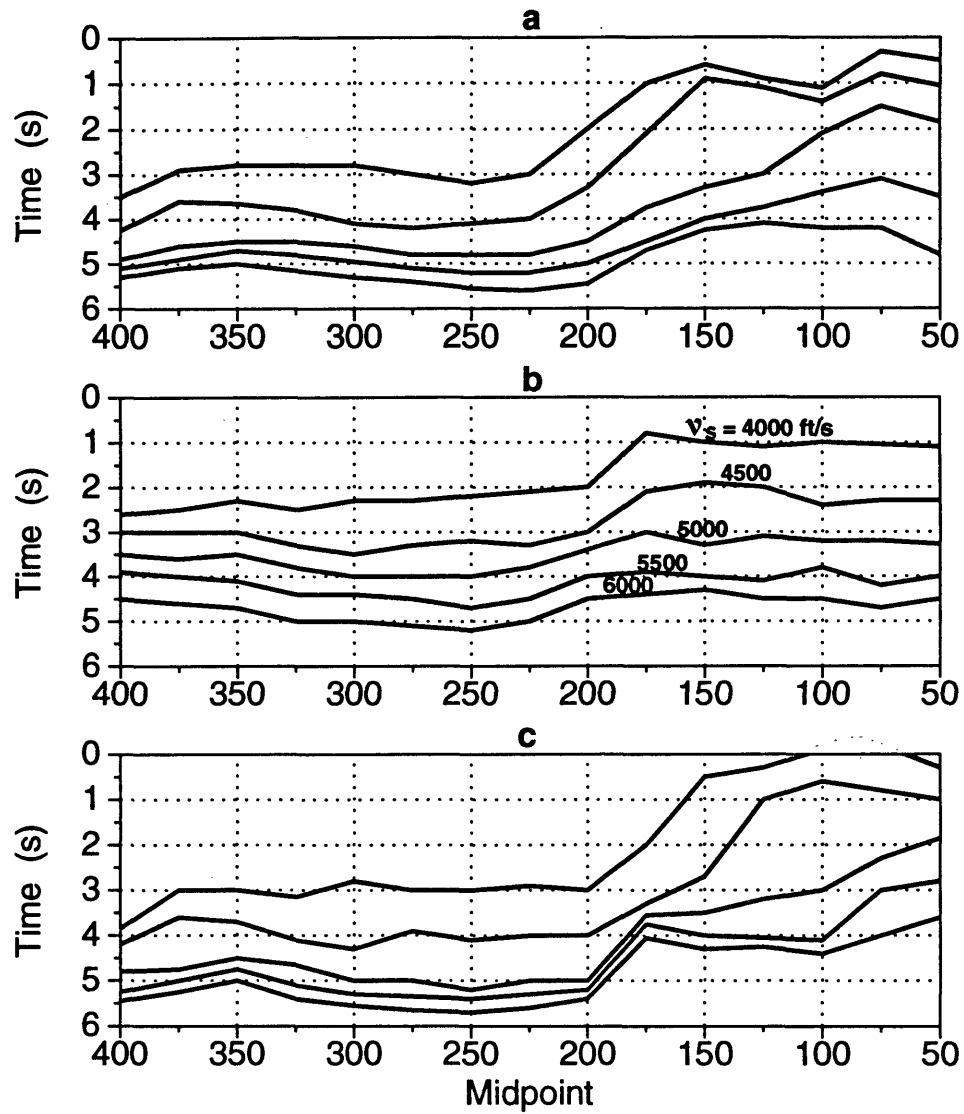


FIG. 5.11. Contours of stacking velocities for Line 2. (a) processing with no TZO; (b) mode-converted TZO; (c) conventional TZO.

TZO has significantly lessened the dip influence on stacking velocity. Velocities from conventional TZO are shown in Figure 5.11c; again, the trend here is similar to that with no TZO shown in Figure 5.11a.

The differences in stacking velocity seen in Figures 5.10 and 5.11 are significant in terms of their influence on the quality of the stacked data. To see this, Figure 5.12 shows a stack of conventional CMP gathers (Line 1), but the velocity function used to

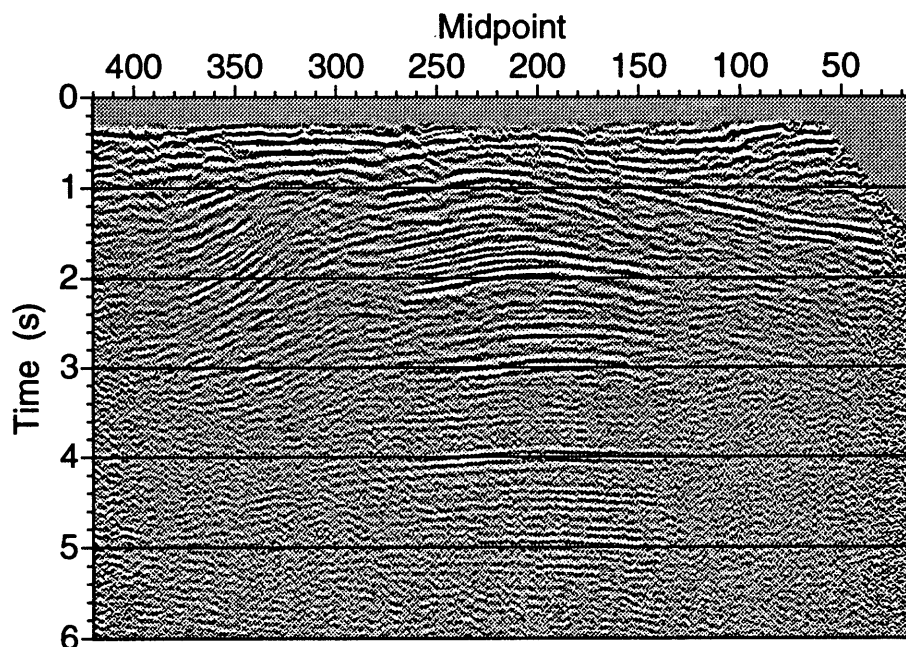


FIG. 5.12. Stack of conventional CMP gathers (Line 1), but using NMO velocity obtained after mode-converted TZO has been applied.

NMO-correct these data is that (Figure 5.10b) obtained after mode-converted TZO has been applied. The stack here is much poorer in reflection quality than either the TZO-corrected stack (Figure 5.6) or the conventional stack (Figure 5.1). The same observation holds for Line 2; the stack of conventional CMP gathers, using NMO velocity after mode-converted TZO has been applied (Figure 5.13) is much poorer than that in Figure 5.2.

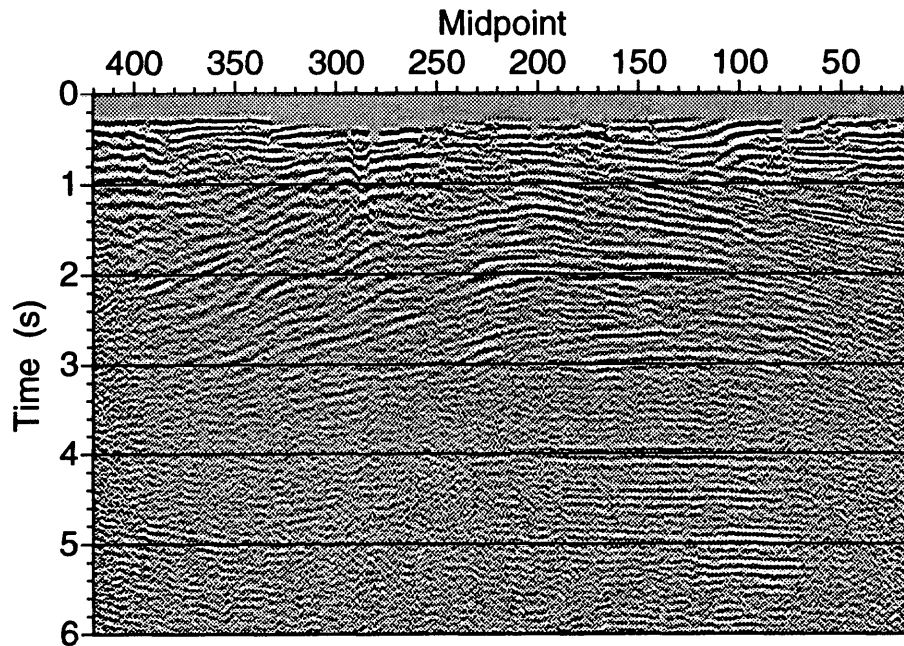


FIG. 5.13. Stack of conventional CMP gathers (Line 2), but using NMO velocity obtained after mode-converted TZO has been applied.

The central point in the “improper” stacks in Figures 5.12 and 5.13 is that the stack quality deteriorated when the rather stable, dip-independent NMO-correction velocities, as opposed to the dip-corrected velocities, were applied to the data. The conventional stacks were aided by the option to pick dip-dependent stacking velocity. That option would not have been available if the unmigrated data had contained crossing reflections having widely differing dips. We should not be surprised, therefore, that for these data, the mode-converted TZO, stacked data in Figures 5.6 and 5.7 were not dramatically superior to the conventionally stacked data in Figures 5.1 and 5.2.

I conclude from the analysis of the San Joaquin Valley data that, despite its poor signal quality and consequent difficulties in picking stacking velocities, and despite the fact that the data do not contain steep reflectors or conflicting slopes, the diagnostic results support the conclusion that mode-converted TZO yielded the best-processed

results, (results that are most consistent on the two reversed lines), and did so with stacking velocities that were essentially independent of dip.

Chapter 6

MODE-CONVERTED TZO IN THE k - t_1 DOMAIN

6.1 Introduction

In this chapter, we consider an alternative method for doing mode-converted TZO. The principles underlying the Gardner DMO approach (Forel and Gardner, 1988), which was originally developed for ordinary p-waves, are readily extended to mode-converted waves. The process achieves TZO in two steps. First, DMO correction is applied by simply transforming the prestack data into a new *nonphysical* offset-time domain. That is, the physical half-offset and recorded time, h and t , are transformed into new quantities, k and t_1 , having units of offset and time, respectively. Velocity analysis in the nonphysical domain yields a dip-independent average velocity as the velocity that best stacks the data. TZO is then achieved by applying NMO correction, using the average velocity, and finally stacking the gathers in the nonphysical domain.

Implementation of this TZO method, however, is deemed unfavorable due to three problems. In increasing order of severity, the problems are: amplitude and phase distortion, an amplitude-versus-offset (AVO) problem, and a large-offset problem. The problem of amplitude and phase distortion seems unsolvable for mode-converted waves when using this TZO method. In addition, neither the AVO nor the large-offset problems can be overcome, even when dealing only with ordinary p-waves.

Despite these problems, useful information can still be obtained from this TZO

method. Brute zero-offset sections, with coarse treatment of amplitudes, can be generated. Also average velocities, for converted-wave reflections, can be obtained from conventional velocity analysis performed on gathers in the nonphysical domain. The average velocity, so-determined, is useful in exploration applications such as migration and conversion from time to depth.

In the following, we derive TZO for mode-converted waves in the nonphysical domain, showing that it is a special case of Gardner DMO, which was developed for ordinary p-waves. We then present a detailed analysis of the problems associated with this TZO method.

6.2 The k - t_1 TZO method

TZO for mode-converted waves is achieved here in two steps. First, the seismic data are corrected for DMO; second, NMO correction is applied to the data. The first TZO step, i.e., DMO correction, is independent of velocity. This indeed was the primary rationale for Gardner's development of the method. DMO correction is automatically applied to the data by transforming the recorded seismic data from the physical (offset-time) domain into a nonphysical domain, Gardner's k - t_1 domain.

To transform the data to the k - t_1 domain, consider a seismic trace whose half-offset between source and receiver is h and whose recorded time is t . Ignoring the fact that there is no mode conversion at zero-offset, as before, b denotes the position, relative to the midpoint, of an equivalent zero-offset trace, as shown in Figure 6.1. An expression for the square of the zero-offset time, t_0^2 , was given in equation (2.11), which we rewrite here as

$$\frac{\sigma^2(h^2 - b^2)}{2h(\alpha h + \beta b)} t^2 = t_0^2 + \frac{4(h^2 - b^2)}{v_a^2}, \quad (6.1)$$

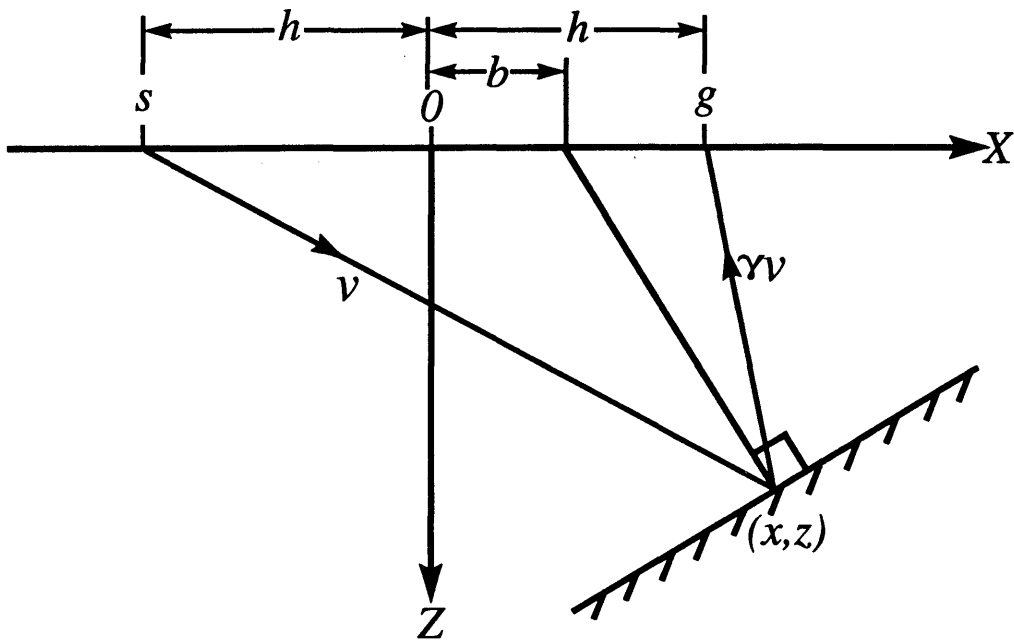


FIG. 6.1. Depth section depicting mode-converted reflection. Here, $2h$ is the offset distance between source s and receiver g . The midpoint is located at the surface point $x = 0$. The downgoing and the upgoing velocities are, respectively, v and γv . The equivalent zero-offset trace, for this geometry, is located a distance b from the midpoint.

where we recall from Section 2.2 that α , β , and σ are constants depending only on the velocity ratio. Equation (6.1) can be written as

$$t_1^2 = t_0^2 + \left(\frac{2k}{v_a} \right)^2, \quad (6.2)$$

where the new "offset" k is defined by

$$k^2 \equiv h^2 - b^2, \quad (6.3)$$

and the new time is

$$t_1 \equiv \frac{\sigma k}{\sqrt{2h(\alpha h + \beta b)}} t. \quad (6.4)$$

The quantity k is the same offset-dependent parameter obtained by Forel and Gardner for ordinary waves. The newly defined time t_1 is a scaled version of the recorded time t . For $\gamma = 1$ (e.g., ordinary p-waves), the scaling factor reduces to k/h , the same factor derived by Forel and Gardner. Note, also, that the mapping given by equation (6.4) is a function of the velocity *ratio*, γ , but not of the individual p- and s-waves velocities themselves. We use equations (6.3) and (6.4) to transform the physical quantities, h and t , into their nonphysical counterparts, k and t_1 , respectively.

The transformation automatically DMO-corrects the data. That is, in terms of the transformed offset k and the transformed time t_1 , equation (6.2) is seen to be just a simple hyperbolic time-offset relationship (i.e., standard NMO equation) for mode-converted waves. It maps nonzero-offset data at transformed time t_1 to zero-offset time t_0 . Moreover, just as for ordinary waves, by equation (2.9) the moveout velocity v_a in equation (6.2) is independent of dip, one of the primary goals in transforming data to zero offset. Furthermore, as shown in Figure 6.1, after TZO the zero-offset data and the recorded nonzero-offset data pertain to a *common reflection point*. That is, TZO has removed the problem of reflection-point dispersal (Deregowski, 1986) for mode-converted data, just as it does for ordinary-wave data. In addition, recall that for ordinary p-wave data, reflection-point dispersal is not an issue when the reflector is horizontal. For mode-converted data, however, it is. TZO, as described here, removes reflection-point dispersal for mode-converted data when the reflector is horizontal, as well as when it has dip.

Having applied DMO correction by simply transforming the data to the k - t_1 domain, TZO can now be completed by applying NMO correction to the data. As

equation (6.2) implies, conventional velocity analysis in the $k-t_1$ domain yields the dip-independent average velocity, v_a , as the velocity that best stacks the data. Consequently, the data can be stacked, after NMO correction, to yield reflections at their true zero-offset times.

6.3 Problems with the $k-t_1$ TZO method

6.3.1 Amplitude and phase distortion

Although the theory holds from the kinematics point of view, implementation of this $k-t_1$ TZO method does not treat amplitude and phase properly. Figure 6.2b shows an output $k-t_1$ gather. The input data consist of 101 synthetic common-

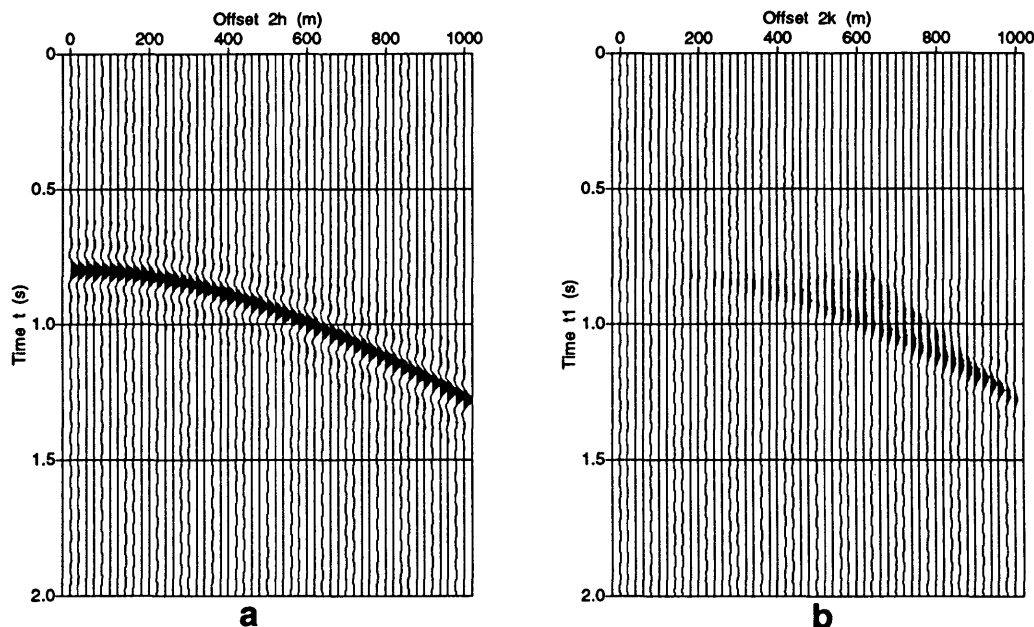


FIG. 6.2. (a) representative synthetic CMP gather over a horizontal reflector at 400-m depth. (b) output $k-t_1$ gather, with severely distorted amplitude and phase. The input data are ordinary p-wave ($\gamma = 1$) synthetic CMP gathers, and the medium velocity is 1000 m/s.

midpoint (CMP) gathers over a single horizontal reflector. Only ordinary p-waves are considered in this example, i.e., $\gamma = 1$. The input wavelet is a sinc function, with unit amplitude and a dominant frequency of 12.5 Hz (a low frequency is assumed here to emphasize the shape of the output wavelet). Each input CMP gather consists of 51 traces (including the zero-offset trace), with an increment in source-receiver separation distance of 20 m. The distance separating two consecutive CMP gathers is 10 m. For this horizontal-reflector model, all input CMP gathers are identical; one such gather is shown in Figure 6.2a. The location of the output $k-t_1$ gather is at CMP location 51, midway along the line. All 101 CMP gathers contribute equally, without any special weighting, to the output $k-t_1$ gather shown in Figure 6.2b.

For such a trivial model as this, the data in the $k-t_1$ domain ideally would be unchanged from any one of the input CMP gathers. The $k-t_1$ result depicted in Figure 6.2b clearly shows an increase in amplitude with offset (with the exception of the last few traces). The maximum amplitude (offset ≈ 900 m) is about 40 times larger than the input unit amplitude (the zero-offset trace). The variation in amplitude is related to changing Fresnel-zone width as a function of k and t_1 . The Fresnel-zone width for this model (Appendix E) is shown in Figure 6.3 for different values of k . For the range of k values shown in Figure 6.3a, the Fresnel-zone width, and therefore the amplitude, increases as k increases across the time window of interest (0.8—1.25 s). Figure 6.3b shows the Fresnel zone for another range of k 's, this time the large k 's. Consistent with the observation that amplitude starts to decrease with increasing k in this offset range (starting at offset $2k \approx 900$ m in Figure 6.2b), the Fresnel-zone width also decreases with increasing k .

Compared with the zero-phase input wavelet in Figure 6.2a, the wavelet in the output $k-t_1$ gather has undergone a significant amplitude and phase distortion that

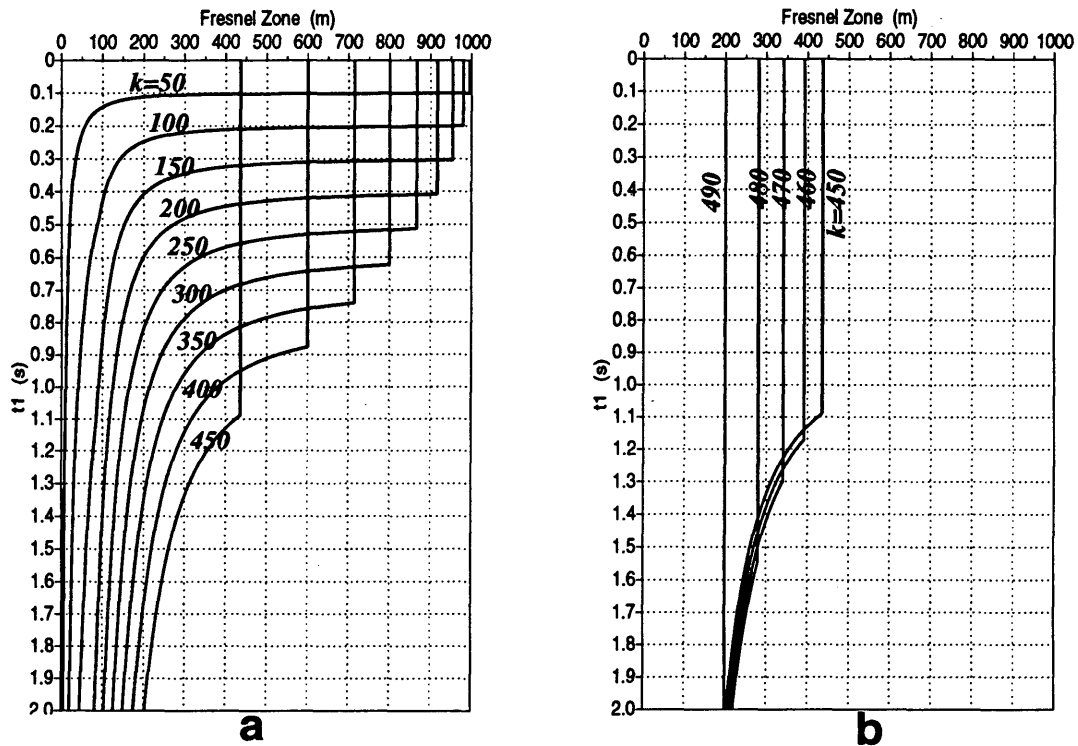


FIG. 6.3. Fresnel-zone width for the k - t_1 gather depicted in Figure 6.2b. The Fresnel zone increases with increasing k in the time window 0.8 – 1.25 s for the range of k shown in (a). In (b), the Fresnel-zone width decreases as k (large) increases for the same time window. Corners seen on the curves are explained in Appendix E.

varies with time and offset. The distortion is worst at offset $2k \approx 600$ m, where the wavelet contains a low-frequency precursor. To see how this distortion takes place, first note again that each output trace gets contributions from many midpoints and many offsets. In fact, any offset-midpoint combination satisfying equation (6.3) will contribute to this single, constant-offset ($2k$) output trace in the k - t_1 domain. Furthermore, the number of physical traces, contributing to a single k - t_1 trace, varies as a function of k and t_1 . The final k - t_1 trace is a result of stacking the contributions from all possible traces in the h - t domain. In other words, each output trace is a mixture of traces from different offsets and midpoints.

Figure 6.4 shows the contributions from all possible midpoints, before stack, to the $k-t_1$ trace whose offset, in Figure 6.2b, is 600 m. In this figure, it is clear that

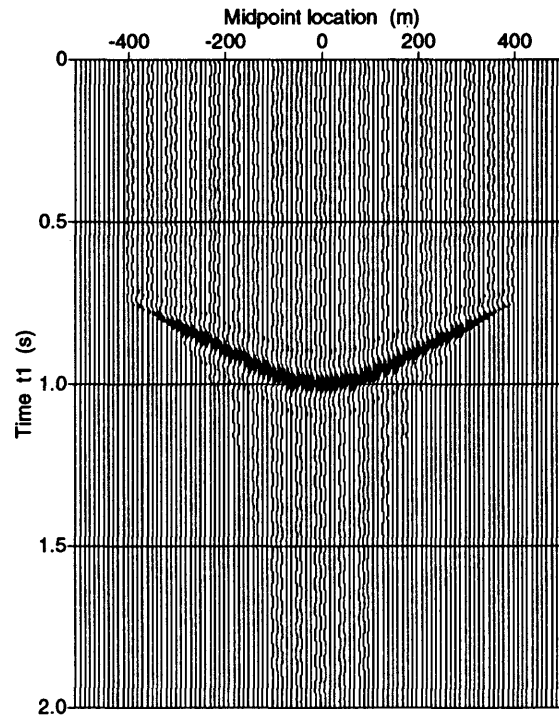


FIG. 6.4. Contributions from many midpoints to a single output trace in the $k-t_1$ domain. In this example, the stack of this gather forms the trace whose offset is 600 m in Figure 6.2b. The locations of contributing midpoints are relative to the location of the output $k-t_1$ gather.

the stacked trace will eventually have an amplitude that depends on the width of the Fresnel zone for the event. Besides, stacking the curved event (smile) in that figure introduces a rho-filtering of the input wavelet (Newman, 1990), and gives rise to the precursor seen in the final stacked trace. Due to the complexity arising with the kinematics of mode conversion, an analytic description of those smiles is not available when $\gamma \neq 1$ (even for horizontal reflectors) and, therefore, an inverse rho-filter cannot be readily designed. For ordinary p-waves, the analytic expression describing such

smiles depends, among other things, on dip. Consequently, when generating a k trace, an expression for the Fresnel-zone width derived assuming some dip, will be correct for only that dip. The Fresnel-zone widths shown in Figure 6.3 were obtained assuming a horizontal reflector. Widths based on this assumption (Appendix E) are later used to balance amplitudes in $k-t_1$ gathers.

Aside from the amplitude and phase distortion, as the theory predicts, the event in the $k-t_1$ gather of Figure 6.2b is approximately hyperbolic, with a moveout velocity equal to that of the medium. This is shown by applying a constant-velocity (1000 m/s) NMO correction to the synthetic gather of Figure 6.2b. The result, depicted in Figure 6.5, shows that the main energy of the (distorted) event is now flattened.

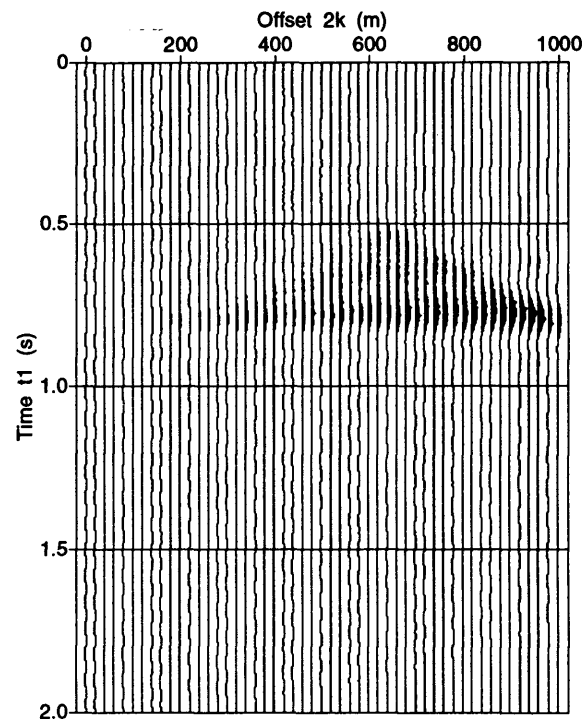


FIG. 6.5. The $k-t_1$ gather of Figure 6.2b is flattened after applying a constant-velocity NMO correction to the data. The velocity used is the medium velocity, 1000 m/s.

For ordinary p-waves, Forel (1986) avoided this amplitude and phase problem completely by not transforming the data to the $k-t_1$ domain. Instead, he selected a different method for implementing DMO—the constant-velocity-migration approach outlined by Ottolini (1982). Forel and Gardner (1988), however, did apply the $k-t_1$ TZO implementation to ordinary p-wave, 3-D synthetic data. They observed, just as I have shown for the 2-D case, that the amplitude and phase had undergone a distortion that varied with time and offset, although the kinematics (timing of events) were correct.

6.3.2 The AVO problem

It is only when b is zero that the new offset k is the same as the physical offset h , as equation (6.3) shows. This condition (i.e., $b = 0$) is always true only for horizontal reflectors with no mode-converted waves, in which case TZO is not even needed. In general, however, k and h are not the same; for mode-converted waves, they differ even when the reflector is horizontal. Even when k and h are the same, the final $k-t_1$ trace is always a mixture of traces from different offsets and different midpoints. This drawback certainly makes AVO analysis in the $k-t_1$ domain meaningless. Stated differently, the $k-t_1$ approach to TZO is seen as a device for obtaining a good approximation to a zero-offset trace after stacking, not for producing improved unstacked traces. We shall see, nevertheless, that velocity analysis is aided by the transformation to the $k-t_1$ domain.

6.3.3 The large-offset problem

Further investigation of equation (6.3) reveals yet another problem intrinsic to the $k-t_1$ domain—one that arises for large offsets $2k$. Large- k traces cannot be cor-

rectly constructed in most cases. The half-offset k is considered large when its value is comparable to the largest physical half-offset, h , in question.

The relationship between the physical and the nonphysical offsets, given in equation (6.3), is schematically shown in Figure 6.6. In that figure, each circle, whose

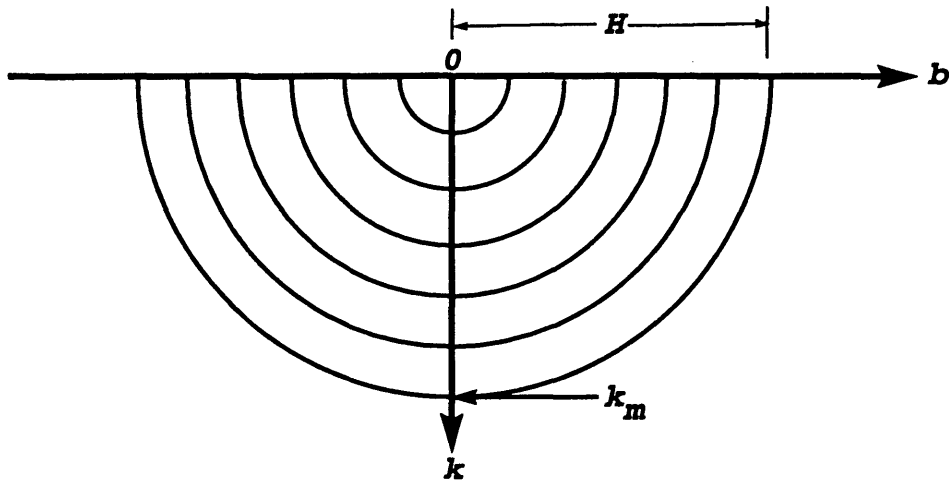


FIG. 6.6. Schematic diagram showing the relationship between the physical and the nonphysical half-offsets as given in equation (6.3). Here, circles represent constant, physical half-offsets. The maximum physical and nonphysical half-offsets are H and k_m , respectively.

radius is equal to a constant physical half-offset h , shows the relationship between k and b . The largest circle has a radius H , corresponding to the maximum physical half-offset in question. As k increases, larger circles, and hence larger physical offsets, are involved; this, in turn, limits the values allowed for b to progressively smaller ranges in constructing k traces. In the extreme case, when the nonphysical half-offset is maximum k_m and is equal to H , only one value for b ($b = 0$) is allowed.

For horizontal reflectors with no mode conversion (the case when b is really zero), there should be no problem with generating traces with large k 's. Figure 6.2b

is an example of this case. For dipping reflectors (with or without mode conversion), however, large- k traces will always be erroneous. That is, the time t_1 will depart from the hyperbolic trajectory given by equation (6.2). For mode-converted waves, large- k traces will always be also erroneous even for horizontal reflectors. The reason for the error in these two cases is simply that the actual b , in the corresponding physical seismic traces, is never zero, whereas only small values for b are used (allowed) in the process of generating the k trace.

Synthetic k - t_1 gathers from different models, Figure 6.7, show the problem encountered with the large- k traces. To minimize the amplitude variations from trace to trace, each trace has had a gain (based on the Fresnel-zone width, as discussed earlier and in Appendix E) applied to it as a function of k and t_1 . For all these k - t_1 gathers in Figure 6.7, the input data consist of 101 CMP gathers synthesized over a reflector whose depth is 400 m; the largest offset ($2h$) is 1000 m. The medium velocity is 1000 m/s, and the input wavelet is zero phase with unit amplitude. The reflector in gather (a) is horizontal, with only ordinary p-waves. Since the actual b is exactly zero for this model, the event is hyperbolic as expected—no kinematics problems arise with the large- k traces. Gather (b) is the same as (a), but now the reflector dips at 20° downward from source to receiver; note the nonhyperbolic behavior of the event in the large-offset traces. Gathers (c) and (d) show the case when dealing with mode-converted waves (downgoing velocity = 1000 m/s, $\gamma = 0.5$) for a horizontal and a dipping reflector, respectively. Events in the large-offset traces, of gathers (c) and (d), weaken and clearly follow a nonhyperbolic path, confirming the existence of the problem with the kinematics for large values of k .

In generating a k trace, contributions from different midpoints (i.e., from a range of b values) are stacked. Figure 6.4 is an example of the contributing traces before they

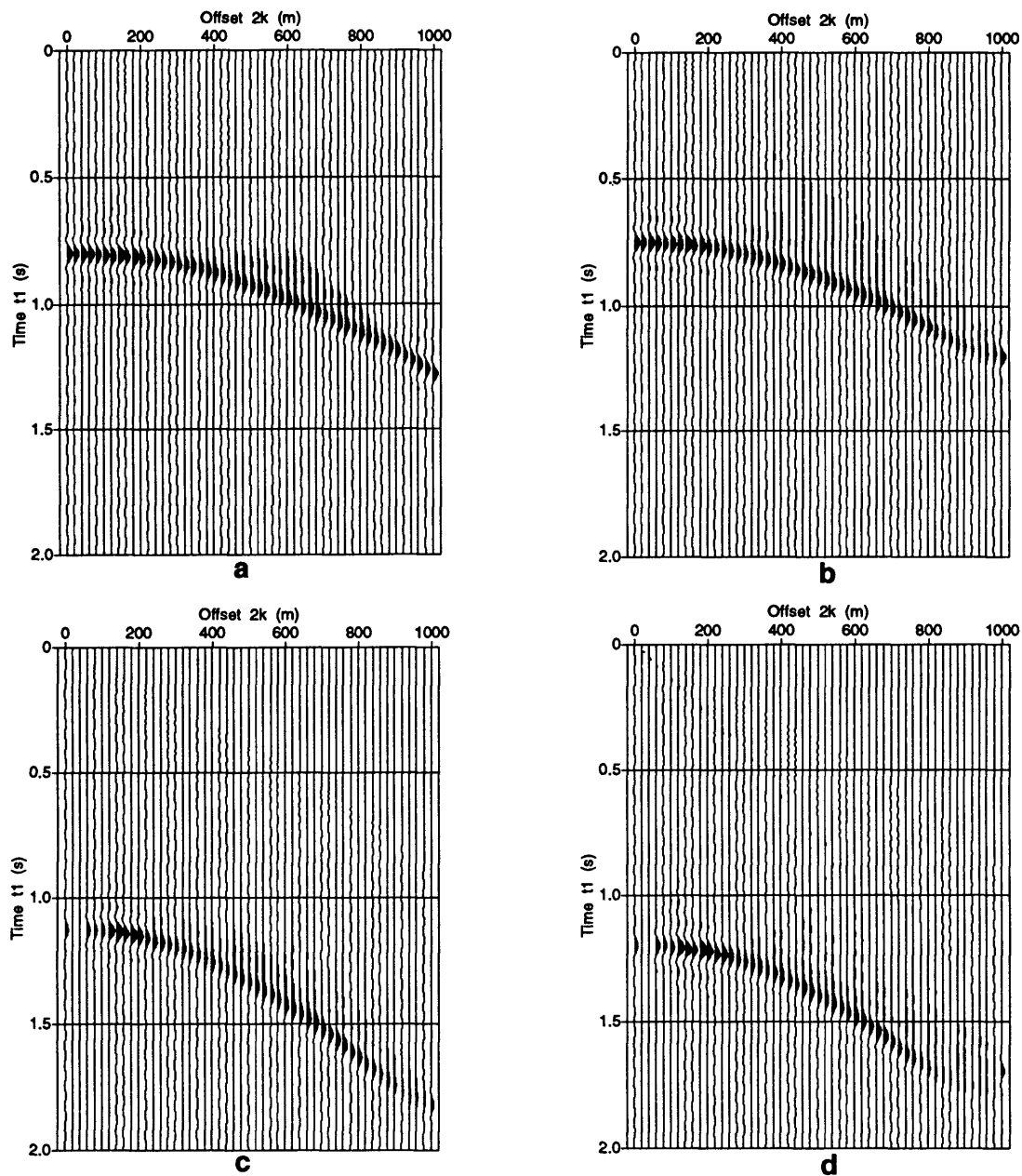


FIG. 6.7. The problem with large- k traces. The event in (a) is hyperbolic for all k values because the reflector is horizontal with no mode-converted waves. When the reflector is dipping, or when mode conversion is present, large- k traces become erroneous (i.e., nonhyperbolic), as depicted in (b), (c), and (d). In (b), the reflector dips at 20° downward from source to receiver. Events in (c) and (d) show the problem for mode-converted waves; the reflector in (c) is horizontal, whereas that in (d) dips at 20° downward from source to receiver.

are stacked. For each k trace, the theoretical b range (Appendix F) may or may not be totally included within the available range calculated based on equation (6.3). In other words, large- k traces typically require large- h traces, which in turn may not have been recorded, especially when b is large. When generating a k -trace, reflections from contributing midpoints, before stack, typically form a ‘smile’ in the k - t_1 domain. The maximum time t_1 along a smile is attributed to a midpoint that really pertains to the same reflection point as that dictated by b . That is, the appropriate midpoint (the one giving rise to the actual b value in question) yields the maximum t_1 along a smile. The stack of the smile will ultimately have its timing close to that of the maximum t_1 of the smile (Appendix G). As long as the b range, used in generating a k trace, encompasses the actual b associated with this k trace, the moveout of the corresponding k -trace (after stack) will be hyperbolic, in accordance with equation (6.2).

As an example, the smile in Figure 6.4 peaks when the midpoint location is equal to zero; this corresponds to the actual value for b in that model, for a horizontal reflector with no mode conversion. In general, the extent to which an event in a k trace (after stack) will follow a hyperbolic trajectory in a k - t_1 gather depends on whether or not the actual value of b for that trace is within the range of b values used in generating the k trace itself; the actual b value for each k trace, however, is a complicated function of dip, depth, and velocity ratio (Appendix G).

6.4 Alternative solution

Despite the problems associated with the k - t_1 TZO method, some useful information may still come out of use of this method. When amplitude is not of concern, for example, one can use the k - t_1 approach to generate a zero-offset section for mode-converted waves. Of course, the zero-offset section will then have distorted

amplitudes. The k - t_1 method can nevertheless be used to deduce velocity information when dealing with mode-converted waves.

As equation (6.2) implies, velocity analysis in the k - t_1 domain yields the average velocity, v_a , as the velocity that will best stack the data. Again, although the velocity ratio γ is required to do the transformation to the k - t_1 domain, actual velocity is not. With the average velocity determined, TZO by some alternative method (e.g., Harrison, 1990, or the frequency-wavenumber domain approach proposed earlier) can then be used. As we recall, equation (2.11),

$$t_0^2 = (h^2 - b^2) \left[\frac{(\sigma t)^2}{2h(\alpha h + \beta b)} - \left(\frac{2}{v_a} \right)^2 \right],$$

shows that the average velocity can be used to directly transform the prestack seismic data from recorded time t to zero-offset time t_0 .

6.5 Velocity estimation

We now perform velocity analysis for p-sv mode conversion in three models: one with a horizontal reflector and two with reflectors dipping at 25° downward and upward (from source to receiver), respectively. The parameters for all these models are such that all have the same zero-offset time (0.95 s) at the location where velocity analysis is performed. The dominant frequency of the input zero-phase wavelet is 12.5 Hz (this low frequency is again chosen to emphasize the shape of the output wavelet; higher frequencies yield similar results). The downgoing velocity is 2000 m/s, and a $\gamma = 0.5$ is chosen, yielding an average velocity $v_a = 1333$ m/s, based on equation (2.9). For comparison, velocity analysis was performed in both the h - t and k - t_1 domains.

For the reflector dipping at 25° downward, the results from the k - t_1 domain

approach are shown in Figure 6.8. Figure 6.8a shows the output $k-t_1$ gather, whereas Figure 6.8b shows the same gather after applying a low-cut (3 Hz) filter. The filter was applied to suppress the near-DC precursors that arise in the transformation to the $k-t_1$ domain. Because of the problem with the large- k traces, as discussed earlier, the last few traces were muted before doing the velocity analysis. The stacking velocity for this event is found to be 1370 m/s, which is close to the average velocity (1333 m/s). The NMO-corrected $k-t_1$ gather is shown in (c) in that figure, and the stacked (zero-offset) trace is shown in (d). Note that the peak of the stacked trace is at 0.95 s, the correct zero-offset time.

A conventional CMP gather, at the same location as that of the above $k-t_1$ gather, is shown in Figure 6.9a. Velocity analysis on this gather yields an erroneous stacking velocity of 1200 m/s, 10 percent *lower* than the average velocity. This low value in stacking velocity clearly cannot be attributed to the familiar $\cos \theta$ dip-correction factor. The NMO-corrected gather is shown in (b), and the stacked trace, shown in (c), shows that the event is now 20 ms later than the expected zero-offset time. Note, however, the stacked $k-t_1$ wavelet in Figure 6.8d is not as close to being zero-phase (input wavelet) as that of the $h-t$ wavelet in Figure 6.9c; the quality degradation in the $k-t_1$ wavelet is due to improper phase treatment (rho-filtering).

For the horizontal reflector, the results of the analysis in the $k-t_1$ domain and the $h-t$ domain are shown in Figures 6.10 and 6.11, respectively. The stacking velocity obtained in the $k-t_1$ domain (1350 m/s) is practically the same as the average velocity, whereas that obtained in the $h-t$ domain (1480 m/s) is 11 percent higher than the average velocity. The timing of the event did not differ much from the true zero-offset time in either case.

For the reflector that is dipping at 25° upward, the results are shown in Fig-

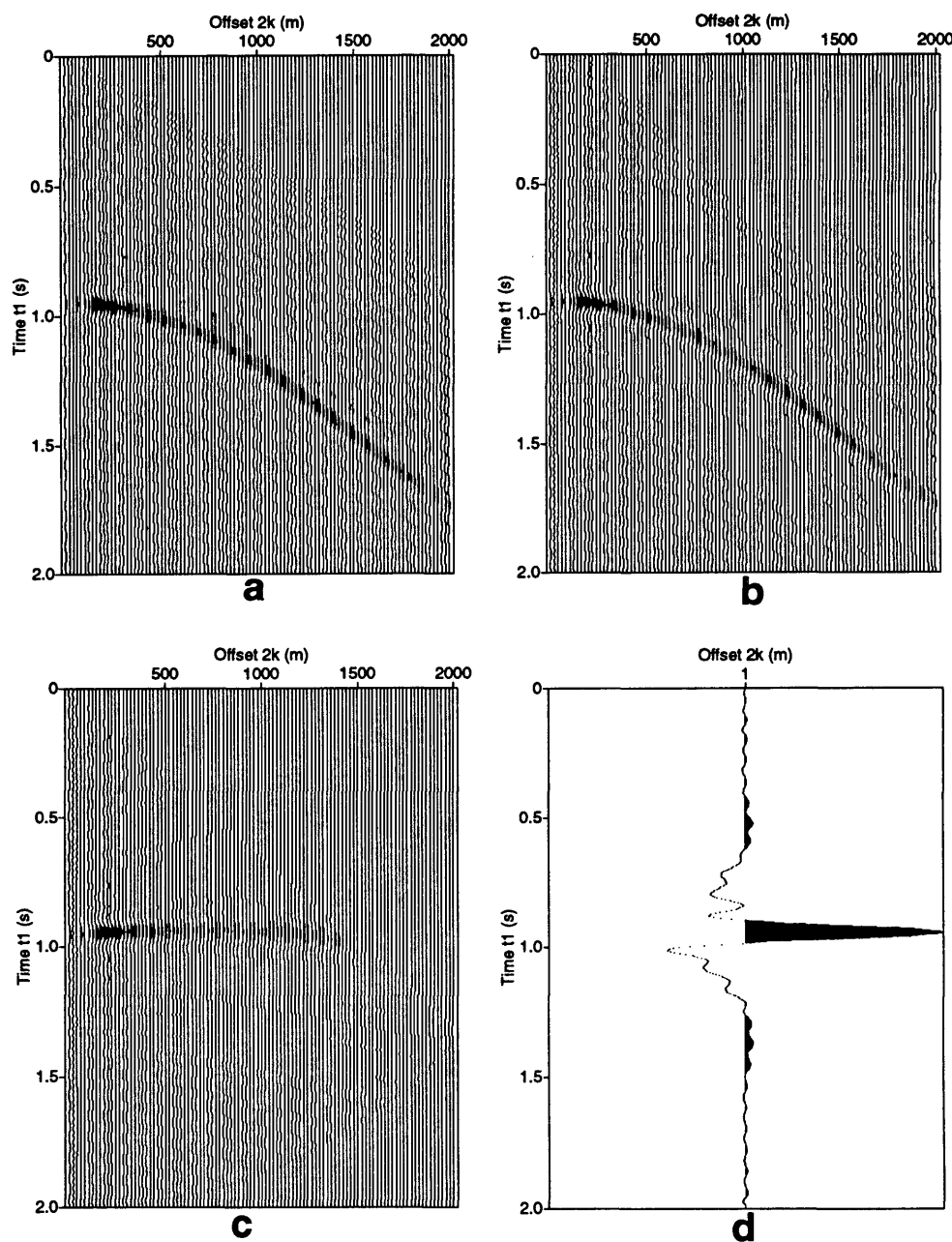


FIG. 6.8. Analysis in the $k-t_1$ domain for a reflector dipping at 25° , downward from source to receiver. (a) output $k-t_1$ gather; (b) same gather after filtering; (c) NMO-corrected gather ($v = 1370$ m/s); (d) stacked trace.

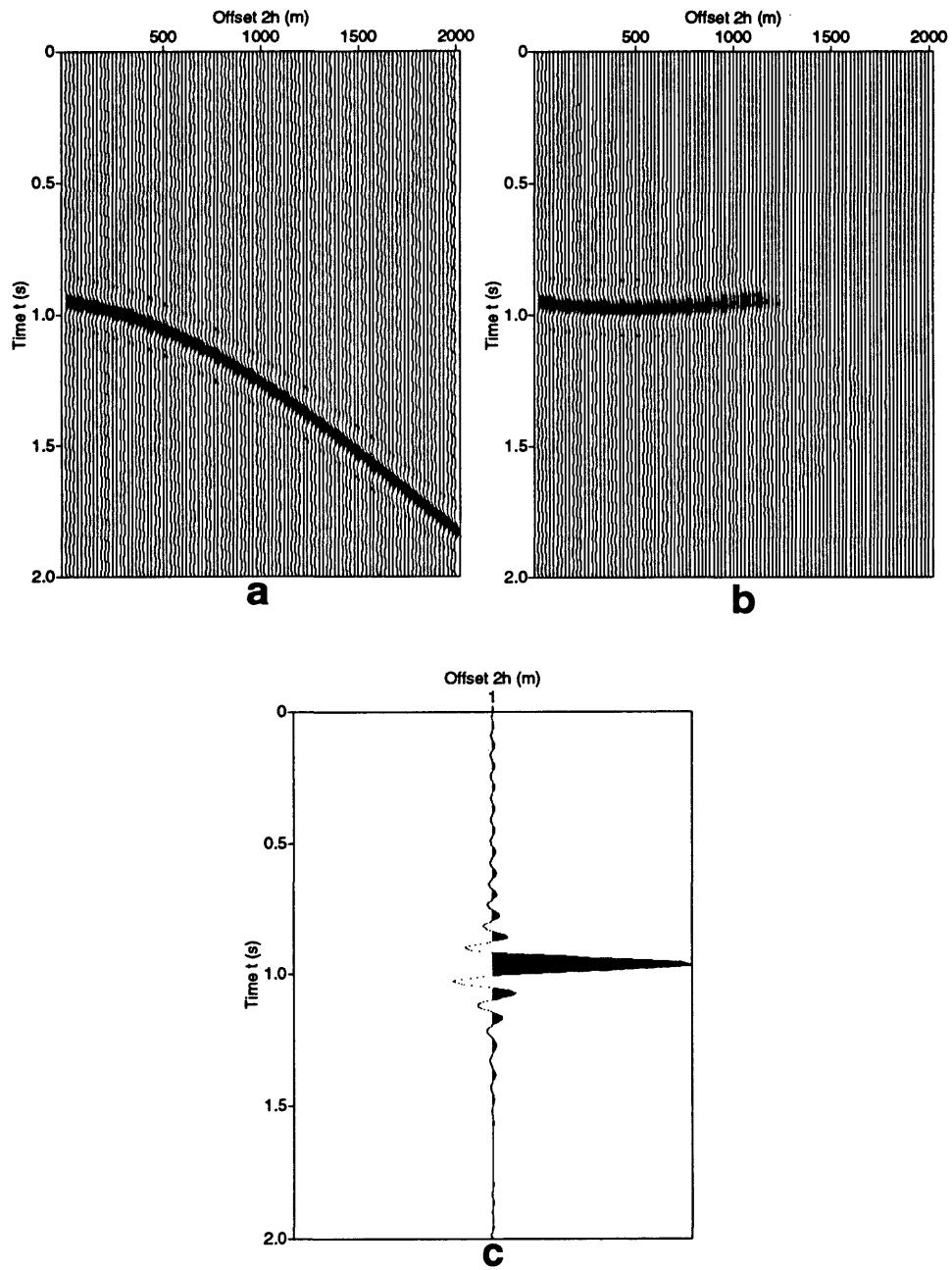


FIG. 6.9. Analysis in the $h-t$ domain for a reflector dipping at 25° , downward from source to receiver. (a) CMP gather at the location where velocity is analyzed; (b) NMO-corrected gather ($v = 1200$ m/s); (c) stacked trace.

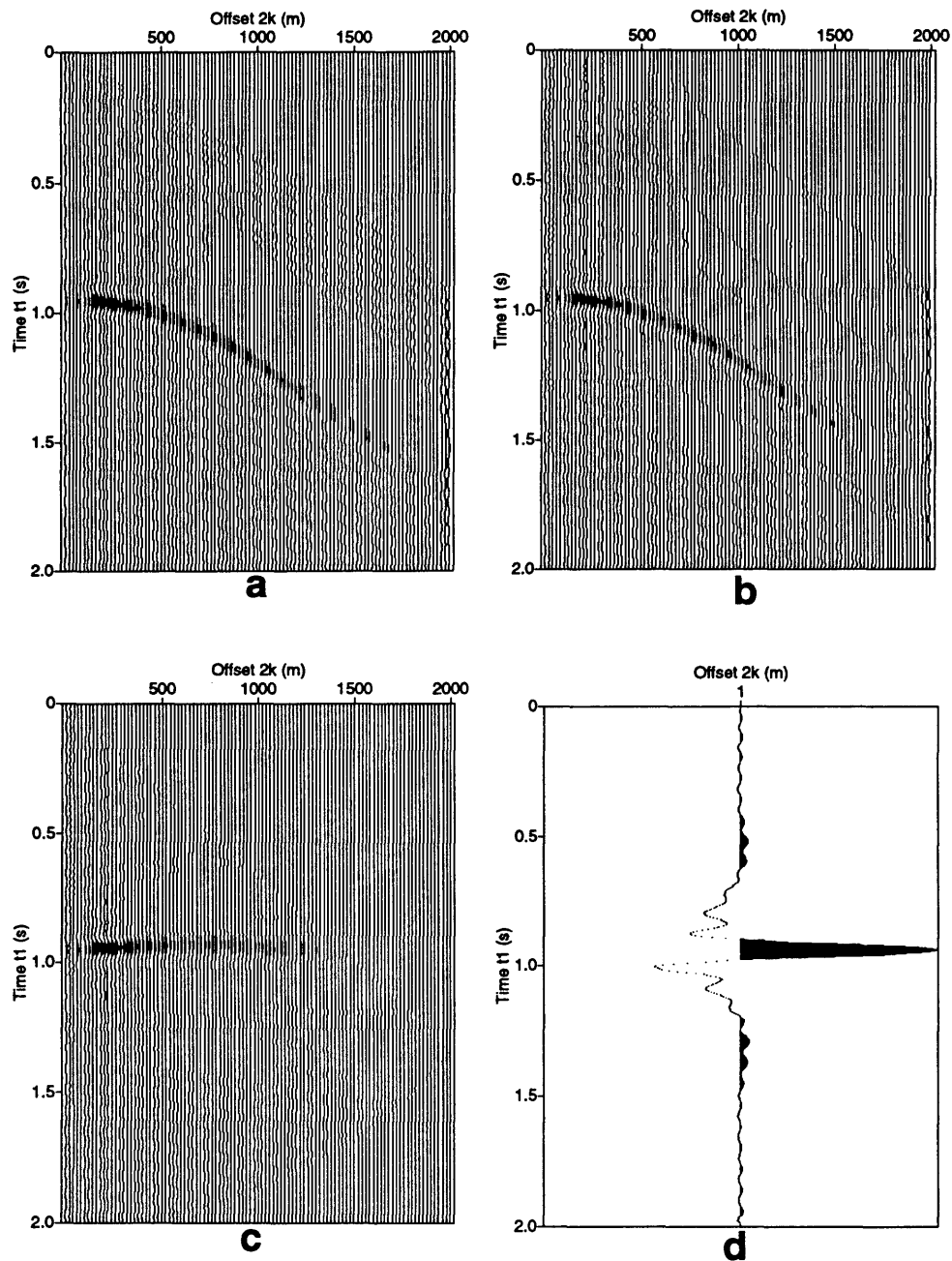


FIG. 6.10. Analysis in the $k-t_1$ domain for a horizontal reflector. (a) output $k-t_1$ gather; (b) same gather after filtering; (c) NMO-corrected gather ($v = 1350$ m/s); (d) stacked trace.

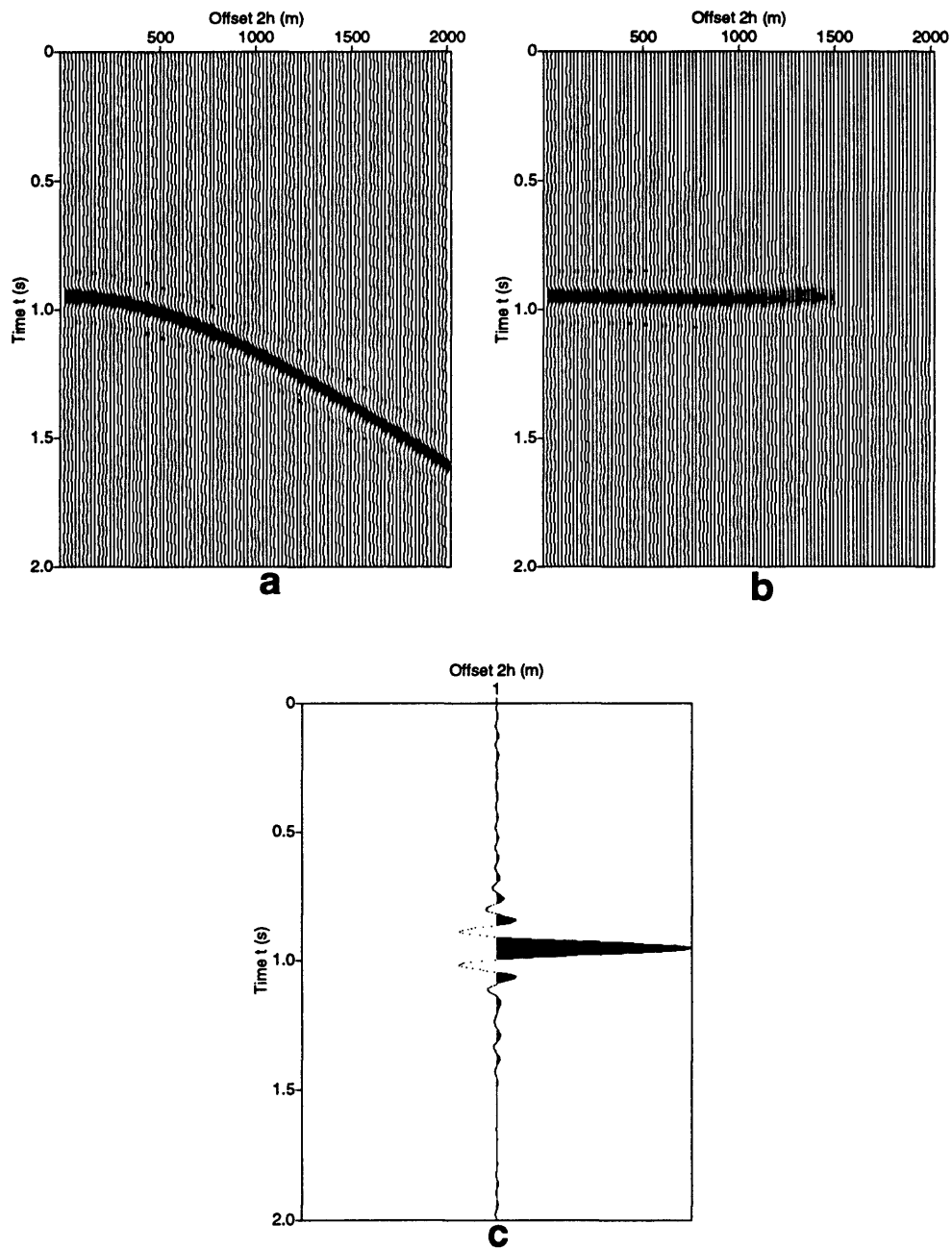


FIG. 6.11. Analysis in the $h-t$ domain for a horizontal reflector. (a) CMP gather at the location of the velocity analysis; (b) NMO-corrected gather ($v = 1480$ m/s); (c) stacked trace.

ures 6.12 and 6.13. The stacking velocity obtained in the $k-t_1$ domain (1360 m/s) is, again, practically the same as the average velocity. This time, however, the stacking velocity from the $h-t$ domain (2450 m/s) is about *85 percent higher* than the average velocity, again not accounted for by the $\cos \theta$ factor.

From the foregoing examples, I conclude that velocity analysis in the $h-t$ domain, for mode-converted waves, can yield highly erroneous results; not only does the velocity depend on the dip, but also on the sign of the dip. Those velocities should not be used in time-to-depth conversion or any application other than CMP stacking. On the other hand, the velocity obtained in the $k-t_1$ domain does not depend on dip; it is close to the average velocity v_a . This average velocity can be reliably used in seismic applications, such as transformation to zero offset, migration, and even time-to-depth conversion. Although the $k-t_1$ approach is not highly sensitive to the choice of the velocity ratio γ (results not shown), it is important to include a reasonable estimate for γ in the transformation to the $k-t_1$ domain. That is, Gardner's conventional $k-t_1$ approach (assuming $\gamma = 1$) yields poor velocity results if applied to mode-converted data.

6.6 Summary

Investigation of the $k-t_1$ TZO method reveals that this method has three problems; namely, improper treatment of amplitude and phase, AVO distortion, and a problem with the large-offset traces. In addition, neither the AVO nor the large-offset problems can be overcome, even when dealing only with ordinary p-waves. I recommend, therefore, that the $k-t_1$ TZO approach *not be used* as a primary scheme in processing seismic data, whether mode-converted or conventional p-wave. This approach, however, could be useful in deducing velocity information for mode-converted

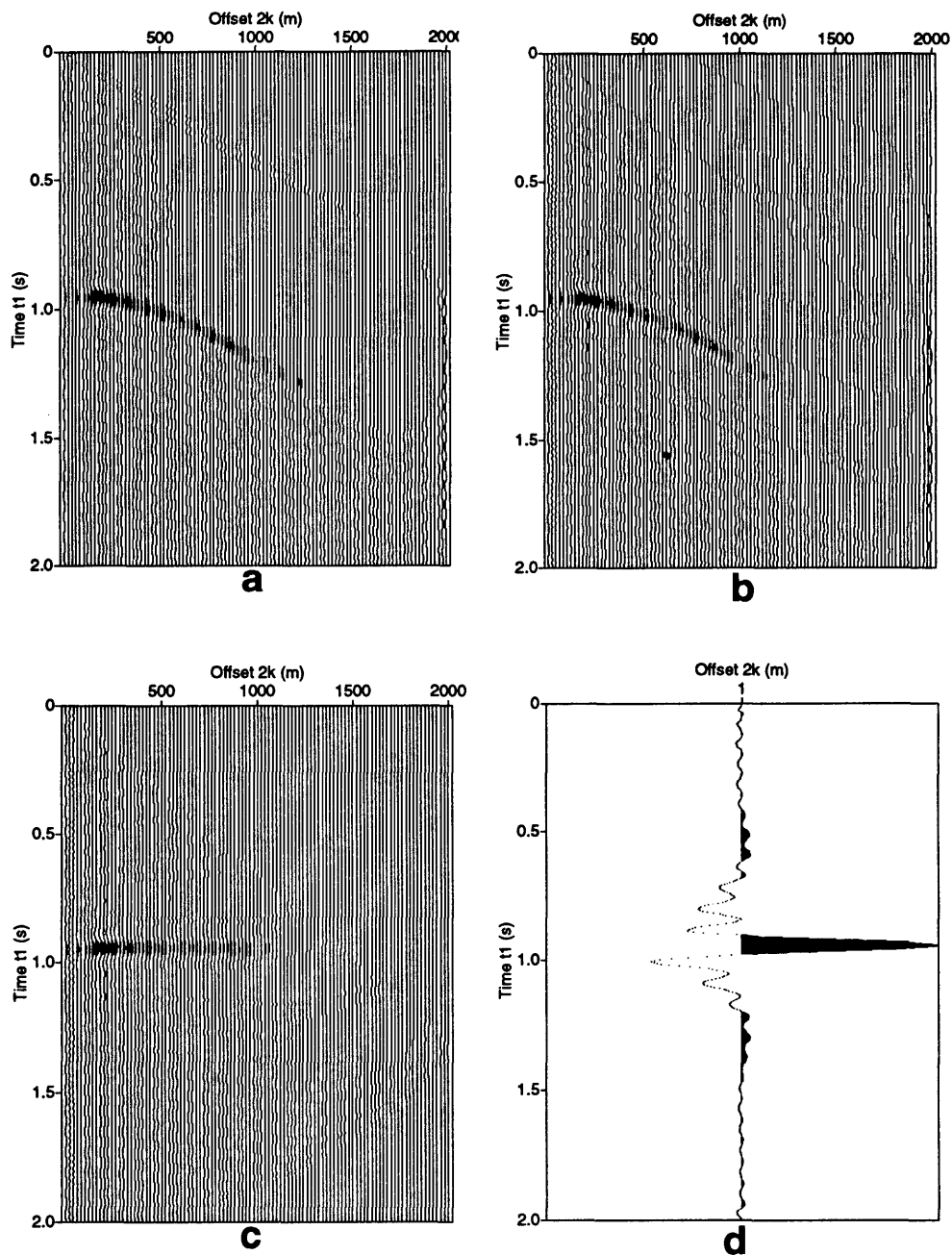


FIG. 6.12. Analysis in the $k-t_1$ domain for a dipping reflector (dip= 25° , upward from source to receiver). (a) output $k-t_1$ gather; (b) same gather after filtering; (c) NMO-corrected ($v = 1360$ m/s); (d) stacked trace.

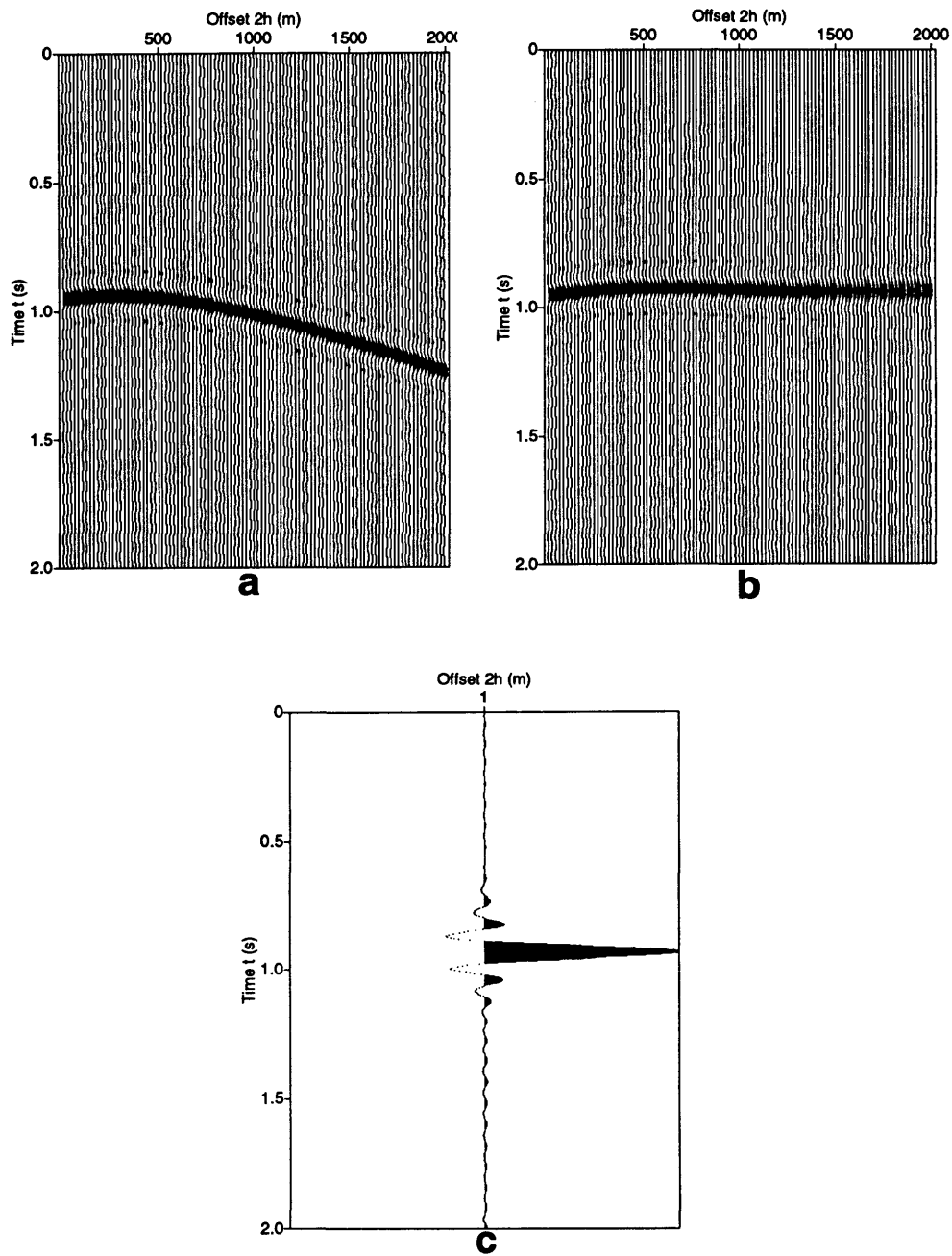


FIG. 6.13. Analysis in the $h-t$ domain for a dipping reflector (dip= 25° , upward from source to receiver). (a) input CMP gather; (b) NMO-corrected gather ($v = 2450$ m/s); (c) stacked trace.

seismic data as long as mode-conversion is taken into account in the transformation to the k - t_1 domain.

Chapter 7

CONCLUSION

In addition to an existing Kirchhoff ($t-x$) implementation, and as discussed in this thesis, TZO for mode-converted waves can also be implemented in either of two domains—the nonphysical $k-t_1$ domain, and the frequency-wavenumber ($f-k$) domain. I now summarize my views on these two TZO approaches.

For a constant-velocity medium, the $k-t_1$ TZO approach is, in principle, exact. However, the $k-t_1$ approach has three intrinsic problems associated with it: problems of amplitude and phase, of AVO, and of large-offset. Due to these unresolved problems, the $k-t_1$ TZO approach is deemed unfavorable for practical use in generating zero-offset sections. Although the discussion here pertains solely to mode-converted waves, the conclusion that the implementation of the $k-t_1$ TZO method be avoided applies equally well to ordinary p-waves. However, one useful application on $k-t_1$ data is velocity analysis, in which case resulting velocities are dip-independent, even for mode-converted waves.

The $f-k$ TZO approach for mode-converted waves, though approximate, is straightforward and easy to implement. Its implementation requires only slight modification to an existing algorithm—the Hale's $f-k$ TZO algorithm used in processing ordinary p-waves. The mode-converted TZO operator differs from the well-known, elliptical p-wave operator in two aspects. First, its non-elliptical shape is controlled solely by the velocity ratio which, depending on the mode of conversion, squeezes one side of the operator and stretches the other. Second, the operator is laterally

shifted, and in a time-varying manner. Furthermore, when the velocity ratio is unity (no mode conversion) the mode-converted TZO operator reduces to the conventional operator. As with conventional TZO, Hale and Artley's squeezing trick is readily extended to mode conversion so that mode-converted TZO can approximately handle velocity variations with depth.

Although the method is not too sensitive to the choice of velocity ratio, tests on synthetic data show that it is essential to take mode conversion into account when applying TZO. Application of this mode-converted f - k TZO method to synthetic seismic data reveals that the method is capable, to a great extent, of transforming data to zero offset. The method corrects data from both dipping reflectors regardless of the sign of dip, and from horizontal reflectors by laterally shifting reflections to their appropriate zero-offset locations.

Results from two field data sets show that the dip influence on stacking velocity has significantly decreased after application of mode-converted TZO, a result that conventional TZO has failed to produce. Furthermore, this method can be used, in conjunction with velocity analysis, to qualitatively estimate a velocity ratio γ from field data (since the mode-converted TZO method is not too sensitive to the choice of γ , one would actually be able to estimate a range of γ , rather than a single, precise value of γ). Also, with the availability of two data sets shot over the same area but in opposite directions (as the field example in this thesis), one can make use of the relative lateral shift between their two stacks to estimate a velocity ratio.

Finally, I recommend that this f - k TZO method for mode-converted waves be further modified to handle the more general situation wherein the velocity ratio varies with depth. The influence of anisotropy on this mode-converted TZO process could also be investigated. More specifically, I recommend that the work by Larner (1993),

on TZO error due to anisotropy for ordinary p-waves, be extended to mode conversion. Such a study on synthetic data would provide insight as to how mode-converted TZO would behave in transversely isotropic media.

REFERENCES

- Bleistein, N., 1984, *Mathematical methods for wave phenomena*: Academic Press.
- Clark, S. P., Jr, 1966, *Handbook of physical constants*: The Geological Society of America, Inc., Memoir 97.
- Corbin, R. J., Bell, D. W., and Danbom, S. H., 1988, Shear- and compressional-wave surface and downhole tests in southern Louisiana, *in* Danbom, S. H., and Domenico, S. N., Eds., *Shear-wave exploration: Geophysical Developments 2*, Soc. Expl. Geophys., 62–75.
- Den Rooijen, H. P. G. M., 1991, Stacking of p–sv reflection data using dip moveout: *Geophysical Prospecting*, **39**, 585–598.
- Deregowski, S. M., 1986, What is DMO: *First Break*, **4**, 7–24.
- DeSanto, J., 1986, *Mathematics of Seismology*: Colorado School of Mines, CWP Report 044.
- Dobrin, M. B., and Savit, C. H., 1988, *Introduction to geophysical prospecting*, 4th edition: McGraw-Hill Book Company.
- Forel, D., 1986, Dip moveout correction in three and two dimensions: M.S. Thesis, University of Houston.
- Forel, D., and Gardner, G., 1988, A three-dimensional perspective on two-dimensional dip moveout: *Geophysics*, **53**, 604–610.
- Hale, D., 1984, Dip-moveout by Fourier transform: *Geophysics*, **49**, 741–757.
- Hale, D., 1988, Dip moveout processing: Soc. Expl. Geophys. course notes.
- Hale, D., 1991, A nonaliased integral method for dip moveout: *Geophysics*, **56**, 795–805.
- Hale, D., and Artley, C., 1991, Squeezing dip moveout for depth-variable velocity: Colorado School of Mines, CWP Report 112.
- Harrison, M., 1990, Converted wave DMO: Presented at the 60th Ann. Internat. Mtg., Soc. Expl. Geophys., Expanded Abstracts, 1370–1373.

- Hubral, P., and Krey, T., 1980, Interval velocities from seismic reflection time measurements: Soc. Expl. Geophys. Series.
- Larner, K., 1993, Dip-moveout error in transversely isotropic media with linear velocity: Geophysics, **58**.
- Levin, F., 1971, Apparent velocity from dipping interface reflections: Geophysics, **36**, 510–516.
- Liner, C., 1988, General theory and comparative anatomy of dip moveout: Colorado School of Mines, CWP Report 073R.
- Liner, C., 1990, General theory and comparative anatomy of dip moveout: Geophysics, **55**, 595–607.
- Newman, P., 1990, Amplitude and phase properties of a digital migration process: First Break, **8**, 397–403.
- Notfors, C. D., and Godfrey, R. J., 1987, Dip moveout in the frequency-wavenumber domain: Geophysics, **52**, 1718–1721.
- Ottolini, R., 1982, Migration of reflection seismic data in angle-midpoint coordinates: Ph.D. Thesis, Stanford University.
- Sword, C., 1984, Approximating the kinematics of converted waves: Stanford Exploration Project Report **41**, 347–368, Stanford University.
- Tessmer, G., and Behle, A., 1988, Common reflection point data-stacking technique for converted waves: Geophysical Prospecting, **36**, 671–688.
- Yilmaz, O., 1987, Seismic data processing: Investigations in Geophysics 2, Soc. Expl. Geophys.

Appendix A

OFFSET AND TRAVELTIME FOR MODE-CONVERTED WAVES

Let the offset distance separating source s and receiver g be x , as shown in the depth section in Figure A.1. We assume a plane reflector, with dip θ , beneath a constant-velocity layer. For mode-converted waves, when the downgoing wave travels at velocity v (along the path l_s from source to reflector), then the reflected upgoing wave (along the path l_g) travels at a different velocity, γv . The mode of conversion is determined by the value of the velocity ratio γ . The mode of conversion is p–sv for $\gamma < 1$, and sv–p for $\gamma > 1$. There is no mode conversion (only ordinary p- or s-waves) when $\gamma = 1$. The incident and reflection angles, as measured relative to the perpendicular to the reflector at the reflection point, are ϕ_s and ϕ_g , respectively. Unlike the situation for ordinary p-waves, angles ϕ_s and ϕ_g are not equal for mode-converted waves; the relation between them is given by Snell's law, as follows.

$$\sin \phi_s = \frac{\sin \phi_g}{\gamma}. \quad (\text{A.1})$$

Let the distance from the midpoint y , between source and receiver, to the reflector be D , the distance from source to reflector be D_s , and that from receiver to reflector be D_g , as shown in the figure.

The offset distance x can be obtained as the sum of two distances, x_s and x_g , as

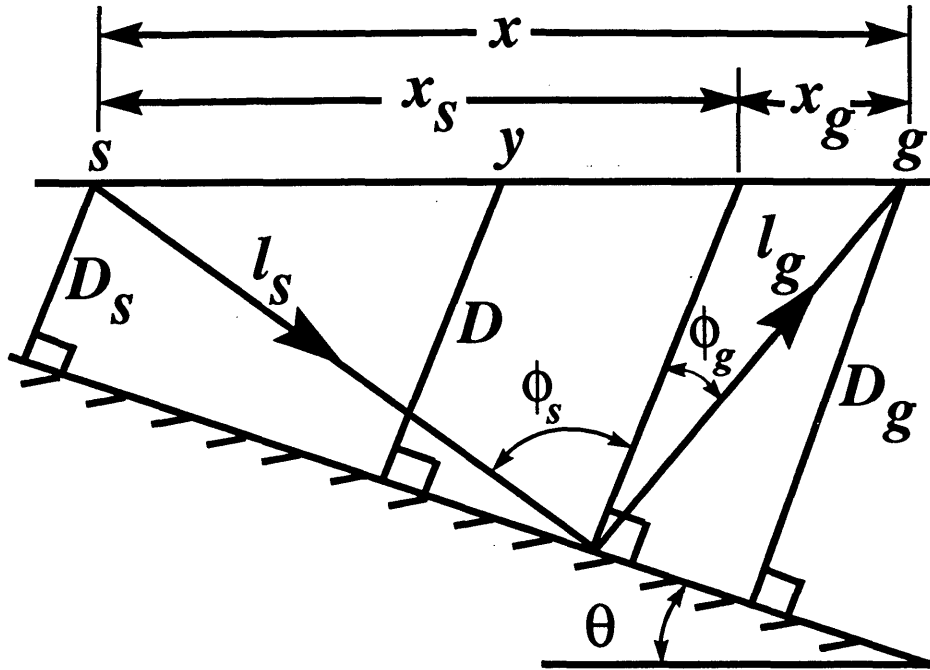


FIG. A.1. Depth section depicting a mode-converted, reflection raypath in a homogeneous medium with a dipping reflector.

shown in the figure. Using the law of sines, x_s and x_g are obtained as

$$x_s = \frac{l_s \sin \phi_s}{\cos \theta},$$

$$x_g = \frac{l_g \sin \phi_g}{\cos \theta}.$$

The offset distance can then be expressed as

$$x = x_s + x_g = \frac{1}{\cos \theta} (l_s \sin \phi_s + l_g \sin \phi_g). \quad (\text{A.2})$$

Using, once again, the law of sines (see the geometry of the figure), distances l_s and

l_g in equation A.2 can be written as

$$\begin{aligned} l_s &= \frac{D_s}{\cos \phi_s}, \\ l_g &= \frac{D_g}{\cos \phi_g}, \end{aligned} \quad (\text{A.3})$$

where D_s and D_g are given by

$$\begin{aligned} D_s &= D - \frac{x \sin \theta}{2}, \\ D_g &= D + \frac{x \sin \theta}{2}. \end{aligned} \quad (\text{A.4})$$

By substituting equations (A.3) and (A.4) into equation (A.2) and simplifying, I obtain

$$x = \frac{2D(\tan \phi_s + \tan \phi_g)}{2\cos\theta + \sin\theta(\tan \phi_s - \tan \phi_g)}, \quad (\text{A.5})$$

which is the same as equation (2.12).

Traveltime t , from source to reflector (along path l_s) and back to receiver (along l_g), can be expressed as

$$t = \frac{1}{v} \left(l_s + \frac{l_g}{\gamma} \right). \quad (\text{A.6})$$

After substitution for l_s and l_g their expressions from equation (A.3) and simplification using equation (A.4), equation (A.6) reduces to

$$t = \frac{1}{v} \left[D \left(\frac{1}{\cos \phi_s} + \frac{1}{\gamma \cos \phi_g} \right) + \frac{x \sin \theta}{2} \left(\frac{1}{\gamma \cos \phi_g} - \frac{1}{\cos \phi_s} \right) \right], \quad (\text{A.7})$$

which is the same as equation (2.13) in the main text.

Appendix B

SERIES EXPANSION

For mode-converted waves, the traveltime is not an even function of offset when dip is present. A series expansion of traveltime as a function of offset should, therefore, contain both even and odd powers of offset. For convenience, I choose to expand the square of the traveltime, as follows

$$t^2 = c_0 + c_1x + c_2x^2 + c_3x^3 + c_4x^4 + \dots, \quad (\text{B.1})$$

where x is the offset distance separating source s and receiver g , as shown in Figure B.1. The goal here is to determine the coefficients c_i in equation (B.1).

Define a slowness parameter ν , along the dipping interface, that relates the incident and reflection angles, ϕ_s and ϕ_g , respectively, as follows

$$\nu = \frac{\sin \phi_s}{v} = \frac{\sin \phi_g}{\gamma v}, \quad (\text{B.2})$$

where we recall that v and γv are the downgoing and upgoing velocities, respectively. Using trigonometric substitution, $\tan \phi_s$ and $\tan \phi_g$ are easily found from equation (B.2) as follows

$$\begin{aligned} \tan \phi_s &= \frac{\sin \phi_s}{\cos \phi_s} = \frac{v\nu}{\sqrt{1 - (v\nu)^2}}, \\ \tan \phi_g &= \frac{\sin \phi_g}{\cos \phi_g} = \frac{\gamma v\nu}{\sqrt{1 - (\gamma v\nu)^2}}. \end{aligned} \quad (\text{B.3})$$

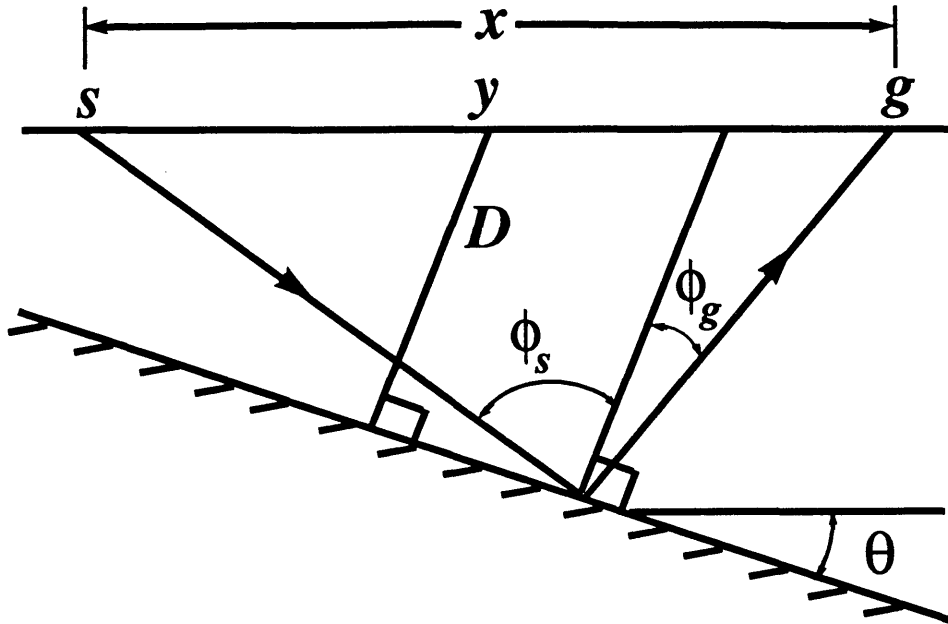


FIG. B.1. Depth section depicting a mode-converted, reflection raypath in a homogeneous medium with a dipping reflector.

The offset distance x , given by equation (A.5), can thus be expressed as a function of the slowness parameter ν after substituting for $\tan \phi_s$ and $\tan \phi_g$ their expressions from equation (B.3). Expansion of x in the parameter ν , then, is given by the following Taylor series

$$\begin{aligned}
 x = & \frac{D\nu(1+\gamma)}{\cos\theta}\nu + \frac{D\nu^2(\gamma^2-1)\sin\theta}{2\cos^2\theta}\nu^2 \\
 & + D\nu^3 \left[\frac{1+\gamma^3}{2\cos\theta} + \frac{(1-\gamma)^2(1+\gamma)\sin^2\theta}{4\cos^3\theta} \right] \nu^3 \\
 & + \frac{D(\gamma^2-1)v^4\sin\theta[4\cos^2\theta(1+\gamma^2) + \sin^2\theta(1-\gamma^2)]}{8\cos^4\theta}\nu^4 + \dots \quad (\text{B.4})
 \end{aligned}$$

Similarly, expansions of x^2 , x^3 , and x^4 are given by

$$x^2 = \frac{D^2 v^2 (1 + \gamma)^2}{\cos^2 \theta} \nu^2 + \frac{D^2 v^3 (\gamma - 1) (1 + \gamma)^2 \sin \theta}{\cos^3 \theta} \nu^3 + D^2 v^4 \left[\frac{(1 + \gamma) (1 + \gamma^3)}{\cos^2 \theta} + \frac{3(1 - \gamma^2)^2 \sin^2 \theta}{4 \cos^4 \theta} \right] \nu^4 + \dots, \quad (\text{B.5})$$

$$x^3 = \frac{D^3 v^3 (1 + \gamma)^3}{\cos^3 \theta} \nu^3 + \frac{3D^3 v^4 (\gamma - 1) (1 + \gamma)^3 \sin \theta}{2 \cos^4 \theta} \nu^4 + \dots, \quad (\text{B.6})$$

and

$$x^4 = \frac{D^4 v^4 (1 + \gamma)^4}{\cos^4 \theta} \nu^4 + \dots \quad (\text{B.7})$$

The relation for the traveltime, equation (A.7), can also be expressed as a function of the slowness parameter ν , by substituting for $\tan \phi_s$ and $\tan \phi_g$ their expressions from equation (B.3). Taylor expansion of the square of the traveltime in the parameter ν is found to be

$$t^2 = \frac{D^2 (1 + \gamma)^2}{\gamma^2 v^2} - \frac{D^2 (\gamma - 1) (1 + \gamma)^2 \sin \theta}{\gamma^2 v \cos \theta} \nu - \frac{D^2 (1 + \gamma^2) [(1 - \gamma)^2 \sin^2 \theta - 4\gamma \cos^2 \theta]}{4\gamma^2 \cos^2 \theta} \nu^2 - \frac{D^2 v (\gamma^2 - 1) (1 + \gamma^3) \sin \theta}{2\gamma^2 \cos \theta} \nu^3 + \dots \quad (\text{B.8})$$

The coefficients c_i are then recursively found by, first, substituting equations (B.4), (B.5), (B.6), (B.7), and (B.8) into equation (B.1) and, second, matching like powers of ν after the substitution. The first five coefficients are

$$c_0 = \left(\frac{2D}{v_a} \right)^2 \equiv t_0^2,$$

$$c_1 = \frac{2(1 - \gamma)t_0 \sin \theta}{(1 + \gamma)v_a},$$

$$\begin{aligned}
 c_2 &= \frac{4\gamma \cos^2 \theta + (1 - \gamma)^2 \sin^2 \theta}{(1 + \gamma)^2 v_a^2}, \\
 c_3 &= \frac{8\gamma(1 - \gamma) \cos^2 \theta \sin \theta}{(1 + \gamma)^3 t_0 v_a^3}, \\
 c_4 &= \frac{4\gamma(1 - \gamma) \cos^2 \theta [(\gamma - 1) \cos^2 \theta + (2 - 2\gamma - \gamma^2) \sin^2 \theta]}{(1 + \gamma)^4 t_0^2 v_a^4},
 \end{aligned}$$

where v_a is the same average velocity given by equation (2.9), i.e.,

$$\frac{2}{v_a} = \frac{1}{v} + \frac{1}{\gamma v}.$$

Appendix C

IMPULSE RESPONSE VIA STATIONARY PHASE

The method of stationary phase (Bleistein, 1984) is useful in finding asymptotic solutions to certain integrals that are, otherwise, hard to solve analytically. In particular, an integral of the form

$$I = \int f(\xi) e^{i\Phi(\xi)} d\xi \quad (\text{C.1})$$

will have an asymptotic solution given by the stationary phase-formula if I has at least one stationary point.

Any point in the range of integration of I is defined as a stationary point, ξ_s , if it satisfies the following relation

$$\left. \frac{d\Phi(\xi)}{d\xi} \right|_{\xi=\xi_s} = \Phi'(\xi_s) = 0,$$

where $\Phi(\xi)$ is the phase seen in the integrand of I . If such a stationary point exists, then I in equation (C.1) is asymptotically given (Bleistein, 1984) by

$$I \sim \left[\frac{2\pi}{|\Phi''(\xi_s)|} \right]^{1/2} f(\xi_s) e^{i\Phi(\xi_s) + i\frac{\pi}{4} \text{sgn}[\Phi''(\xi_s)]}, \quad (\text{C.2})$$

where the sgn function is defined by

$$sgn(\zeta) \equiv \begin{cases} 1 & , \zeta > 0 , \\ -1 & , \zeta < 0 . \end{cases}$$

If there exists more than one stationary point along the range of integration, then the superposition of their individual contributions, each given by relation (C.2), gives the asymptotic value of I .

We follow the approach of Liner (1988), but dealing with mode-conversion here, to derive an impulse response based on the approximate TZO formulation given by equation (3.15). We start by rewriting that equation as

$$P_0(\omega, k) = \int dt_n A^{-1} e^{i(\omega A t_n + B k)} \int dy e^{-iky} p_n(t_n, y), \quad (C.3)$$

where, for convenience here, the dependence of both P_0 and p_n on the constant half-offset h is not shown. Definitions for A and B are given in equations (3.14) and (3.16), respectively. Equation (C.3) can also be expressed as

$$P_0(\omega, k) = \int dt_n G(\omega, t_n, k) p_n(t_n, k), \quad (C.4)$$

where $G(\omega, t_n, k)$ is given by

$$G(\omega, t_n, k) = A^{-1} e^{i(-CHk + \omega A t_n)}, \quad (C.5)$$

and the parameter C , introduced for convenience, is defined by

$$C = \frac{1 - \gamma}{2\sqrt{\gamma}}.$$

The scaled-offset, H , was defined in equation (3.18). Taking the inverse Fourier transform over wavenumber in equation (C.5), we get

$$G(\omega, t_n, y) = \frac{1}{2\pi} \int dk A^{-1} e^{i(-CHk + \omega A t_n)} e^{iky}, \quad (\text{C.6})$$

We now apply the method of stationary phase to the integral in equation (C.6). If we express that integral as

$$G(\omega, t_n, y) = \frac{1}{2\pi} \int dk A^{-1} e^{i\Phi(k)}, \quad (\text{C.7})$$

then the phase $\Phi(k)$ is given by

$$\Phi(k) = -CHk + \sqrt{\omega^2 t_n^2 + H^2 k^2} + ky.$$

Solving for the zeros of $d\Phi(k)/dk$, we find a single stationary point, k_s , given by

$$k_s = -\frac{\omega t_n (y - CH)}{H [H^2 - (y - CH)^2]^{1/2}}. \quad (\text{C.8})$$

The asymptotic value of the integral in equation (C.6), using the stationary-phase formula given in equation (C.2), is then

$$G(\omega, t_n, y) \sim \frac{1}{2\pi} \left[\frac{2\pi}{|\Phi''(k_s)|} \right]^{1/2} A^{-1}(k_s) e^{i\Phi(k_s) + i\frac{\pi}{4} \text{sgn}[\Phi''(k_s)]}. \quad (\text{C.9})$$

In order to apply the stationary-phase formula here, we need to evaluate the following expressions at the stationary point

$$A^{-1}(k_s) = \frac{\sqrt{H^2 - (y - CH)^2}}{H},$$

$$\Phi(k_s) = \frac{\omega t_n}{H} \sqrt{H^2 - (y - CH)^2},$$

and

$$\Phi''(k_s) = \frac{[H^2 - (y - CH)^2]^{3/2}}{H\omega t_n}.$$

Noting that the sign of the argument of the *sgn* function is totally determined by the sign of ω , and applying Euler's identity to the exponential with the *sgn* function, the expression in equation (C.9), after simplification, becomes

$$G(\omega, t_n, y) \sim \left[\frac{i^{\text{sgn}(\omega)} \omega t_n}{2\pi} \right]^{1/2} \frac{1}{H^{1/2} [H^2 - (y - CH)^2]^{1/4}} e^{i \frac{\omega t_n}{H} [H^2 - (y - CH)^2]^{1/2}}. \quad (\text{C.10})$$

To proceed, refer to equation (C.4) and express the product of the two terms $G(\omega, t_n, k) P_n(t_n, k)$ as a convolution over midpoint y . That is, using the convolution theorem, equation (C.4) is written as

$$P_0(\omega, y) = \int dt_n \int dy' G(\omega, t_n, y - y') p_n(t_n, y'), \quad (\text{C.11})$$

where y and y' are output and input midpoint coordinates, respectively. Substituting for $G(\omega, t_n, y - y')$ its counterpart from equation (C.10), equation (C.11) then yields

$$\hat{P}_0(\omega, y) = \left(\frac{1}{2\pi} \right)^{1/2} \int dt_n \int dy' \frac{t_n^{1/2}}{H[1 - (\xi - C)^2]^{1/4}} e^{i\omega t_n [1 - (\xi - C)^2]^{1/2}} p_n(t_n, y'), \quad (\text{C.12})$$

where

$$\hat{P}_0(\omega, y) = \frac{P_0(\omega, y)}{[i^{\text{sgn}(\omega)} \omega]^{1/2}},$$

and

$$\xi = \frac{y - y'}{H}.$$

We now take the inverse Fourier transform over frequency of equation (C.12), obtaining

$$\hat{P}_0(t_0, y) = \left(\frac{1}{2\pi}\right)^{3/2} \int dt_n \int dy' \frac{t_n^{1/2} p_n(t_n, y')}{H[1 - (\xi - C)^2]^{1/4}} \int d\omega e^{-i\omega\{t_0 - [1 - (\xi - C)^2]^{1/2} t_n\}}. \quad (\text{C.13})$$

Realizing that the last integral is 2π times a delta function, equation (C.13) can be written as

$$\hat{P}_0(t_0, y) = \left(\frac{1}{2\pi}\right)^{1/2} \int dt_n \int dy' \frac{t_n^{1/2} \delta\{t_0 - [1 - (\xi - C)^2]^{1/2} t_n\}}{H[1 - (\xi - C)^2]^{1/4}} p_n(t_n, y') \quad (\text{C.14})$$

We make use of the scaling property of the delta function to simplify equation (C.14). Specifically, we apply

$$\delta\{t_0 - [1 - (\xi - C)^2]^{1/2} t_n\} = [1 - (\xi - C)^2]^{-1/2} \delta\{t_n - t_0 [1 - (\xi - C)^2]^{-1/2}\},$$

and then sift $t_n^{1/2} = t_0^{1/2} [1 - (\xi - C)^2]^{-1/4}$, to obtain

$$\hat{P}_0(t_0, y) = \left(\frac{t_0}{2\pi}\right)^{1/2} \int dt_n \int dy' \frac{\delta\{t_n - t_0 [1 - (\xi - C)^2]^{-1/2}\}}{H[1 - (\xi - C)^2]} p_n(t_n, y'). \quad (\text{C.15})$$

Finally, we get the geometry of the impulse response from the zero of the delta-function argument, given by

$$t_n = t_0 [1 - (\xi - C)^2]^{-1/2}.$$

For convenience, we assume the input midpoint location, y' , to be at the origin. The

above relation, then, can be written as

$$\left(\frac{t_0}{t_n}\right)^2 + \left(\frac{Y_0}{H}\right)^2 = 1, \quad (\text{C.16})$$

where $Y_0 = y - [(1 - \gamma)h/(1 + \gamma)]$. For constants t_n and H , equation (C.16) describes an ellipse in t_0 and Y_0 . This equation is the same as equation (3.17) in the main text.

Appendix D

QUARTIC EQUATION FOR b

For ordinary p-wave reflection, the location of an equivalent zero-offset reflection, i.e., b , can be analytically derived, as a function of offset, depth, and dip. Figure D.1, which shows a depth section with a dipping reflector, is used to find b in the presence of mode-conversion.

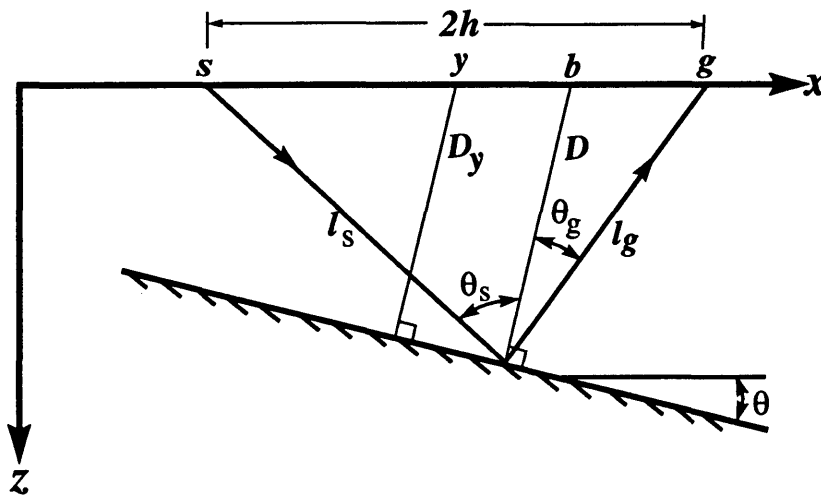


FIG. D.1. Depth section depicting a raypath for p-sv mode conversion. The trace has offset $2h$ between source s and receiver g . The distance from the midpoint y to the dipping reflector is D_y , and that from b (the location of an equivalent zero-offset trace) to the reflector is D . The distance from s along the raypath to the reflector is l_s , and that from the reflector to g is l_g . The incidence and reflection angles are θ_s and θ_g , respectively, and reflector dip is θ .

From the Pythagorean theorem, and noting that

$$D = D_y + b \sin \theta, \quad (\text{D.1})$$

the distance along the raypath from the source to the reflector, l_s , and that from the reflector to the receiver, l_g , can be expressed as

$$l_s = \sqrt{(h + b)^2 \cos^2 \theta + (D_y - h \sin \theta)^2}, \quad (\text{D.2})$$

$$l_g = \sqrt{(h - b)^2 \cos^2 \theta + (D_y + h \sin \theta)^2}. \quad (\text{D.3})$$

At the reflection point, Snell's law is

$$\frac{\sin \theta_s}{\sin \theta_g} = \frac{1}{\gamma}. \quad (\text{D.4})$$

From the geometry of Figure D.1, and taking positive dips downward from source to receiver,

$$\sin \theta_s = \frac{(h + b) \cos \theta}{l_s}, \quad (\text{D.5})$$

and

$$\sin \theta_g = \frac{(h - b) \cos \theta}{l_g}. \quad (\text{D.6})$$

By substituting equations (D.5) and (D.6) into equation (D.4), we get

$$l_g = \frac{l_s h - b}{\gamma h + b}. \quad (\text{D.7})$$

For a downgoing velocity v , and recorded time t , we have

$$vt = l_s + l_g/\gamma. \quad (\text{D.8})$$

Substitution of equation (D.7) into equation (D.8) yields

$$vt = l_s \left(1 + \frac{1}{\gamma^2} \frac{h-b}{h+b} \right). \quad (\text{D.9})$$

Equation (D.9), upon substituting expression (D.2) for l_s and squaring both sides, becomes

$$(vt)^2 = \left[(h+b)^2 \cos^2 \theta + (D_y - h \sin \theta)^2 \right] \left(1 + \frac{1}{\gamma^2} \frac{h-b}{h+b} \right)^2. \quad (\text{D.10})$$

But the term $(vt)^2$ can also be solved for, from the kinematics relations for mode-converted waves (equations [2.11] and [2.9]), as

$$(vt)^2 = 2h(\alpha h + \beta b) \left(1 + \frac{D^2}{h^2 - b^2} \right), \quad (\text{D.11})$$

which can also be expressed in terms of D_y (equation [D.1]) as

$$(vt)^2 = 2h(\alpha h + \beta b) \left[1 + \frac{(D_y + b \sin \theta)^2}{h^2 - b^2} \right]. \quad (\text{D.12})$$

Eliminating $(vt)^2$ from equations (D.10) and (D.12) and simplifying yields the following quartic equation in b

$$\begin{aligned} & \left[(h+b)^2 \cos^2 \theta + (D_y - h \sin \theta)^2 \right] (\alpha h + \beta b)(h-b) = \\ & 2h(h+b) \left[h^2 - b^2 + (D_y + b \sin \theta)^2 \right]. \end{aligned} \quad (\text{D.13})$$

For a horizontal reflector, $\theta = 0$, equation (D.13) simplifies a bit, but remains quartic in b . In this case, the depth $D = D_y$ of the horizontal reflector is trivially found in terms of b ,

$$D^2 = -\frac{(h^2 - b^2)^2}{h^2 + 2\alpha hb/\beta + b^2},$$

which is the same as equation (3.20) in the main text.

Appendix E

FRESNEL-ZONE WIDTH

Before discussing the Fresnel zone, I first derive the general form of the smile, the stack of which generates a $k-t_1$ trace. Only ordinary p-waves are considered, i.e., $\gamma = 1$. For $\gamma \neq 1$, the mathematics become rather tedious, as quartic symbolic equations arise.

Consider the surface point a (Figure E.1) at which a $k-t_1$ gather is to be generated from input CMP gathers. A constant-velocity, single-reflector medium is assumed.

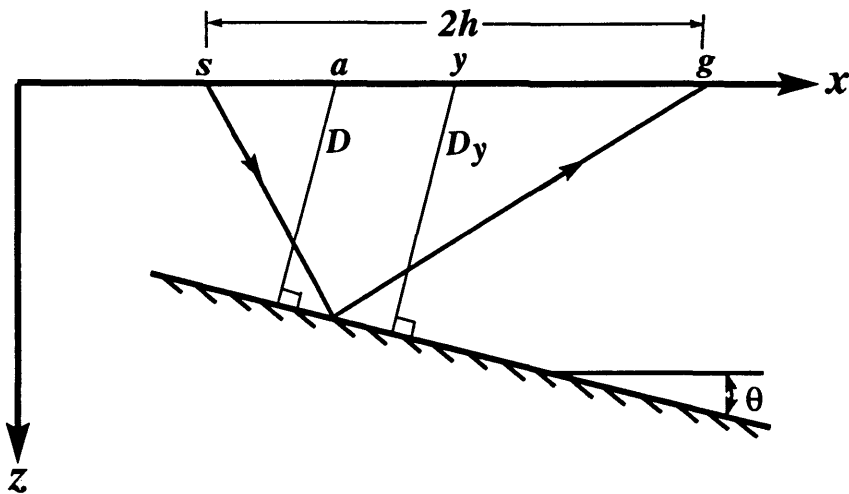


FIG. E.1. Subsurface model consisting of a single dipping reflector in a constant-velocity medium. An output $k-t_1$ gather is desired at location a . Any midpoint y with source-receiver ($s-g$) offset ($2h$) encompassing point a will contribute to the output $k-t_1$ gather. The zero-offset time, which the $k-t_1$ gather inherits, is experienced along path D .

With D being the distance from point a to the reflector, the theoretical zero-offset time at point a is given by

$$t_0 = \frac{2D}{v}, \quad (\text{E.1})$$

where v is the medium velocity. Any trace whose source-receiver line encompasses point a will contribute to the output k - t_1 gather. One such trace is depicted in the figure, with distance $2h$, between source s and receiver g , encompassing point a . Because the reflector is dipping, the distance D_y from midpoint y to the reflector varies with location of midpoint.

The recorded time t from the source down to the reflector and back up to the receiver can be expressed as

$$t^2 = t_{0y}^2 + \left(\frac{2h \cos \theta}{v} \right)^2, \quad (\text{E.2})$$

where t_{0y} is the midpoint zero-offset time, given by $t_{0y} = 2D_y/v$. For convenience, let point a be the origin. Then t_{0y} can be expressed as

$$t_{0y} = t_0 + \frac{2y \sin \theta}{v}, \quad (\text{E.3})$$

with positive dip being downward from source to receiver. Substitution of equation (E.3) into equation (E.2) yields

$$t^2 = \left(t_0 + \frac{2y \sin \theta}{v} \right)^2 + \left(\frac{2h \cos \theta}{v} \right)^2. \quad (\text{E.4})$$

For $\gamma = 1$, equation (6.4) becomes $t_1 = kt/h$, which, from equation (E.4), can be written as

$$t_1^2 = \frac{k^2}{h^2} \left[\left(t_0 + \frac{2y \sin \theta}{v} \right)^2 + \left(\frac{2h \cos \theta}{v} \right)^2 \right]. \quad (\text{E.5})$$

Noting that y (Figure E.1) and b (Figure 6.1) are equal, but with opposite signs, equation (6.3) can be used to eliminate h from equation (E.5). The result, after simplification, becomes

$$t_1^2 = \frac{k^2}{k^2 + y^2} \left(t_0 + \frac{2y \sin \theta}{v} \right)^2 + \left(\frac{2k \cos \theta}{v} \right)^2. \quad (\text{E.6})$$

For constant k , equation (E.6) gives the general form of the smile in generating a k trace.

The behavior of the smile depends, among other parameters, on dip, which is normally unknown. In deriving the Fresnel-zone width, I shall assume a horizontal reflector ($\theta = 0$). Then equation (E.6) reduces to

$$t_1^2 = \frac{k^2 t_0^2}{k^2 + y^2} + \left(\frac{2k}{v} \right)^2, \quad (\text{E.7})$$

which describes a symmetric smile whose maximum time is t_{1max} (occurring at $y = 0$) given by

$$t_{1max}^2 = t_0^2 + \left(\frac{2k}{v} \right)^2. \quad (\text{E.8})$$

Let the width of the zone that the smile spans within a time interval Δt_1 be $2\Delta y$.

With $\Delta t_1 \equiv t_{1max} - t_1$, then t_{1max} , t_1 , and Δt_1 are also related by

$$t_{1max}^2 - t_1^2 = (\Delta t_1)^2 + 2t_1 \Delta t_1. \quad (\text{E.9})$$

From equations (E.7) and (E.8), we can write

$$t_{1max}^2 - t_1^2 = t_0^2 - \frac{k^2 t_0^2}{k^2 + (\Delta y)^2}, \quad (\text{E.10})$$

which, after substituting for t_0 its value from equation (E.7) and simplification, can be written as

$$t_{1max}^2 - t_1^2 = \frac{(\Delta y)^2}{k^2} \left[t_1^2 - \left(\frac{2k}{v} \right)^2 \right] \quad (\text{E.11})$$

Equating the right-hand sides of equations (E.9) and (E.11) and solving for Δy , we obtain

$$\Delta y = k \sqrt{\frac{(\Delta t_1)^2 + 2t_1 \Delta t_1}{t_1^2 - \left(\frac{2k}{v} \right)^2}}. \quad (\text{E.12})$$

If Δt_1 is chosen to be half a cycle, i.e., $\Delta t_1 = T/2$, where T is the dominant period of the wavelet, then Δy (half the Fresnel-zone width) can be expressed from equation (E.12) as

$$\Delta y = k \sqrt{\frac{\frac{1}{f} \left(\frac{1}{4f} + t_1 \right)}{t_1^2 - \left(\frac{2k}{v} \right)^2}}, \quad (\text{E.13})$$

where f is the dominant frequency of the wavelet.

It should also be noted that the Fresnel-zone width cannot exceed a maximum value determined by the maximum offset present in the data. Take, for example, the case when $k = 300$ m in Figure 6.3a. The maximum half-offset was 500 m. As equation (6.3) implies, the maximum Fresnel-zone width should be $2\sqrt{500^2 - 300^2} = 800$ m. In other words, Fresnel-zone widths greater than 800 m, in this example, require larger offsets that are not present in the data. This explains the corners seen in the curves of Figure 6.3.

Appendix F

RANGE OF b

When dealing with ordinary p-waves, the DMO impulse response (i.e., the DMO ellipse) has a lateral extent of $2h$. The part of that lateral extent corresponding to non-evanescent seismic data (i.e., the range of b) is, Forel and Gardner (1988), bounded by

$$b = \pm \frac{2h^2}{vt}, \quad (\text{F.1})$$

relative to the midpoint.

Now, consider mode-conversion. Let the range of b be bounded by b_{max} and b_{min} relative to the midpoint. A surface of constant travelttime (pseudo-ellipse) is schematically depicted in Figure F.1. The extreme points, x_{max} and x_{min} , are trivially deduced as

$$x_{max} = \frac{vt - \eta h}{\sigma}, \quad (\text{F.2})$$

and

$$x_{min} = -\frac{vt + \eta h}{\sigma}, \quad (\text{F.3})$$

where σ is given by equation (2.10), and $\eta = 1 - 1/\gamma$ is another constant that depends only on the velocity ratio. For reflections from a vertical wall ($z=0$), the distance R , from point b to reflection point ($x, z = 0$), can be expressed as

$$R = x_{max} - b_{max}, \quad (\text{F.4})$$

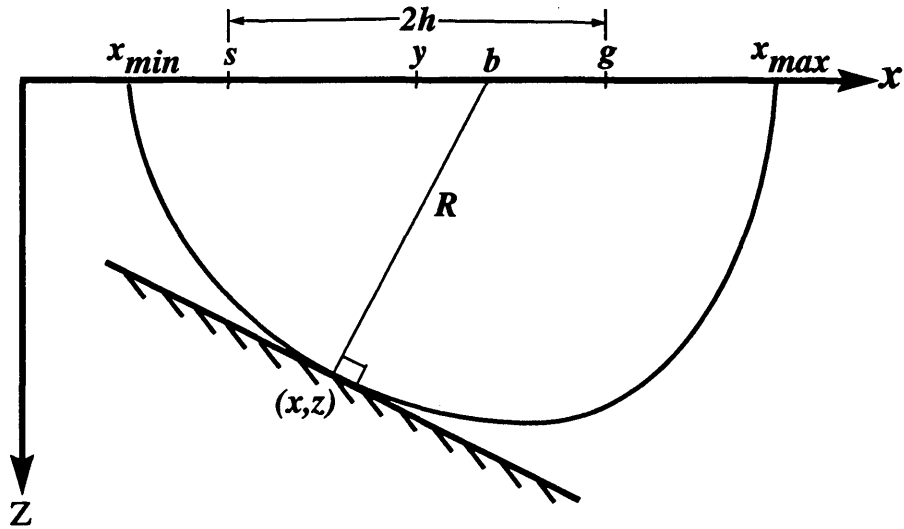


FIG. F.1. Surface of constant traveltime (pseudo-ellipse) for a mode-converted wave. The range of b corresponding to possibly recorded seismic data is along the line connecting source s and recorder g , but shorter than offset $2h$.

or

$$R = x_{min} - b_{min}, \quad (\text{F.5})$$

depending on whether the vertical wall is situated to the right or to the left of the midpoint y , respectively. Recalling equation (2.7), the expression for R^2 is given by

$$R^2 = (h^2 - b^2) \left[\frac{(vt)^2}{2h(\alpha h + \beta b)} - 1 \right], \quad (\text{F.6})$$

where α and β are defined in equations (2.3) and (2.10). Substituting for x_{max} and x_{min} their respective values from equations (F.2) and (F.3), squaring equations (F.4) or (F.5), and inserting the result in equation (F.6) yields quadratic equations for b_{max} and b_{min} , respectively. Their solutions are

$$b_{max} = \frac{h(2\alpha h - \eta vt)}{\sigma(vt - 2\eta h)}, \quad (\text{F.7})$$

and

$$b_{min} = \frac{h(2\alpha h + \eta vt)}{\sigma(-vt - 2\eta h)}. \quad (\text{F.8})$$

For $\gamma = 1$, the range of b as given by equations (F.7) and (F.8) reduces exactly to that in equation (F.1) for ordinary p-waves.

Appendix G

MAXIMUM t_1 ALONG A SMILE

From the relationship between D and D_y (Figure E.1), with positive dips being downward from source to receiver, and noting that $b \equiv a - y$, relation (E.3) between t_0 and t_{0y} can be expressed as

$$t_0 = t_{0y} + \frac{2b \sin \theta}{v_a}, \quad (\text{G.1})$$

where, again, we take a to be the origin, giving $y = -b$. As an aside here, if we substitute equation (G.1) into equation (2.11) and simplify, we obtain the following general expression for the square of the travelttime

$$t^2 = \frac{2h(\alpha h + \beta b)}{\sigma^2(h^2 - b^2)} \left[\left(t_{0y} + \frac{2b \sin \theta}{v_a} \right)^2 + \frac{4(h^2 - b^2)}{v_a^2} \right], \quad (\text{G.2})$$

which is valid for any velocity ratio γ .

Recall, each k -trace in a k - t_1 gather is obtained by stacking contributions from many midpoints. As shown in Section 6.3.1, a “smile” in the y - t_1 domain, after stack, typically generates an event on a k trace. The maximum t_1 , along a smile, occurs at a midpoint y corresponding to a b value that is truly the location of the equivalent zero-offset trace. The proof of this assertion, when $\gamma = 1$ (no mode conversion), follows.

Consider the relation for t_1^2 as given by equation (E.6). Differentiating that

equation with respect to y and setting dt_1/dy to zero yields the following quadratic relation in y

$$2y^2 \sin \theta + t_0 v y - 2h^2 \sin \theta = 0. \quad (\text{G.3})$$

Keeping in mind that $y = -b$ (the output location a is arbitrarily taken to be zero), equation (G.1) can be written as

$$t_0 = t_{0y} - \frac{2y \sin \theta}{v}. \quad (\text{G.4})$$

Substituting for t_0 its value from the above equation, and solving equation (G.3) for y yields

$$y = \frac{2h^2 \sin \theta}{vt_{0y}} = \frac{h^2 \sin \theta}{D_y} = -b, \quad (\text{G.5})$$

which is the same as that derived by Levin (1971). This proves the assertion made above.

Although not proven analytically, this same assertion also holds for mode-converted waves ($\gamma \neq 1$); I have shown this numerically.